INVESTIGATING PATTERNS AND KINEMATICS OF FAULTS AND ASSOCIATED FUMAROLIC ACTIVITY ABOVE A BLIND STRIKE-SLIP SYSTEM, BISHOP TUFF, CA

by

WILLIAM TALIAFERRO JENKINS

(Under the Direction of CHRISTIAN KLIMCZAK)

ABSTRACT

The Volcanic Tableland is situated in the Eastern California Shear Zone at the northern end of Owens Valley, CA. Volcanism from the adjacent Long Valley Caldera led to the eruption and emplacement of the ~ 760 ka Bishop Tuff atop the tectonically active valley floor. Through high-resolution mapping, three-dimensional modeling, and the documentation of new kinematic evidence of faulting, this research sheds new light on the deformation of the Volcanic Tableland and its relationship to regional tectonic evolution. Dip-slip, oblique-slip, and strike-slip kinematic indicators (grooves and slickenlines) preserved in the Bishop Tuff are all indicative of transtensional regional tectonics that have been active, at a minimum, since the tuff's emplacement ~ 760 ka. Newly compiled evidence suggests that these regional tectonics were responsible for the early formation of conjugate fractures and their subsequent enhancement to function as fumarolic pathways, thus governing fumarolic activity at the surface of the Volcanic Tableland.

INDEX WORDS: Structural Geology, Tectonics, Bishop Tuff, Owens Valley, Fumarole

INVESTIGATING PATTERNS AND KINEMATICS OF FAULTS AND ASSOCIATED FUMAROLIC ACTIVITY ABOVE A BLIND STRIKE-SLIP SYSTEM, BISHOP TUFF, CA

by

WILLIAM JENKINS

BS, Sewanee: The University of the South, 2015

A Thesis Submitted to the Graduate Faculty of The University of Georgia in Partial Fulfillment of the Requirements for the Degree

MASTER OF SCIENCE

ATHENS, GEORGIA

2019

INVESTIGATING PATTERNS AND KINEMATICS OF FAULTS AND ASSOCIATED FUMAROLIC ACTIVITY ABOVE A BLIND STRIKE-SLIP SYSTEM, BISHOP TUFF, CA

by

WILLIAM JENKINS

Major Professor: Christian Klimczak
Committee: Douglas Crowe
Mike Roden

Electronic Version Approved:

Suzanne Barbour
Dean of the Graduate School
The University of Georgia
May 2019

DEDICATION

I dedicate this work to Anna, my fiancée, who (at first and from a considerable distance of 2,000 miles) tolerated my nomadic lifestyle and general lack of cleanliness brought on by the solitary six weeks spent in the bed of my truck conducting this research, and then proceeded to accommodate such a lifestyle herself (in close proximity) while accompanying me for the long drive back east.

“There was a California earthquake, in the year of '83. It shook the living daylights out of the Owens County Seat. Not a building still left standing when the dust had cleared away. Just a rumble in the distance all the way to San Andrea.

…

California earthquake you just don't know what you've done. We may fall off in the ocean, but you'll never make us run. You're a partner to the devil, but we ain't afraid of him. We'll build ourselves another town so you can tear it down again.”

Grateful Dead live at The Spectrum - 10/20/1989
(three days after the M 6.9 Loma Prieta earthquake)
Originally composed by Rodney Crowell

ACKNOWLEDGEMENTS

I would first like to thank my thesis advisor Dr. Christian Klimczak for his guidance in the Structural Geology and Geomechanics lab at UGA, for suggesting I investigate the area around Bishop, and for his assistance in the field. From day one of my master's, Christian was instrumental in guiding me to research and develop a thesis project that pertained to my interests in structural geology and its multidisciplinary applications (e.g. geothermal energy, oil & gas, hydrothermal mineral deposits, and hydrogeology). Secondly, I would like to thank the other members on my thesis committee. Dr. Doug Crowe for his insight on hydrothermal mineral deposits and suggesting that I conduct sampling and preliminary analysis of the fumarolically altered tuff in the field. Dr. Mike Roden for joining my committee in the later stages of the project and providing his insight as an igneous petrologist.

I would also like to thank those affiliated with UGA's department of geology who assisted in this project. Patrick Trent for his assistance in creating composite photomicrographs from thin sections showing fumarolic alteration and devitrification in the Bishop Tuff. Dr. Jeff Speakman for allowing Patrick and I to utilize the XRF at UGA's CAIS lab and providing us with a means to analyze our data.

Lastly, I would like to thank the Chevron Corporation for providing the funding to support my research assistantship at UGA. I also acknowledge the use of the MOVE Software Suite granted by Petroleum Experts Limited (formerly Midland Valley Exploration Ltd.)

TABLE OF CONTENTS

Page

ACKNOWLEDGEMENTS v

LIST OF TABLES viii

LIST OF FIGURES ix

CHAPTER

1 INTRODUCTION 1

Regional Setting 1

The Volcanic Tableland 4

Description of Joints 6

Description of Faults 7

Kinematics of Tableland Fault System 9

Hydrogeology and Structure 10

Volcanic Tableland Sequence of Events 11

Hypothesis 13

2 METHODS 18

Preliminary Mapping 18

Fieldwork 19

XRF Analysis 20

Fault Response Modeling 20

Kinematic Analysis 23

Data Analysis of Modeled and Observed Fumarolic Pathways 25

3 RESULTS 27

Bishop Tuff Descriptions 27

Secondary Mineralization 32

Petrography 35

Fault Surface Morphology 36

Fault Kinematics 38

Joints and Fumarolic Pathways 42

Model Results 44

4 DISCUSSION 70

Faults, Kinematics, and Deformation of the Volcanic Tableland 70

Regional Stress of Northern Owens Valley 77

Formation of Conjugate Fractures and Fumarolic Pathways 80

5 CONCLUSIONS 89

REFERENCES 91

APPENDICES

A. DATA TABLES 96

LIST OF TABLES

Page

Table 1: Fault Kinematic Data.....96

Table 2: Mineralized Joint Data.....102

Table 3: Non-Mineralized Joint Data.....111

Table 4: Synthetic Joint Data.....121

LIST OF FIGURES

Page

Figure 1.1: Regional Map of Northern Owens Valley 15

Figure 1.2: Outcrop of Mesozoic Granite Beneath the Tableland 16

Figure 1.3: Panorama of the Stratigraphic Emplacement Units of the Tableland 17

Figure 2.1: Map Showing the Locations of Field Observations 26

Figure 3.1: Case-hardening of Fe-Oxides 46

Figure 3.2: Fault Scarp and Surface Morphology 47

Figure 3.3: Weathering and Case-hardening 48

Figure 3.4: Desert Varnish 49

Figure 3.5: Petrography of Welded and Devitrified Tuff 50

Figure 3.6: Fumarolic Features of the Volcanic Tableland 52

Figure 3.7: XRF and Petrography of Fumarolic Rind 53

Figure 3.8: Map Distribution of Structure and Fumarolic Mounds 55

Figure 3.9: Caliche Textures 56

Figure 3.10: Fault Surface Panorama 57

Figure 3.11: Fault Surface Pre-Rupture Soil Profile 58

Figure 3.12: Kinematic Indicators Observed in the Field 59

Figure 3.13: Kinematic Analysis of Structural Field Data 60

Figure 3.14: Stress Inversion of Field Data 61

Figure 3.15: Columnar Jointing in Owens River Gorge 62

Figure 3.16: Vertical Fumarolic Pathway 63

Figure 3.17: Secondary Mineralization on Columnar Joints 64

Figure 3.18: Conceptual Block Diagram of Cooling Joint 65

Figure 3.19: Comparison of Non-Mineralized and Mineralized Joint Orientations 66

Figure 3.20: Comparison of Synthetic and Mineralized Joint Orientations 67

Figure 3.21: Three-Dimensional Modeling of the 1986 CVES and Synthetic Joints 68

Figure 4.1: Extent of the Transtensional Zone beneath the Volcanic Tableland 87

CHAPTER 1

INTRODUCTION

Regional Setting

The Owens Valley in eastern California, where the Bishop Tuff is found, trends roughly northwest-southeast, lying between the Sierra Nevada and the White-Inyo mountains, along the western edge of the Basin and Range province (Figure 1.1). The valley is a large graben that formed as the result of extensive down faulting following the Pliocene-Pleistocene break-up of the Sierra Nevada-White-Inyo mountain block, formation of the Sierra Escarpment, and the subsequent uplift of the White-Inyo mountains (Bachman, 1978). Furthermore, the area has actively undergone a regional tilt of the Sierra Nevada to the west (0.28^{o}/Ma), northern Owens Valley to the east (3.5-6.1^{o}/Ma), and White Mountains to the east (0.47^{o}/Ma) (Unruh, 1991; Pinter and Keller, 1995; Marchand, 1971). The Owens Valley is characterized by approximately east-west extension and dextral strike-slip motion along oblique valley-bounding faults (Lovely, 2011). Recent research by Phillips and Majkowski (2011) suggests that faults bounding Owens Valley are low-angle, by highlighting a supposed discrepancy between extension rates (~1.5 mm/yr over 3.5 Ma), assumed steep fault dips (60^{o}), and valley displacement relative to the prominence of adjoining mountain ranges (~ 4km from peaks to valley basement). Using these parameters, Phillips and Majkowski (2011) predict a total vertical displacement of the valley between 8-10 km; however, it appears that they did not account for the graben geometry (two graben-bounding faults) of Owens Valley. Accounting for this extension along two graben-bounding faults yields a displacement value of ~ 4.55 km, which is similar to the reported

vertical displacement of Owens Valley and suggests that the valley bounding faults are indeed steep.

The present topography of the valley is believed to have formed since the middle to late Pliocene (3.5 – 2.3 Ma), during which relative displacement between Owens Valley and the surrounding mountain blocks has been between 2.3 and 5.0 km (Pakiser et al., 1964; Bachman, 1978; Phillips and Majkowski, 2011). The west-dipping White-Mountain Fault Zone (WMFZ) and Owens Valley Fault (OVF) parallel the trend of the valley (Figure 1.1) and accommodate substantial extension and dextral slip from the Eastern California Shear Zone (ECSZ), which together with the Walker Lane Belt accounts for 20-25% of the relative motion between the Pacific and North American plates (Dixon et al., 2000). The remaining ~ 75% of dextral motion is believed to be accommodated along the San Andreas Fault to the southwest (Nagorsen-Rinke et al., 2013).

The northern Owens Valley is of particular interest given that it lies at the junction between the western margin of the Basin and Range province, the Long Valley Caldera, and the Sierra Nevada microplate. Unruh et al. (2003) proposed that normal faults in this region are the result of the northwestern translation of the Sierra Nevada microplate, and that Owens Valley represents a releasing geometry from the transtension manifested along the Sierra Nevada's eastern microplate boundary. It is believed that regional stresses resulting from this tectonic situation were also a driving force in the development of the Long Valley Caldera, whereby extension and subsequent magma intrusions from the adjoining Sierra Nevada lead to the subsidence and volcanism of the caldera proper (Pakiser et al., 1964).

Bedrock along the flanks of the Owens Valley can be generally distinguished by mountain range. In the Sierra Nevada, bedrock primarily consists of Mesozoic granitoids that

comprise the Sierra Nevada Batholith, along with its included Paleozoic and Mesozoic metasedimentary roof pendants (Pakiser et al., 1964). Bedrock in the Benton Range (northeast of the Long Valley Caldera) and the Tungsten Hills to the south is similar in age and composition to the Mesozoic granitoids of the Sierra Nevada (Pakiser et al., 1964). In the White-Inyo Mountains, Paleozoic sedimentary units are the dominant bedrock, with contact metamorphosed metasediments present in the northern White Mountains (Pakiser et al., 1964).

Using geophysical and structural data, Hollett et al. (1991) subdivided the graben beneath the northern Owens Valley into two distinct structural basins: the Bishop Basin, and the Owens Lake Basin. The Bishop Basin is bounded to the east by the White Mountain Fault Zone, to the west by the Round Valley Fault, and to the southwest by the Coyote Warp. The east-dipping Round Valley Fault is located on the flank of the Sierra Nevada and Long Valley Caldera, and it exhibits both dip and dextral slip (Hildreth et al., 2017). The Coyote Warp is a broad downwarped surface of the Sierra Nevada extending north-northeast beneath the present Owens Valley surface, which is related to the eastern deflection of dextral range-front faulting from the Sierra Nevada to the WMFZ and may represent a large normal fault propagation fold (Pakiser et al., 1964; Dawers et al., 2002). To the south, the Bishop Basin is truncated by a northeast-dipping normal fault beneath the Poverty Hills. Immediately south of the Bishop Basin and Poverty Hills lies the Owens Lake Basin. As the Owens Valley graben developed from Pliocene to present, the valley was filled with several kilometers of volcanic rocks (e.g. rhyolite, basalt, tuff, pumice, breccia), reworked volcaniclastics, glacial outwash, alluvium, and lacustrine sediments (Gilbert, 1938; Pakiser et al., 1964; Bateman, 1965; Hollett et al., 1991; Lovely, 2011). Valley fill was deposited atop pre-Quaternary granitic, metamorphic, and sedimentary

basement units. At present, sedimentation rates have exceeded the subsidence of the Poverty Hills fault, and the former Bishop and Owens Lake basins are linked.

Gravity surveys identifying the contrast between Cenozoic valley fill material and underlying pre-Tertiary basement suggest that the basement along the western margin of the northern Owens Valley is warped downwards across the valley to the east and forms an east-trending synclinal structure between the Coyote Warp and the Benton Range along its limbs (Bateman, 1965; Pakiser et al., 1964). The warped surface continues until its intersection with the White Mountain Fault Zone, and valley fill thins accordingly from east to west (Bateman, 1965).

The Volcanic Tableland

The field site described in this study is located on the Volcanic Tableland, a topographic plateau at the northern end of the Owens Valley, just north of Bishop, California. The Volcanic Tableland is immediately bounded to the east by the White Mountain Fault Zone and lies between the Benton Range to the north and the Coyote Warp to the south.

The tableland is capped by the 758.9 $\pm$ 1.8 ka Bishop Tuff (Sarna-Wojcicki et al., 2000), a layered ignimbrite atop a basal plinian fall deposit that formed from a series of nuées ardentes following the collapse of the Long Valley Caldera (Bateman, 1965; Wilson and Hildreth, 1997). At its base, the Bishop Tuff and associated fall deposits are observed to overlie valley-fill sediments on the southern end of the tableland and granitic bedrock in the central Owens River gorge (Figure 1.2), suggesting a varied lithology and topography at depth (Gilbert, 1938; Bateman, 1965; Hollett et al., 1991; McGinnis et al., 2009). Regional gravity surveys and basin-depth maps identified a curved basin beneath the southern and eastern extent of the tableland that

coincides with synclinal flexure between the Benton Range and Coyote warp as well as with faulting along the White Mountain Fault Zone (Pakiser et al., 1964; Saltus and Jachens, 1995).

The tuff itself has been subdivided into two packages, Ig1 and Ig2, representing two subsequent stages of the Long Valley Caldera eruptive sequence (Wilson and Hildreth, 1997; Wilson and Hildreth 2003). The two packages exhibit a proximal (Ig1) and distal (Ig2) relationship from the caldera center. The second Ignimbrite package Ig2 varies from ~ 70 - 150 meters in thickness on its southern margin, forms the Volcanic Tableland, and is the focus of this study. It can be further divided into a moderately to densely welded cap (Ig2Eb), and an underlying non- to poorly-welded tuff (Ig2Ea) (Wilson and Hildreth, 1997; Figure 1.3). Three zones of vapor-phase crystallization (Ig2Ec) overlie densely welded and devitrified units in the tuff, capping parts of the Volcanic Tableland (Sheridan, 1970; Wilson and Hildreth, 1997). These zones were formed from volatiles released during devitrification, as SiO_2 and anhydrous feldspars formed from the hot ash and pumice present in lower units of the ignimbrite (Vaniman, 2006).

Domical mounds and elongated ridges on the surface of the tableland represent fossil fumarolic features that once behaved as loci of intense vapor-phase and hydrothermal activity (Sheridan, 1970). The source for fumarolic vapors remains speculative. Sheridan (1970) suggested the fumaroles formed solely from degassing occurring within the tuff sheet, while Holt and Taylor (1998) suggested a combination of processes involving the influx of meteoric waters, hydrothermal circulation, and degassing.

Since emplacement, the tuff has been structurally modified by the formation of deep-rooted vertical conjugate joints, shallow-rooted curvilinear cooling joints, and columnar joints in areas of enhanced cooling and vapor-phase alteration (Sheridan, 1970). Furthermore, regional

tectonic extension and associated north and northwest striking faults have segmented the Bishop Tuff into hundreds of horsts, graben, and relay ramps.

Description of Joints

Joints in the Bishop Tuff are believed to have both thermal and tectonic origins. A series of northeast and northwest striking conjugate joints intersect at acute, dihedral angles. Bateman (1965) suggested that these were conjugate shear planes formed from a regional horizontal principal stress, similar to the conjugate joints observed in the Mesozoic granitoids of the Sierra Nevada and Tungsten Hills. Likewise, Sheridan (1970) observed offsets and minor slickensides along the surfaces of conjugate joints, leading him to believe that they were shear fractures that formed after welding increased the competency of the tuff sheet. Fumarolic activity is reported to have utilized conjugate joints, and evidence indicates that the joints extend vertically into the tuff sequence, localizing vapor-phase alteration along the joint walls (Sheridan, 1970). As a result of the increased heat flow from rising fumarolic vapors, columnar joints radiate outwards from vertical conjugate joints in upper units of the tuff (Sheridan, 1970; Holt and Taylor, 1998). On a smaller scale, curvilinear cooling joints are believed to have formed after vapor-phase alteration was complete because they show no signs of alteration (Sheridan, 1970). Cooling joints have variable orientations (polygonal with curving dips and strikes), and they often approach orthogonal intersections with larger conjugate joints which indicates that they likely formed from the release of thermal stress as the tuff continued to cool (Sheridan, 1970).

Description of Faults

The faulting of the Volcanic Tableland has been the subject of many previous research efforts because it preserves a record of the structural evolution of the northern Owens Valley since the emplacement of the Bishop Tuff (e.g. Bateman, 1965; Dawers et al. 1993; Dawers and Anders, 1995; Pinter, 1995; Lovely, 2011; Phillips and Majkowski, 2011; Ferrill et al., 2016). In general, faults strike between N10°W and N20°W, dips of ~ 60° (east and west) have been estimated from profiles due to the absence of accessible fault scarps, and many occur in left-stepping en echelon arrangements with relay ramps evident where fault tips overlap (Pinter, 1995). The lack of high-resolution geophysical data coupled with heterogeneous regional tectonics contribute to the complexity of the area's structural interpretation.

The nucleation of faults on the Volcanic Tableland is debated in the literature. Systematic displacement-length ratios and nearly constant fault-tip gradients led Dawers et al. (1993) to suggest that the tableland faults nucleated at the free surface of the welded tuff as a result of flexural extension from normal faulting along the White Mountain Fault Zone. However, faulting is also suggested to have propagated vertically upwards from preexisting structures buried beneath the Bishop Tuff at the time of emplacement (e.g. Bateman, 1965; Ferrill et al., 2016).

Through analyzing the scaling relationship between fault length and displacement, Dawers et al. (1993) suggested that the variation they observed between peaked and plateaued displacement profiles was a function of fault length. In particular, peaked displacement profiles are representative of faults that are contained entirely within the ignimbrite sheet, and plateaued displacement profiles are representative of faults that break through the ignimbrite sheet. Therefore, Dawers et al. (1993) interpreted plateaued fault displacement profiles to suggest a sharp contrast in the mechanical properties of underlying units that inhibited the development of

further fault displacement. Dawers et al. (1993) calculated that a semi-elliptical fault (2:1 aspect ratio) propagating from the surface would begin to break through the base of the thickest part of the tuff sheet (~ 150 m) with lengths approaching ~ 600 m. Knowing that many tableland faults exceed this length (Pinter, 1995) and that the tuff is rarely more than 150 m in thickness (Hildreth and Fierstein, 2017), the methodology used by Dawers et al., (1993) implies that many of the faults in this fault population would penetrate the entire ash-flow sheet even if nucleation had occurred at the free surface. Therefore, regardless if faults utilized preexisting structures at depth or nucleated from the surface of the tableland, their vertical continuity through the Bishop Tuff can and should be acknowledged.

Fault scarp morphology in the Bishop Tuff is obscured by colluvial processes as scarps are often mantled with loose sediment and joint-bounded boulders, making it difficult to locate fault surfaces and kinematic indicators (Pinter, 1995; Evans and Bradbury, 2004; Ferrill et al., 2016). One potential explanation for the scarcity of preserved slickenlines is that fault-tip monoclinal folding precedes scarp rupture on a vertically propagating fault, thereby dilating preexisting joints in the moderately welded cap of the Bishop Tuff and reducing the frictional contacts capable of forming a fault surface (Ferrill et al., 2012; Ferrill et al., 2016). Conversely, slickenlines would be formed along existing surfaces with minimal dilation, or new shear surfaces altogether. For instance, Evans and Bradbury (2004) identified slickenlined surfaces along several small faults in the non-welded units expressed along the southern terminus of the Volcanic Tableland, attributing their formation to the development of cataclastic shear failure in an unfractured medium.

Kinematics of Tableland Fault System

Throughout much of the existing literature on the subject, the kinematics of the faults on the Volcanic Tableland have been believed to be primarily dip-slip resulting from east-west valley extension and the subsequent down warping of the Bishop tuff along the White Mountain Fault Zone (e.g. Dawers et al., 1993; Pinter, 1995; Phillips and Majkowski, 2011; Ferrill et al., 2016). North trending fault strikes roughly perpendicular with regional extension and the lack of accessible, well-preserved fault surfaces and kinematic indicators have contributed to this belief. Other research has suggested that the northwestern en echelon arrangement of normal faults on the Volcanic Tableland accommodates regional transtensional dextral shear (Bateman, 1965; Pacheco and Nabelek, 1988; Smith and Priestly, 2000; Nagorsen-Rinke et al., 2013; Delano, 2015). Bateman (1965) suggests that the east-west synclinal warp and lack of faulting in the basement between the Benton Range and the Coyote Warp implies regional north-south shortening, which combined with the en echelon arrangement of east and west dipping faults allows for a clockwise rotation couple.

In late July of 1986, a period of increased seismicity culminating in three moderately sized earthquakes (M 5.7 on July 20th; M 6.3 on July 21st; and M 5.5 on July 31st) and their associated aftershocks occurred in the Chalfant Valley area north of Bishop, in what became known as the 1986 Chalfant Valley earthquake sequence (Smith and Priestly, 2000). The earthquake sequence shed light on the presence of a conjugate blind strike-slip system buried beneath the tableland, which provided further evidence of transtensional dextral shear being manifested across the Volcanic Tableland. Following the earthquake, Lienkaemper et al. (1987) recorded en echelon patterns preserved in loose sediments atop the tableland that were similar to

the area's distribution of normal faults, but their findings lacked concrete evidence directly linking kinematics in the tuff to the underlying strike-slip fault system.

To explain the differences between peaked and plateaued fault displacement profiles recorded on the tableland, Dawers et al. (1993) postulated that the plateaued displacement profiles observed along larger tableland faults indicate that poorly consolidated valley fill material underlying the tuff behaves as a buffer allowing for normal faulting at the surface that is kinematically distinct from strike-slip faulting in the basement. Such distributed deformation was also suggested by Lienkaemper et al. (1987) to occur in the alluvium beneath the Bishop Tuff, differentiating between simple shear at seismogenic depth and fault-guided slip on the existing structures of the Volcanic Tableland, ultimately linking tableland deformation to many deep seismic events similar to the Chalfant Valley earthquake sequence. Furthermore, Pinter (1995) discovered an ~ 2 m undegraded fault surface that preserved a pre-rupture soil profile, indicating that tableland faults are coseismic with earthquake ruptures capable of producing surface displacement of the same magnitude. This discovery shed light on a more substantial link between seismic events at depth and deformation atop the Volcanic Tableland; however, the lack of additional kinematic evidence and fault scarps precluded further analysis on fault slip.

Hydrogeology and Structure

The combination of faults and conjugate joints forms a complex, pervasive structural network across the ~ 350 km^2 area included in this study. As a result, groundwater migration and storage in the region is largely controlled by these structures as they behave both as lateral conduits for subsurface flow into aquifers, and vertical conduits for capturing surface flow and emitting active thermal springs such as those that emerge from fault tips in the Fish Slough area

(Jaykoh and Fatooh, 2010). Hydrologic data indicates that the 1986 Chalfant Valley earthquake sequence disrupted aquifers and thermal springs in the surrounding region, illuminating their potential relationship with deep-seated structures. Seven groundwater wells in Fish Slough and Chalfant Valley recorded a rising water table following the earthquake sequence, and enriched O^{18} isotopes of thermal springs in Fish Slough are indicative of a hydrothermal system at depth (Jaykoh and Fatooh, 2010). Additionally, public access to hot springs in the Long Valley Caldera over 36 km northwest of the M 6.3 epicenter (Figure 1.1) was restricted as a consequence of a higher influx of thermal waters migrating along fracture planes due to the increased seismicity (Brewer, 1989).

Volcanic Tableland Sequence of Events

The collapse of the Long Valley caldera and subsequent emplacement of the Bishop Tuff occurred 758.9 $\pm$ 1.8 ka (Sarna-Wojcicki et al., 2000). Eruptive chronometry suggests that the Bishop Tuff and fall deposits were emplaced over a period of about six days due to the lack of erosion, fallout, or significant reworking of the tuff present on the cooling surfaces between emplacement units (Wilson and Hildreth, 1997). Pre-existing depressions on the surface of Owens Valley accommodated thick portions of the tuff, which allowed for welding to occur in the tuff sheet interior (Wilson and Hildreth, 1997). Along the upper and lower contacts of the tuff and in areas where the tuff sheet was relatively thin, cooling occurred more quickly and welding did not occur (Wilson and Hildreth, 1997).

Post-emplacement welding and compaction of the tuff aided in developing the competency necessary to support the formation of vertical conjugate joints with preferred northeast and northwest orientations (Bateman, 1965; Sheridan, 1970). After welding,

devitrification resulted in the crystallization of glass and the expulsion of volatiles (Vaniman, 2006). It has also been suggested that meteoric water was introduced into the cooling tuff at this time (Holt and Taylor, 1998). Resulting fumarolic activity ensued along vertical conjugate fractures, hydrothermally altering the immediately adjacent rock volume (Sheridan, 1970). Such fumarolic features atop the cap of the tableland are fossil remnants of an intricate system of pathways that once transmitted escaping vapors. The hydrothermal alteration indurated the loose, non-welded tuff at the top of the ignimbrite sequence and represents a zone of vapor-phase alteration (Sheridan, 1970; Wilson and Hildreth 1997). Non-welded ash that was not affected by fumarolic activity, was later stripped to the top of the indurated vapor-phase zone by erosive processes (Sheridan, 1970). Following fumarolic activity, short and relatively shallow-rooted cooling joints developed at orthogonal angles to existing fractures, forming a complex web of curvilinear features with no signs of alteration or secondary mineral coatings (Sheridan, 1970). Mapped radiating and polygonal patterns of cooling joints adjoining fumarolic mounds in the Bishop Tuff are likely a result of enhanced cooling from rising vapors during fumarolic activity (de Silva, 2017).

Sometime after welding and compaction, the Bishop Tuff was tectonically modified forming hundreds of north-striking normal faults, which express more than 290 meters of cross-valley extension since its deposition (Pinter, 1995). Evidence suggests that faulting is still active on the tableland and is likely a coseismic process with earthquake activity occurring in the northern Owens Valley (Pinter, 1995).

Hypothesis

The 1986 magnitude 6.3 Chalfant Valley earthquake sequence shed light on conjugate dextral and sinistral strike-slip faulting beneath the Bishop Tuff (Cockerham and Corbett, 1987; Smith and Priestly, 2000). The strike-slip fault on which the main shock occurred has not yet been observed to breach the surface of the Volcanic Tableland, but small left-stepping offsets in unconsolidated sediments were observed during the weeks following seismic activity, marking the only study correlating strike-slip motions at depth to surficial expressions on the tableland (Lienkaemper et al., 1987). Many normal fault orientations curve to a dominant northwestern trend across the field site, which is coincident with the mapped distribution of earthquake epicenters, regional dextral shear, and the northwestern translation of the Sierra Nevada microplate described in past research (Unruh et al., 2003; Nagorsen-Rinke et al., 2013). The opposing sinistral and dextral motions of the conjugate strike-slip system have also been suggested to contribute to the extensional mechanisms manifested in the Bishop Tuff (Dawers et al., 1993; Smith and Priestly, 2000). Previous research has only identified the presence of strike-slip faulting at depth using focal mechanisms produced from relocated seismic data and offered conjectures of its influence on the Bishop Tuff (Cockerham and Corbett, 1987; Pacheco and Nabelek, 1988; Smith and Priestly, 2000; Nagorsen-Rinke et al., 2013; Delano, 2015). To date, there has been no fieldwork specifically addressing the effects of this underlying strike-slip system on the Bishop Tuff. Furthermore, the relationship between fumarolic features (mounds and ridges) on the Volcanic Tableland and structures (faults and conjugate joints) has been well documented (Sheridan, 1970; Holt and Taylor, 1998); however, the mechanisms for their structural development and enhancement as fumarolic pathways have not yet been explored. Therefore, I hypothesize that structures in the Bishop Tuff record the kinematics of a blind

strike-slip system, and that associated tectonic activity played a key role in the early development of fumarolic pathways.

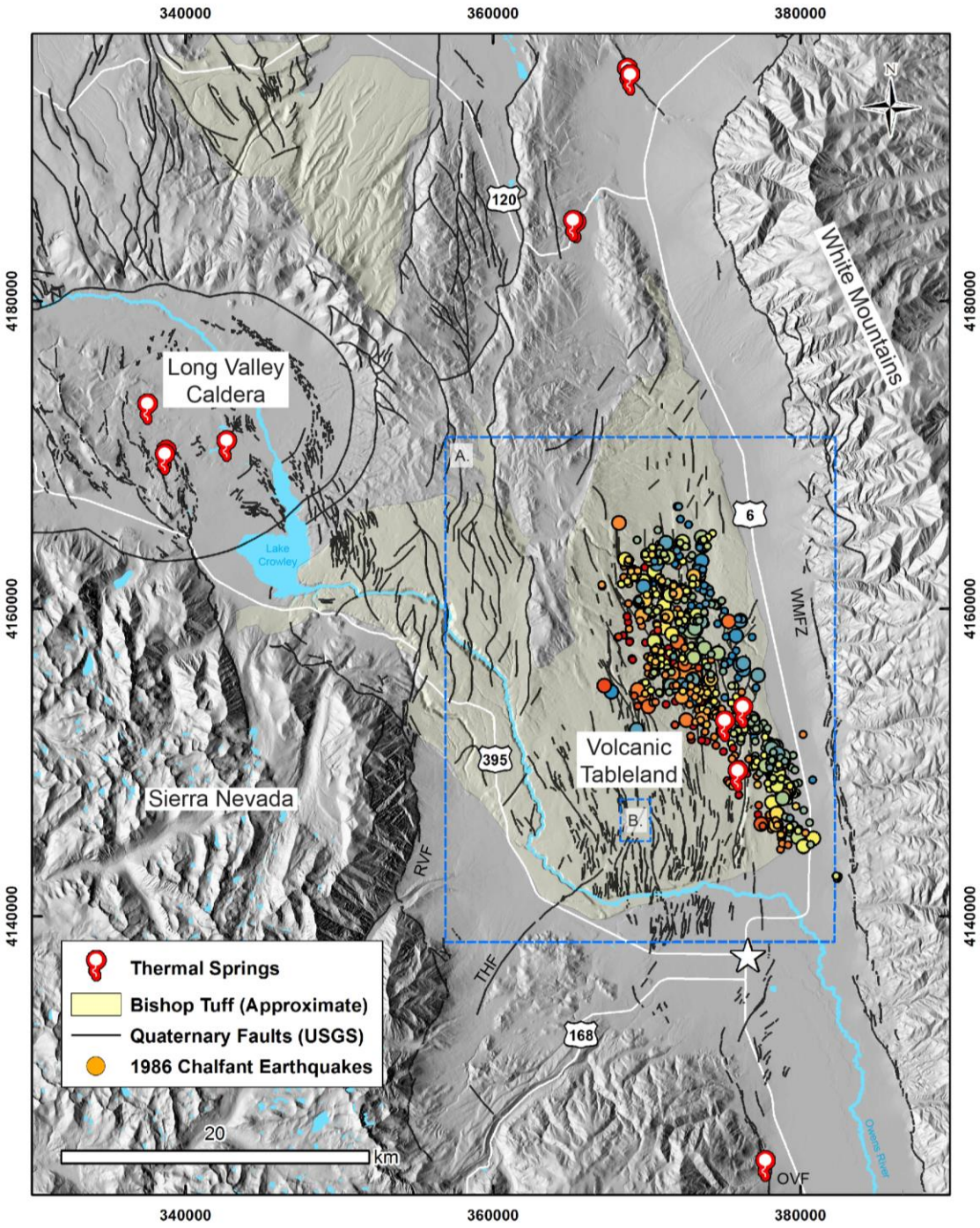

Figure 1.1. Map of northern Owens Valley (UTM Zone 11 N) showing Quaternary faults (USGS database) and active thermal springs. Regional faults included in this study have been labeled with the following abbreviations: White Mountain Fault Zone (WMFZ), Owens Valley Fault (OVF), Tungsten Hills Fault (THF), and Round Valley Fault (RVF). Hypocenters from the 1986 Chalfant Earthquake Sequence are colored according to depth (blue/green = shallow (~ 2 km), red = deep (~ 11 km)) and sized by magnitude (larger symbols correlate with greater magnitude events). Bishop, CA is indicated by the white star. (A) Map extent for figures 2.1, 4.1, and 3.21. (B) Map extent for figure 3.8.

Figure 1.2. An outcrop of Mesozoic granitoid beneath the Bishop Tuff in Owens River Gorge representing a basement high and indicating the varied topography beneath the Volcanic Tableland.

Figure 1.3. Stratigraphic position of the tableland emplacement units of the Bishop Tuff in Owens River Gorge. Nomenclature follows the units described by Wilson and Hildreth (1997). The upper ignimbrite package (Ig2) and its subunits (a,b,c) are the focus of this study, Note the contrasts in colors and degrees of welding between the units. Higher degrees of welding support more vertical slopes (cliff forming), while less welded tuff forms slopes. The outcrop of Ig2Ec is thin and forms a small cap on the NW margin of this panorama.

CHAPTER 2

METHODS

Preliminary Mapping

Prior to fieldwork, the site was thoroughly mapped with ArcGIS using 1-meter aerial imagery from the National Agriculture Imagery Program (NAIP), and publicly available 1- and 10-meter resolution digital elevation models from the National Center for Airborne Laser Mapping (http://opentopo.sdsc.edu/datasetMetadata?otCollectionID=OT.042016.26911.1) and the USGS respectively. Faults and fumarolic mounds identifiable on DEMs and aerial imagery were mapped at different scales given the variability in coverage and resolution of available data sets. Where data resolution was the highest (e.g. 1-meter DEM and imagery), faults were mapped at a 1:5,000 scale, and fumarolic mounds were mapped at a 1:2,500 scale. Fossil fumaroles were identified as peaked topographic mounds on DEMs and round to elongate features with vapor-phase alteration halos in aerial imagery. They were mapped as point features, whereby a point was placed in the approximate center of each identified mound or ridge. Faults were identified as having vertical offsets on DEMs and visible scarps in aerial imagery. They were mapped as polylines with appropriate symbols indicating their respective dip directions. In total, 2,164 fumarolic mounds and 749 faults were mapped across the Volcanic Tableland north and east of the Owens River prior to beginning fieldwork (Figure 2.1). The preliminary map was used to identify sites for collecting field data and navigating around the area.

Fieldwork

In the field, the structural orientations of joint planes (n = 837), and 267 fault surfaces and their corresponding kinematic indicators of slip (e.g. slickenlines and grooves) were recorded using the FieldMove Clino application (Midland Valley Exploration Ltd.) in lieu of a Brunton Compass. It should be noted that the application follows the British right hand rule, whereby fingers are placed down-dip and the thumb indicates the strike-direction, so the results produce strikes that are opposite (180^{o}) to the American right hand rule. Coordinates of each observation were recorded in the application, as were any applicable field notes. Tables of fault kinematic data and joints are included in the appendices (Tables 1-3). As much of the field site is remote, hiking and driving along four-wheel drive roads were the sole modes of access to conduct field observations.

To test whether faults in the Bishop Tuff record the underlying motion of a blind strike-slip fault system, kinematic indicators were located, and their orientations were recorded for further analysis. Deformation bands that would serve as precursors to faults and provide additional kinematic evidence were sought in porous units of the tuff; however, no such bands were discovered in the field and thus they are not discussed in this thesis. To assess the relationship between structure (faults and joints) and fumarole development, observations were recorded where their overlap was observed in the field (e.g. faults cutting fumaroles, or joints with noticeable fumarolic alteration). Likewise, the morphology of fumarolic alteration was described in field notes. Scaled photographs were taken of all relevant observations including fault surfaces, slickenlines, joints, fumarolic features, tuff morphology, and outcrops. For petrographic analysis of fumarolic alteration, hand samples were collected from 37 fumarolic

features across the field site and 9 thin sections were prepared. The localities of all field observations are presented in Figure 2.1.

XRF Analysis

Of the 37 samples collected in the field, 20 were selected for XRF analysis in order to further describe the mineralization associated with fumarolic activity in the Bishop Tuff. A stationary Bruker © handheld XRF (Rhodium anode) linked to Bruker Artax Spectra © software (version: 8.0.0.471) on a desktop computer was used to complete the analysis. The handheld XRF unit was calibrated in order to identify potential potassium bearing minerals that may have been associated with fumarolic activity (e.g. Adularia). Samples were placed flush against the XRF unit, and were analyzed for a duration of 16 seconds with the following parameters: high voltage - 20kV, current - 25 μA, energy range – 10.0 KeV, stripping cycles – 10. The following elements were included in the readout for each sample: Al, Ar, Br, Ca, Cr, Cu, Fe, Ga, K, Mg, Mn, Na, Ni, P, Rh, S, Si, Ti, Zn. Data was exported from the Bruker Artax Spectra © software (version: 8.0.0.471) into a .csv file for analysis in the open-acess statistical computing software *R*.

Fault Response Modeling

In the lab, Midland Valley's Move software was used to plot earthquake hypocenters of the 1986 Chalfant Valley Earthquake Sequence from the Northern California Earthquake Data Center and interpolate large-scale regional fault planes beneath the Volcanic Tableland to form a three-dimensional fault model. Smith and Priestly (2000) identified three fault planes active during the earthquake sequence from relocated aftershocks, depicting a conjugate strike-slip

system and the White Mountain Fault Zone. The three fault planes produced in this study share a similar geometry and were assigned the following naming conventions: Chalfant Valley Fault (CVF), Tungsten Hills Fault (THF), and the White Mountain Fault Zone (WMFZ). Fault planes were easily identified by the geometry of their hypocenters, with Y-junctions apparent between the CVF-THF and the CVF-WMFZ. This allowed for the isolation of hypocenter point clouds for each individual fault plane, from which three-dimensional fault surfaces could be interpolated using Inverse Distance Weighting. As the modeled conjugate strike-slip system has not been observed to break the surface of the tableland, it was constrained vertically by the maximum and minimum depths for hypocenters on each plane, denoting each respective seismogenic zone. The White Mountain Fault Zone, however, is manifested along the intersection of the Owens Valley floor and base of the White Mountains. Therefore, the upper limit of the fault plane was modeled according to its surface expression, and the lower limit was constrained by its respective maximum hypocenter depths. As it is believed that only a portion of the WMFZ was involved during the 1986 earthquake sequence, the interpolated surface was extended along its strike according to its mapped trace along the base of the White Mountains (Smith and Priestly, 2000). After each fault surface was interpolated from its respective hypocenter point cloud, a smoothing tool was used to eliminate computer-generated asperities and create more realistic fault surfaces.

In order to simulate the stresses that were active during the 1986 Chalfant Valley Earthquake Sequence, Move's Fault Response Modeling Module was used to recreate displacement magnitudes and directions along the three interpolated fault surfaces and observe the combined effects of fault movement (stress, strain, and displacement) experienced by a surface in the same elastic medium. For the purpose of this study, the observational surface was created in Move to represent the current expression of the Bishop Tuff atop the Volcanic

Tableland at an average elevation of 1,500 meters above sea level. Understanding that fault slip is not uniform across a fault plane, slip maxima were defined in the centroid of each modeled fault and slip was tapered toward the fault tips. Likewise, given that faulting does not occur in an infinite elastic medium, a free surface was defined directly above the modeled elevation of the Bishop Tuff in order to accurately model elastic dislocations in a half space (Comninou and Dundurs, 1975).

In accordance with previous observations, the slip sense of each modeled fault was assigned accordingly: CVF-dextral, THF-sinistral, WMFZ-dextral (Lienkaemper et al., 1987; Cockerham and Corbett, 1987; Smith and Priestly, 2000). Stress drop and displacement calculations by Smith and Priestly (2000) yielded average slip displacements of 1.50 meters on the primary dextral fault (CVF), 0.71 meters along the conjugate sinistral fault (THF), and 0.25 meters along the WMFZ. For the scope of this study, these slip displacement parameters were input into Move's fault response modeling module in order to generate a simulated stress field analogous with the stress conditions that were active during the 1986 earthquake sequence. As there are no observations to support modeling any opening or closing that occurred along the full extent of each fault surface, such parameters were omitted from the simulation.

Upon generating the simulated stress field a set of synthetic joints (n = 397) was produced to represent optimal fumarolic pathways, and joints within the set were assigned an equal spacing of 1.5 km across the 350 km^2 extent of the field site. This sample size was selected in order to match the number of recorded mineralized joints in the field. Although a smaller joint spacing would yield a greater number of synthetic joints, the overall orientations of the joints would remain the same given they are a function of the reproduced stress field. The synthetic joints were assigned a vertical dip in order to reflect the vertical nature of fumarolic pathways

observed in the field and described in previous research (Sheridan, 1970; Holt and Taylor, 1998). To find the optimal azimuth of a synthetic joint, the software rotated the azimuth of each joint plane in 1-degree intervals around a full 360° and selected the azimuth with the maximum Coulomb stress change according to the chosen displacement, in this case dilation. The model results consist of a synthetic fracture network that was most likely to experience dilation given the stress conditions exhibited during the 1986 Chalfant Valley earthquake sequence and could be used for comparison with the observed orientations of fumarolic pathways.

Kinematic Analysis

To analyze the kinematic data obtained from fault surfaces in the field, 267 slickenline measurements and corresponding fault planes were imported into Allmendinger's FaultKin software to plot a stereonet with arrows indicating the respective hanging wall slip directions (Allmendinger, 2017). Kinematic axes (P and T) of each recorded slickenline and fault pair were individually calculated. These axes represent the principal axes of the incremental strain tensor of a fault (Marrett and Allmendinger, 1990), and thus define quadrants of dilation (P) and compression (T) for each recorded fault plane. On an infinitesimal scale (approaching the intersection of nodal planes), they represent shortening axes (P) and extensional axes (T). The orientation of kinematic axes was calculated as being 45º from the fault pole along a movement plane that intersects the plotted slickenline, so each kinematic axis is 90º from the other. The pole for the movement plane that intersects both the plotted slickenline and kinematic axes is defined by the intersection of nodal planes. Therefore, the labeling of P and T axes respectively varies according to the sense of slip recorded on the fault plane.

Plotted kinematic axes were then graphically analyzed using linked Bingham distribution statistics to identify the directional maxima of P and T axes for a fault population (Marrett and Allmendinger, 1990). The resulting maxima were produced operating under the assumption that fault kinematics on the site are scale-invariant because the individual magnitudes of deformation (displacement and fault surface area) for each fault in the population could not be recorded. Regardless, scale-invariant fault kinematics for other large data sets have been well documented in existing literature (e.g. Marrett and Allmendinger, 1990). Directional maxima of P and T axes were used to produce composite fault plane solutions for the three fault populations recorded and observed in the field (normal, oblique, and strike-slip). The T quadrants of the resulting fault plane solutions were shaded to indicate regions of compression therefore their appearance is similar to seismic focal mechanisms whereby T quadrants, identified by peaked first motions (compressive P-waves), are also shaded. Faults were classified using a simplified version of the Zoback criteria whereby faults were grouped by the plunge of their respective kinematic axes to identify their stress regime: normal (P plunge $\geq 52^{o}$, T plunge $< 40^{o}$), oblique ($40^{o} \leq$ P plunge $< 52^{o}$, T plunge $< 40^{o}$), strike-slip (P plunge $< 40^{o}$, T plunge $< 40^{o}$) (Zoback, 1992; Boore et al., 2013). It is important here to recognize that any slickenline plunging between true horizontal (0^{o}) and vertical (90^{o}) is the result of oblique slip, so the aggregate fault plane solutions for normal and strike-slip faults indeed have oblique components.

Furthermore, using Move, kinematic data was analyzed via stress inversion to calculate the orientations of the principal stress axes associated with the faulting observed in the field, representing a paleo-stress field of the Volcanic Tableland. On a fault surface, the maximum shear direction is indicated by the orientation of slickenlines or striated fault grooves and is inherently related to the orientation of the principal stress axes and the fault plane itself

(Allmendinger et al., 1989; Angelier, 1990). Thus, known kinematic data can be inverted to determine the orientation of the principal stress axes for an array of faults. Move utilizes the direct inversion method described by Angelier (1990); however, there are multiple ways to conduct a stress inversion from field data. The minimum principal stress axis (sigma-3) was used to determine the direction of extension for the field site, and the direction of the intermediate principal stress axis (sigma-2) was compared for parallelism with recorded fault strikes in accordance with Andersonian fault theory (Anderson, 1951).

Data Analysis of Modeled and Observed Fumarolic Pathways

In order to compare the field and modeled data for vertical fumarolic pathways, violin plots comparing the strike values of each data set were produced using the statistical computing software, *R*. This method was chosen to visualize the distribution and the probability density of the data, whereby a box plot showing statistical data (whiskers = minimum and maximum; vertical bar = median; and boxes = interquartile range/middle 50%) is encompassed in a density plot and the width of the density plot is correlative with the frequency of observations. So, peaks on a violin plot indicate the relative probability of observing a value (joint strike) given the distribution of the recorded data. Therefore, any overlap between the two datasets would represent similarities in strike values, and corresponding violin shapes would represent similar probabilities of recording those strike values.

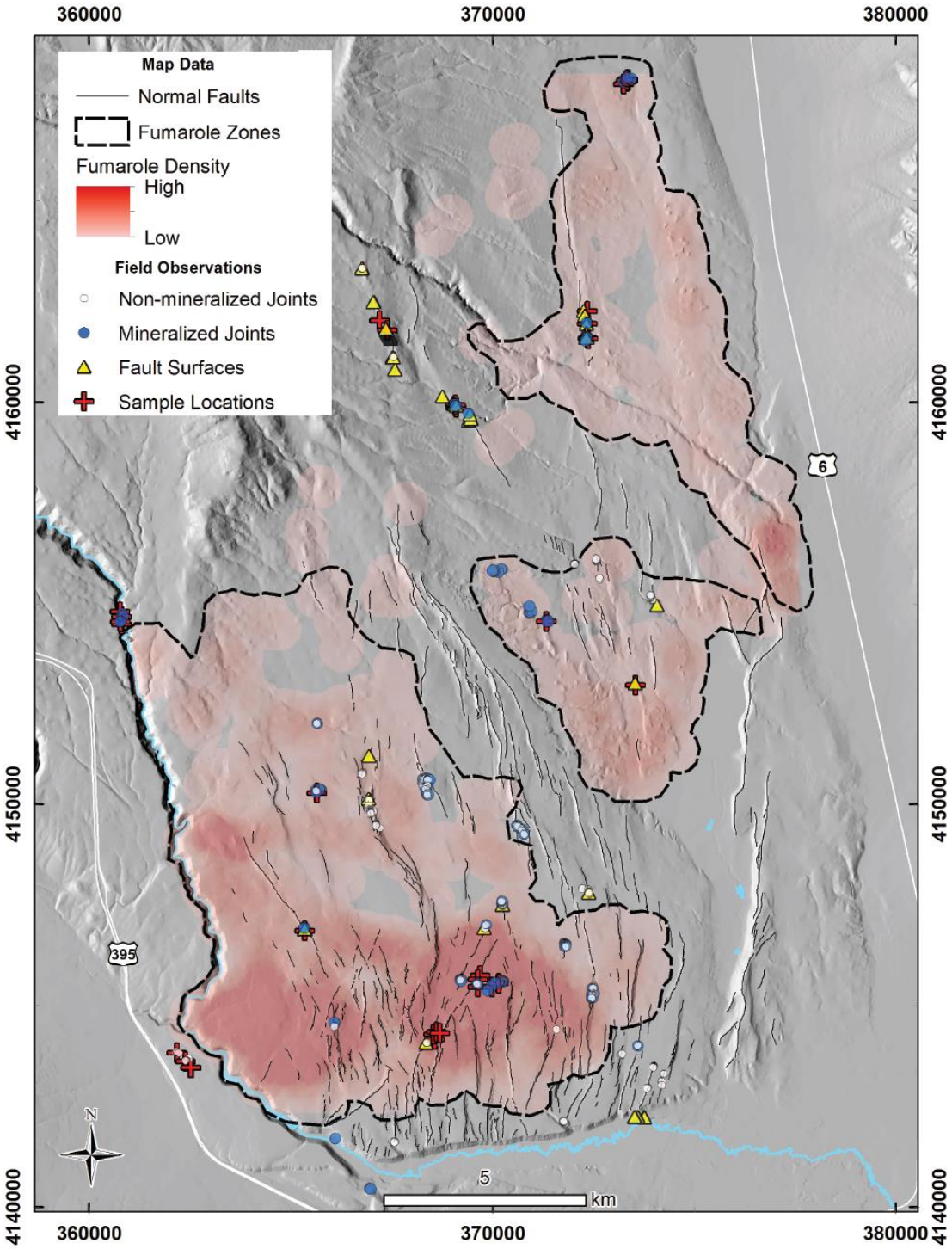

Figure 2.1. Map showing the locations of field observations described in this study (UTM Zone 11 N). The calculated point density of 2,164 mapped fumarolic mounds delineates three zones of fumarolic activity on the tableland. The relative abundance of mounds within each zone is represented by shade (darker areas have more mounds and vice versa). The dips of mapped normal faults (n = 749) can be distinguished by the shade of their scarp on the DEM (sun angle is due west, so lighter scarps are west-dipping and shaded scarps are east-dipping).

CHAPTER 3

RESULTS

Bishop Tuff Descriptions

The upper emplacement unit of the Bishop Tuff (Ig2E) and its three subunits (from bottom to top Ig2Ea-c) that are readily observed atop the Volcanic Tableland north and east of the Owens River gorge differ in their morphology, apparent structures, and degree of welding. Each of the three subunits has varying amounts and sizes (~1-10 cm) of pumice clasts and lapilli, rhyolite lithics, and angular xenolithic fragments of variable lithologies – although, such xenoliths are rare in outcrop. Likewise, the flattening of pumice lapilli varies according to the degree of welding to which the respective subunit was subjected; thus, greater degrees of welding correlate with flattened lapilli (fiammé) and vice versa. In hand sample, all three subunits of Ig2E have visibly apparent grains of quartz and sanidine (mm's in scale). In thin section, the subunits of Ig2E are composed predominantly of quartz, plagioclase, feldspar, opaques, pyroxene, and biotite mineral grains bound in a tuffaceous matrix consisting of fine-grained ash, cuspate glass shards, and pumice clasts. Where the tuff has undergone devitrification, this vitric matrix (ash, glass, and pumice) is notable recrystallized to quartz and feldspar. For further detail on the composition of each subunit and their relative abundances of clasts and lithics, the reader is referred to the research published by Wilson and Hildreth (1997); the following descriptions will focus on each of the three subunits of Ig2E and will follow the same naming conventions established in their publication.

Ig2Ea Description

Outcrop exposures of the lower member of the secondary emplacement unit, Ig2Ea, are present along the southern boundary of the field site. Chalk Bluff road traverses the southern extent of the Volcanic Tableland from east to west (375282.16 m E, 4142386.22 m N to 366670.00 m E, 4141075.00 m N - UTM zone 11N), and the Bishop Tuff thickens accordingly. Much of the exposure immediately along Chalk Bluff road is of non-welded Ig2Ea, where it can be observed to overlie valley fill sediments that would have been relatively cooler at the time of emplacement. In outcrop, thin beddings of fall deposits and reworked volcaniclastics are observed to underlie Ig2Ea at the crucifix site (373712.71m E, 4142238.19m N - UTM zone 11N) near the southeastern terminus of the tableland. Consequently, much of Ig2Ea forms slopes along Chalk Bluff road. Further to the west, however, it becomes partially welded and forms subvertical ledges in the vicinity of Pleasant Valley Dam (365963.87m E, 4141502.11m N – UTM zone 11N) and further up the Owens River gorge. This partial welding of Ig2Ea has been correlated with its deposition atop the still cooling lower emplacement unit (Ig1E) of the Bishop Tuff, however Ig1E is not expressed in outcrop along the southern extent of the tableland (Wilson and Hildreth, 1997).

In outcrop, Ig2Ea has abundant pumice clasts and is pink to light orange in color, taking on more whites and grays on freshly broken surfaces. Ig2Ea is friable where non-welded, and displays minor honeycomb weathering in some exposures. Overall, joints and fault planes are poorly preserved in southern outcrops of this unit, except where partial welding has occurred near Pleasant Valley Dam. Sandy to blocky colluvium mantles much of the slopes that comprise this exposure of Ig2Ea, therefore it is most apparent in outcrop where it is partially welded and forms ledges.

Ig2Ea is also present at the surface of the central and northern regions of the field site, where it directly overlies moderately to densely welded units of Ig1E. Much of Ig2Ea in this area is non-welded and appears to have been subjected to extensive vapor-phase alteration, perhaps best observed in the Hammil Valley (371359.39m E, 4154261.10m N – UTM zone 11N). Therefore, the tuff takes on a bleached, white appearance except where it appears to have been stained red, pink, and orange from the surficial case-hardening of weathered Fe-oxides (Figure 3.1). Structures are well preserved in Ig2Ea in this area despite the extremely friable nature of the tuff. Many fault scarps are sandy because the unit is non-welded; however, fresh fault surfaces with slickenlines were discovered near the top of several scarps (Figure 3.2.D). Vertical joints and fault surfaces are best preserved where the tuff has been case-hardened, which could also be an indication that weathering and/or water transport has occurred along these structures in order to initiate the case-hardening process. Additionally, Ig2Ea has been indurated and mineralized where fumarolic vapors have migrated vertically through the unit.

Ig2Eb Description

Ig2Eb forms the moderately to densely welded cap across the lower half of the Volcanic Tableland. This unit grades from being poorly welded at its base to being densely welded at its top, and thus the morphology of upper portions of Ig2Eb forms cliffs and ledges like those expressed above Chalk Bluff road (366386.55m E, 4141610.86m N – UTM zone 11N). Similarly pumice fragments are present in the lower, less welded parts of the unit and they are flattened, replaced, or eroded completely from the more densely welded cap. Welded zones of this unit are extremely competent, and difficult to break with a rock hammer. Case-hardening also appears to have affected exposed surfaces of Ig2Eb, and is on the order of 1 mm – 1 cm in thickness. Where

this case-hardening has been damaged and the underlying tuff can be eroded more easily, thin shells of indurated material form dramatically shaped outcrops and honeycomb weathering (Figure 3.3). Much of Ig2Eb has a burnt orange and reddish brown color, but in some areas it is nearly black from desert varnish (likely Mn oxides).

Tectonic structures are very prominently exposed in Ig2Eb, with conjugate and cooling joints making up the majority of fractures in the rock mass. Conjugate joints (100's of meters) are an order of magnitude larger than cooling joints (1-10's of meters), and appear to have a greater influence on active structural deformation in the tuff. Likewise, fumarolic mineralization discovered along joint planes indicates that they behaved as pathways for fumarolic vapors being transported to the surface through the densely welded cap of Ig2Eb. Cooling joints in this unit can be observed to curve in strike and dip, and the vast majority have no mineralization to suggest that they behaved as conduits for fumarolic activity, barring some polygonal cracks observed in the immediate vicinity of fumarolic mounds and joints.

The majority of mapped faults on the Volcanic Tableland fall within the extent of Ig2Eb. The degree of welding in this unit helps to preserve entire fault scarps and relay ramps from erosion, making this unit ideal for reconstructing the tectonic history of the tableland. However, nearly all fault scarps in Ig2Eb are mantled with sand, blocky colluvium, and boulders once bounded by cooling joints (Figure 3.2.A). Furthermore, the tops of fault scarps are affected by cooling joints in the densely welded cap of Ig2Eb, resulting in a zigzag pattern of densely welded tuff along fault strikes. These irregular fault traces and eroded scarps make it difficult to find fresh fault surfaces that preserve slickenlines in this unit; thus, slickenlines are best preserved in densely welded Ig2Eb where preexisting joints (often large conjugate joints) parallel fault strikes (Figure 3.2.B-C).

Ig2Ec Description

Ig2Ec represents the uppermost, and youngest, subunit of the Bishop Tuff emplaced on the Volcanic Tableland. This unit is preserved in the central and northern areas of the field site where there was extensive fumarolic activity and vapor-phase alteration (374587.04m E, 4164576.13m N – UTM zone 11N). Thus resilient fumarolic mounds and ridges in this area represent non-welded tuff that was indurated and mineralized by vapor-phase alteration. As this unit has not been welded, its competency solely derives from its mineralization associated with vapor-phase/fumarolic activity. This mineralization is most common as an ~ 10mm thick rind that coats surfaces of Ig2Ec that were presumably exposed to fumarolic vapor condensate. For this reason, the morphology of fumarolic mounds has both indurated cobbles and plating (often polygonal resembling cooling cracks) that serve in armoring the mound from further erosion. When non-welded material is eroded from beneath this rind, a remnant shell of fumarolically altered, case-hardened material is left behind.

When compared to the other subunits of the Bishop Tuff, Ig2Ec does not exhibit the same degree of muted orange, pink, and red hues. Rather, Ig2Ec is predominantly white and grey with very minor shades of blue, purple, pink, and brown. This appears to be related to the silica-rich mineralized rind on most samples. When broken, the non-welded tuff beneath the rind is often bleached white from vapor-phase alteration. Rhyolitic lithics in this subunit are abundant, and pumice clasts are often lapilli sized, rarely exceeding 5 cm in length. Black desert varnish is also common on this subunit, on which many petroglyphs have been created by ancient cultures (Figure 3.4).

Secondary Mineralization

Since emplacement, the Bishop Tuff has undergone multiple episodes of secondary mineralization that include the alteration of the tuff itself and the deposition of pedogenic mineral phases. Vapor-phase alteration and fumarolic activity notably alter the mineral grains and tuff matrix to a microscopic level. Conversely, the pedogenic deposition of caliche has little effect on the tuff, rather it accounts for the addition of lithics (mostly sand grains) in calcareous cement. Apart from the crystallization of minerals from volcanic glass in devitrified units of the tuff, secondary mineralization appears to be solely concentrated along preexisting discontinuities of variable scales.

In the field, welded and devitrified tuff (e.g. Ig1E) is present beneath zones of vapor-phase alteration, highlighting a relationship that exists between the processes of devitrification and vapor-phase alteration. In thin section, welding is identified by the flattening of glass shards and pumice fragments (fiammé), and devitrification is apparent where glass shards have been notably replaced by quartz (Figure 3.5). As noted previously through the discovery of mineralized joint planes, vapor-phase activity was directed to the surface of the Volcanic Tableland via an extensive network of conjugate joints, forming fumarolic features. In the immediate vicinity of fumarolic mounds and ridges, structures of all scales (including small polygonal cooling cracks) may be mineralized (Figure 3.6), and many features have a lighter halo of vapor-phase alteration around their circumference. This mineralization forms indurated rinds on tuff surfaces that seemingly came in contact with fumarolic vapors and/or vapor condensate. These rinds represent where the vitric tuff matrix has been replaced with microcrystalline quartz, giving it a conchoidal fracture relative to the unaltered tuff (Figure 3.7). XRF analysis of fumarolic rinds indicates higher counts of silica and calcium than in non-

mineralized samples. They are commonly ~ 10 mm or less in thickness, but larger rinds can be observed in the field. This thin rind suggests that not all fumarolic vapors were gases, rather it seems that there was an aqueous phase also expelled by the fumaroles. Most likely these exiting vapors condensed in order to indurate three-dimensional ridges of otherwise non-welded tuff. Most of the fumarolic mineralization is grey (light-dark) with lesser amounts of pale colors (pink, blue, red); however, some features closely resemble the color of the tuff that's been altered and take on a more orange and brown hue. The nature of this mineralization appears to be the same across the three distinct zones of fumarolic activity identified on the tableland.

In aerial imagery, there is a clear relationship between fumarolic features and structures (conjugate joints and faults) across the southern half of the tableland, where Ig2Eb forms a densely welded cap (Figure 3.8). Fumarolic mounds and ridges are frequently aligned in preferred northeast and northwest trends along the strike and intersection of conjugate joints. In several areas, fumarolic mounds are aligned along fault lines and have been cut by subsequent deformation, indicating that faults were also capable of vertically communicating fumarolic vapors and that faulting occurred while hydrothermal activity was ongoing. In the northern half of the field site, however, this relationship becomes less apparent as friable non-welded units (Ig2Ea and Ig2Ec) appear to obscure the structures that once served as pathways for fumarolic vapors. Field observations confirm that fossil fumarolic features in this area are still related to joints and faults in the tuff, thus this relationship appears to be ubiquitous across the field site.

One exception to this relationship is the fumarolic area north of Casa Diablo road (370182.60m E, 4149725.03m N - UTM zone 11N), where fumarolic activity appears to have occurred along late stage curvilinear cooling joints located on the margin of the buried basin identified by gravity surveys (Pakiser et al., 1964; Saltus and Jachens, 1995). Here, fumarolic

ridges resemble a curvilinear latticework along connected traces of cooling joints (Figure 3.8). Mineralization along these curvilinear fumarolic ridges bears all the same characteristics as fumarolic features found elsewhere in the field site, with a silicified rind indurating the ridges relative to the surrounding tuff.

The other, more pervasive form of secondary mineralization displayed on the Volcanic Tableland is a white caliche that coats fracture surfaces of all scales (loose cobbles, fractured rock mass, cooling joints, columnar joints, conjugate joints, and faults) (Figure 3.9). The caliche can form a variety of textures ranging from corraloidal, botryoidal, dendritic, and laminar, which all appear to be a function of available void space and deposition mechanism. Likely pedogenic in origin, the caliche cement ($CaCO_3$) appears to have been transported to the Volcanic Tableland (perhaps from wind blown sediments or precipitation) due to the lack of calcium present in the tuff substrate. Along fault planes and joint surfaces, caliche is most often laminar, apparent as thin beds of rounded lithics bound in calcareous cement. This laminar texture indicates that meteoric water played a role in transporting the caliche constituents along these fracture planes. Due to its pervasive nature, slickenlines are often preserved in caliche along fault surfaces. In fact, some structural overprinting of slickenlines was observed along fault surfaces where caliche was deposited laminarly, thereby preserving unique kinematics in separate laminations of caliche. The relative timing and deposition of caliche with regards to faulting appears to have been variable, whereby some non-mineralized fault grooves are overlain by undeformed caliche and some fault surfaces display slickenlines in the caliche itself. Regardless, the deposition and formation of caliche on the tableland appears to have begun early after the emplacement of the Bishop Tuff, in some instances occurring before or simultaneously with faulting.

Petrography

In total, nine thin sections were prepared from the 37 hand samples collected in the field. Four thin sections were selected for the petrographic analysis and description of fumarolic alteration and devitrification in the tuff. Overall, the tuff displays a pyroclastic texture, whereby mineral grains (mm), pumice clasts (mm-cm), and lithic fragments (mm-cm) are bound in a vitric tuff matrix consisting of glass shards (cuspate or flattened) and fine-grained volcanic ash. Mineral grains in the tuff are millimeters in scale and the majority display subhedral shapes, while some approach more euhedral and anhedral shapes. These grains consist predominantly of quartz, plagioclase, and feldspar; although, biotite and pyoxrene are present in lesser amounts. Nearly all mineral grains in the tuff have been fractured and pumice clasts are often rounded (figure 3.7.B), which are likely products of the pyroclastic nature of their deposition. Sub-millimeter opaques are common in the vitric matrix and display anhedral shapes.

As the processes of welding and devitrification in the lower unit of the Bishop Tuff are believed to have led to the development of volatiles that were expelled during subsequent vapor-phase (fumarolic) alteration (Sheridan, 1970; Vaniman, 2006), composite photomicrographs showing the welding and devitrification characteristic of the lower emplacement unit of the tuff (Ig1E) were produced (Figure 3.5). Welding can be readily identified by the alignment of tuff constituents (mineral grains, pumice clasts, and glass shards) apparent in Figure 3.5.A. Devitrification can be identified by the recrystallization of glass shards and volcanic ash to quartz (and perhaps feldspar), as is shown in Figure 3.5.B. This recrystallization is best described as fine-grained axiolitic and spherulitic mineral growths extending inward from shard walls. Thus, these characteristics represent the processes that preceded fumarolic activity on the tableland, and behaved as a source of fumarolic volatiles.

In fumarolic samples, vapor-phase alteration is apparent where the vitric matrix has been overprinted with birefringent microcrystalline quartz, defining a distinct contact in the form of a silicified rind (Figure 3.7.B-C). XRF analysis confirms an increase in silica content on these rinds relative to the adjoining and unaltered tuff, despite being calibrated to identify potential K-bearing minerals (Figure 3.7.A). However, for future work, the use of X-Ray Diffraction (XRD) is recommended to better identify the minerals associated with fumarolic alteration. As samples were collected from the surface of the tableland where fumarolic alteration effected non-welded tuff, the original vitric texture (non-welded cuspate glass shards) is often preserved in these rinds. Some larger mineral grains in silicified rinds have developed haloes of recrystallized glass or quartz (Figure 3.7.C). Furthermore, a "bleached" zone is commonly observed along the contact between this silicified rind and the unaltered tuff, where the vitric matrix appears to be lighter than the adjoining matrices but does not display the same microcrystalline mineralization as the rind (Figure 3.7.B - white dashed line).

Fault Surface Morphology

Field efforts resulted in the discovery of 31 well-preserved fault localities that have not been described in previous research on the Volcanic Tableland. These localities are distributed across the field site, and each contains many distinct fault surfaces for analysis. The morphology for each of these newly identified fault surfaces varied according to their corresponding emplacement subunit.

In the northern half of the tableland, where non-welded Ig2Ea and Ig2Ec are exposed at the surface, nearly all fault surfaces were identified in the upper half of exposed hanging walls. Erosion and sedimentation have obscured or destroyed many of the original fault surfaces in the

non-welded tuff, and the remaining exposures are often on the order of centimeters to meters in scale, however the largest continuous fault surface discovered in this area was ~ 235 m long (Figure 3.10). Fault surfaces are indurated relative to tuff in their immediate vicinity, which is a function of minor gouge formation along the slip surface and/or case-hardening from thin mineralized coatings of Fe-oxides that stain the surface orange and brown. Desert varnish also appears to be present on some exposures. A typical fault surface in this area of the tableland exhibits grooves and slickenlines in white caliche encrustations. Some fault surfaces even display a pre-rupture soil profile indicative of relatively recent deformation (Figure 3.11).

In the southern half of the tableland, fault surfaces are preserved along reactivated joint faces (cm to m in scale) in moderately to densely welded (Ig2Eb) tuff. Mapped faults in this area are sub parallel with the strike of existing conjugate joints or curve to intersect conjugate joints near their tips, forming dihedral V-shaped fault terminations (Figure 2.1, and 3.8). This indicates that faulting occurred along preexisting structural weaknesses in the ash-flow sheet. Furthermore, mapped fault traces vary from having a single isolated scarp to an anastomosing arrangement of scarps. On a finer scale, fault scarps display a similar pattern whereby their trace follows the preexisting structural fabric of the jointed rock mass. Therefore, fault surfaces were discovered where jointing (conjugate or cooling) approaches parallelism with fault strike, allowing for shear to occur along joint planes. Given this mechanism, the fault surfaces in this area are often vertical to sub-vertical according to the orientation of the preceding joint (Figure 3.3.B-C). As exposed tuff in this area is moderately to densely welded, fault surfaces are predominantly grooved and show little evidence of fault gouge. Slickenlines are present where caliche has been deposited from fracture flow occurring along fault and joint surfaces.

Furthermore, sinistral horizontal chatter marks were observed at one outcrop in the field, although they are not a common feature of fault surfaces in the area (Figure 3.12.E).

Across the field site, normal and oblique faults are more numerous and larger in scale than faults classified as being strike-slip. Normal and oblique faults have notable vertical offsets ranging from ~ 1 – 145 m and preserve large footwall scarps. However, lateral offsets along strike-slip faults were not visible in the field due to the poor outcrop of fault traces along the surface of the tableland (likely buried beneath loose sediment). Likewise, the homogenous composition and appearance of the tuff precludes identifying any offset that is not a structural discontinuity. Identifying strike-slip surfaces where both fault blocks remain intact is also complicated given their similar conjugate geometry and orientations to vertical conjugate joints. Thus, all strike-slip fault surfaces were discovered where one side of the fault had been exposed by erosion, block collapse, or minor oblique offset from shallow plunging slip.

Fault Kinematics

In total, the orientations of 267 kinematic indicators and corresponding fault surfaces were recorded from 31 fault localities for kinematic analysis (Figure 2.1; Table 1). On average, fault planes strike N 21^{o} W and dip between 53^{o} and 89^{o}. Following the simplified Zoback criteria for classifying faults, 197 of the recorded faults were dip-slip, 49 were oblique-slip, and 21 were strike-slip (Zoback, 1992; Boore et al., 2013). However, structural overprinting was observed along several fault surfaces (Figure 3.12.D). The orientations of slickenlines and grooves was dependent upon fault type, and plunges varied between 0^{o} and 88^{o} depending upon fault dip.

A stereonet plotting striae, slip-sense, and fault planes of the kinematic data recorded in the field is presented in (Figure 3.13). The stereonet indicates that there are at least 3 modes of faulting on the Volcanic Tableland. Normal faults have moderate dips, strike to the NW, have striae plunges that approach the center of fault planes, and display a slip-sense that is perpendicular to sub perpendicular from fault strike. Strike-slip faults approach vertical dips, strike both NE and NW, have shallow-plunging striae that fall near the outline of the plot, and display a slip-sense nearly parallel with fault strike. Oblique-slip faults approach vertical dips, vary in strike from NE to NW (apparently a combination of strikes also observed with strike-slip faults and normal faults), have steeply plunging striae that fall near the center of the plot, and display a slip-sense that departs from strike at an acute angle. Composite fault plane solutions of these modes of faulting are also included in Figure 3.13.

Dip-Slip Faults

Faults identified as being dip-slip (n = 197) have an average strike of N 23^{o} W and dip between 53^{o} and 87^{o} (averaging ~ 65^{o}) slightly to the southwest and northeast. In total, 188 of these fault surfaces are west-dipping and 9 are east-dipping. The average orientation of striae on these dip-slip surfaces has a trend of 243^{o} and plunge of ~ 64^{o}.

Oblique-Slip Faults

Faults identified as exhibiting oblique-slip (n = 49) display two modes with average strikes of N 28^{o} W and N 31^{o} E. Their dips are between 77^{o} and 89^{o}, averaging ~ 85^{o}. In total, 42 of these fault surfaces are west-dipping and 7 are east-dipping. Striae on these fault surfaces have variable trends and an average plunge of ~ 75^{o}.

Strike-Slip Faults

Faults identified as displaying strike-slip kinematics (n = 21) have two modes with average strikes of N 30º W and N 43º E. Their dips are between 73º and 89º, averaging ~ 85º. In total, 16 fault surfaces are west-dipping and 5 are east-dipping. Striae along strike-slip faults have trends nearly parallel to strike and an average plunge of 16º. Striae along northwest-striking faults plunge shallowly to the northwest and southeast, while striae on northeast-striking faults plunge shallowly to the northeast and southwest.

Stress Inversion of Kinematic Field Data

A stress inversion of kinematic data from the field was performed using Midland Valley's Move software in order to determine the orientation of the stress state that best accounts for the structural deformation manifested on the Volcanic Tableland. This paleostress analysis yielded the results shown in Figure 3.14.A. The data reveal stress tensors indicating that normal and oblique faulting have been the dominant modes of deformation occurring on the tableland because the resulting maximum principal stress component (σ_1) is subvertical, trending 255º and plunging 79º. The minimum principal stress component (σ_3) is subhorizontal, trending 76º and plunging 11º, and its axis is parallel to ENE and WSW extension. The intermediate principal stress (σ_2) is horizontal and trends 346º, roughly parallel with the average strike of recorded faults (339º). These stress tensors are coincident with the faulting and kinematic indicators observed in the field.

In order to better understand the strike-slip faulting observed in the field, a stress inversion was performed using the 21 recorded strike-slip faults and lineations (Figure 3.14.B). The resulting maximum principal stress (σ_1) is horizontal and bisects the conjugate NE and NW strike-slip fault planes, trending 12°. Similarly, the least principal stress (σ_3) is horizontal and it's axis parallels lateral ESE and WNW extension, trending 102° and plunging less than 3°. The intermediate principal stress (σ_2) is vertical, trending 281° and plunging 87°.

The stress tensors associated with vertical fault motion were determined via a stress inversion of the 197 normal faults, and 49 oblique faults recorded in the field (Figure 3.14.C). The resulting maximum principal stress (σ_1) is subvertical (plunging 78°) with a trend of 72°. The least principal stress (σ_3) is subhorizontal and it's axis parallels lateral ENE and WSW extension, trending 258° and plunging less than 12°. Lastly, the intermediate principal stress (σ_2) is horizontal (plunging 1°) with a trend of 168° which is subparallel with the strike of normal faults (N 23° W) and the bisector of oblique faults (modes of N 28° W and N 31° E).

Furthermore, the relative slip tendencies produced from the stress inversion of each fault population serve to support the credibility of the inversion results and simplified Zoback criteria of fault classification (Zoback, 1992; Boore et al., 2013). The slip tendencies are plotted on each stereonet as color gradations that indicate the relative likelihood (high = reds and yellows, low = blues and greens) and direction of slip occurring on surfaces of all orientations given the stress state produced via the inversion of field data (Figure 3.14.A-C). Thus, fault poles (black crosses) on each stereo plot that overlap with warmer colors (reds and yellows) of slip tendency represent faults that are more likely to experience slip given their respective calculated stress state. Given faults were classified via the simplified Zoback criteria, and the majority of fault poles for classified strike-slip faults (Figure 3.14.B) and normal-oblique faults (Figure 3.14.C) plot within

regions of higher slip tendency, this supports using the simplified Zoback criteria to classify fault populations.

Joints and Fumarolic Pathways

The following three types of joints were identified on the Volcanic Tableland during fieldwork: columnar joints, cooling joints, and conjugate joints. Columnar joints are best preserved along the central and upper portions of Owens River Gorge, where they are exposed in cross-section (Figure 3.15). Columns are between one and two meters in diameter and extend for 10's of meters in length. They are most common in the upper units of the Bishop tuff that have been subjected to vapor-phase alteration associated with overlying fumarolic activity at the surface of the tableland. Columns display an array of vertical to subhorizontal orientations and are the physical manifestation of heat flow patterns (perpendicular to isothermal gradients) as the tuff sheet was cooling (Sheridan, 1970). Columnar joints often radiate outwards from large vertical joints to form a flower structure in cross-section (Figure 3.16). The curvature of columns near the center of these rosettes suggests steeper isothermal gradients were present along the vertical joint at their center, representing a fumarolic pathway. Secondary mineralization in the form of microcrystalline quartz and caliche were observed along columnar joint planes in the field (Figure 3.17).

The most common joints are cooling joints, which are often between 5 and 10 meters in length and isolate large boulders of moderately to densely welded tuff across the southern half of the tableland. They have been described as cooling joints because their orientations are asystematic, curving in strike and dip, and intersecting each other at near orthogonal angles suggesting thermal stress release (Figure 3.18). Near the exposed free surface of the tableland

they often exhibit subvertical dips that shallow increasingly with depth until they terminate at ~ 5-10 meters. Apart from an area north of Casa Diablo road (Figure 3.8), these joints do not appear to have behaved as fumarolic pathways given pedogenic caliche is the only form of secondary mineralization that is commonly observed along cooling joint planes. In the immediate vicinity of fumarolic features meter-scale polygonal crack patterns are often mineralized; although, these features are smaller than common cooling joints and may instead represent incipient fractures from fumarolic activity.

In the field, the orientations of 440 non-mineralized cooling joints were recorded near the surface of the tableland, where their dips were subvertical. On average, cooling joints had a strike of N 6^{o} W and dip of 81^{o}; however, it is important to note that variability was apparent in strike and dip for each plane's measurement. In general, the data suggests that non-mineralized cooling joints have a roughly equal probability of striking in any direction, due to the lack of definitive peaks on the violin plot in Figure 3.19. Although, there is a slight preference of strikes occurring N 60^{o} W that is evident on the violin plot (peak at 120^{o}) and rose plot showing the distribution of joint strike observations (Figure 3.19).

The largest joints occurring on the Volcanic Tableland are vertically dipping conjugate joints that strike NE and NW. Across the southern half of the field site, where they are best exposed, they can be mapped to extend for hundreds of meters along strike and can be observed to extend vertically up to ~ 100 meters in the Owens River Gorge (Figure 3.16). The mapped alignment of fumarolic mounds on the tableland, the development of rosette columnar joints adjoining vertical conjugate joints in cross-section, the expression of fumarolic ridges, and the mineralization of conjugate joints all serve as lines of evidence that many of the conjugate joints once behaved as fumarolic pathways in the Bishop Tuff. Therefore, in outcrop, conjugate joints

are recognized by their lateral continuity, vertical dips, and fumarolic alteration (where present). In total, the orientations of 397 mineralized joints were recorded in the field. Upon plotting the strikes of mineralized joints on rose plots, their distribution indicates that values cluster between NW and NE strikes and display a minor clustering from E to W (Figure 3.19). The data distribution and probability density displayed on the corresponding violin plot (Figure 3.19) suggests that fumarolic mineralization occurred primarily along conjugate joints that have a relatively higher probability of striking between N 30^o W and N 38^o E than striking at other azimuths. When their orientations are averaged, mineralized joints yield a strike of N 2^o E and a dip of 83^o, which roughly bisects the acute dihedral angle between NE and NW striking conjugate joints. Furthermore, the horizontally oriented maximum principal stress axis (σ_1) produced from the stress inversion of strike-slip data also appears to bisect the conjugate mineralized joints (Figure 3.20).

Model Results

Three-dimensional fault plane surfaces produced from earthquake hypocenters of the 1986 Chalfant Valley earthquake sequence were assigned the following nomenclature: Chalfant Valley Fault (CVF), Tungsten Hills Fault (THF), and White Mountain Fault Zone (WMFZ) (Figure 3.21). Gradational color schemes on the produced three-dimensional fault surfaces represent the tapering of slip outwards from the centroid of each fault towards the fault tips (Figure 3.21). Modeled fault surfaces were not strictly planar, and smoothed areas with curvature and asperities exist along each fault surface that result in minor changes to strike and dip along the trace of modeled faults. On average, the produced fault surfaces had the following

orientations: CVF – striking N 153° E, dipping 45°; THF – striking N 140° W, dipping 55°; WMFZ - striking N 170° E, dipping 70°.

In order to replicate the enhancement of vertical fumarolic pathways by strike-slip activity, slip was modeled along each fault plane according to the parameters exhibited during the 1986 Chalfant Valley earthquake sequence to produce a set of 397 synthetic joints that would become dilated given the simulated stress field. This sample size was selected to match the number of recorded mineralized joints from the field (n = 397). These synthetic joints were assigned vertical dips (90°) and lengths of 500 meters to mimic their fumarolic joint counterparts observed in the field. The spatial distribution of these joints is mapped in Figure 3.21, which was selectively cropped to the extent of the Volcanic Tableland. Given the simulated stresses, the average optimal strike of joints that would become dilated is N 1° E, which bisects the bimodal distribution of NE and NW joint strikes identifiable on the rose plot in Figure 3.21. The probability density function of the synthetic joints is distributed such that there is a sharp increase in the likelihood of recording strike values between N 30° E and N 30° W (Figure 3.20). These values are consistent with the orientations of mineralized joints recorded in the field, which also have an increased likelihood of striking between N 30° W and N 38° E.

Furthermore, the synthetic joints appear to be bisected by the horizontal maximum principal stress component (σ_1) generated from the stress inversion of strike-slip fault surfaces observed in the field. This finding indicates that the synthetic joint dataset is compatible with the kinematic record of strike-slip faulting preserved in the Bishop Tuff.

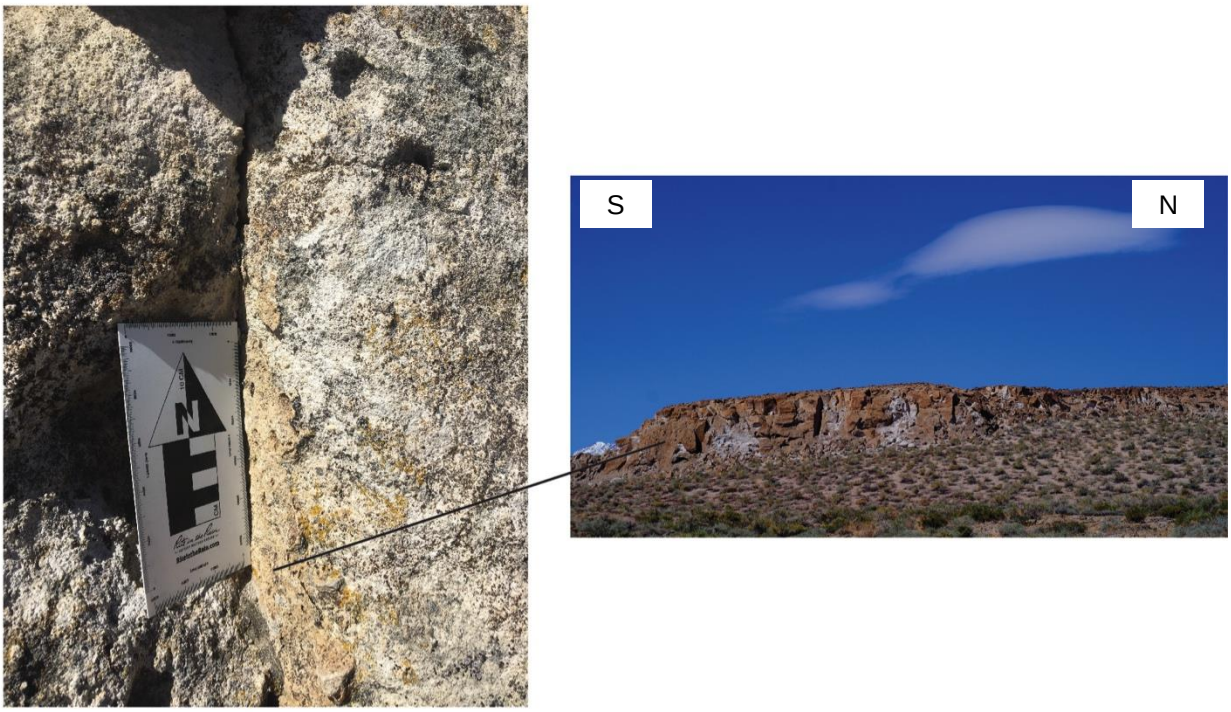

Figure 3.1. Case-hardening (primarily red Fe-oxides) of nonwelded tuff (Ig2Ea) in the central and northern regions of the Volcanic Tableland (e.g. Hammil Valley). These thin (mm-scale) coatings serve to increase the competency of tuff along joint planes and exposed surfaces.

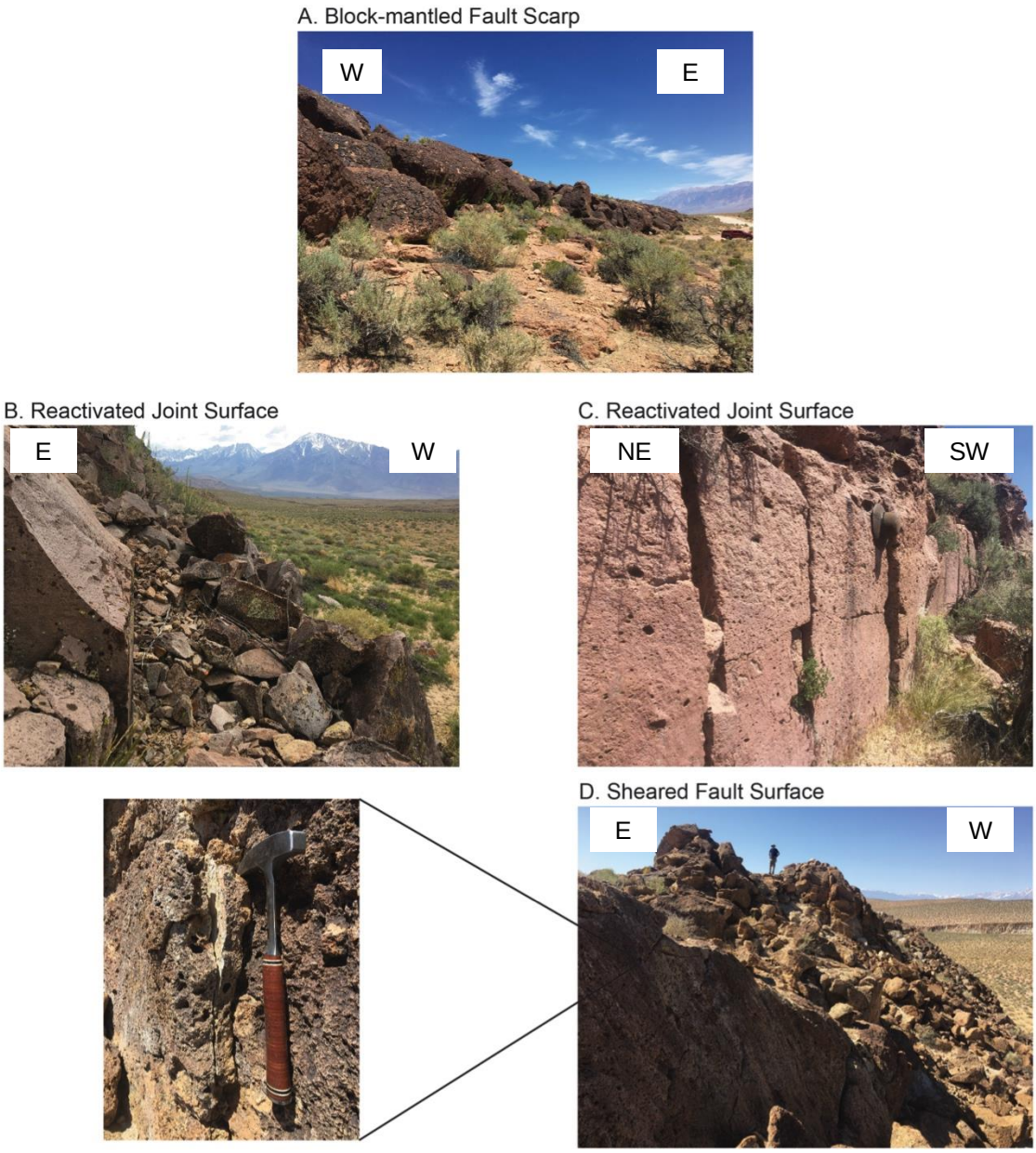

Figure 3.2. Fault scarp and surface morphology of the tableland. (A) a typical block-mantled fault scarp in Ig2Eb across the southern half of the field site (truck for scale). These blocks appear to have been bounded by shallow cooling joints, allowing them to become incorporated into scarp colluvium with the progression of fault displacement. (B and C) Vertical joint surfaces in partly to densely welded tuff (Ig2Eb) that have been reactivated by faulting and display groove lineations (hat for scale). (D) Fault surfaces in non-lightly welded tuff (Ig2Ea) that appear to have formed from cataclastic shear (lefthand photograph: note thin band of cataclasis on the margins of the slicked fault surface – rock hammer for scale). These fault surfaces are characteristic of those discovered on the northern half of the tableland. Also note the similarities in fault scarp morphology to (A), whereby cooling joint-bounded blocks mantle the scarp slope; however, the blocks themselves are much smaller than those in the more competent partially-densely welded Ig2Eb (advisor for scale).

Figure 3.3. Weathering and case-hardening (Fe and Mn oxides) of Ig2Eb across the southern half of the Volcanic Tableland. Where less competent, partially welded tuff has been eroded beneath the case-hardened rind, the tuff displays odd shapes and honeycomb weathering. These textures are what have made the area popular for rock-climbing.

Figure 3.4. Black desert varnish (Mn-oxides) common on exposed Ig2Ec tuff across the northern half of the tableland. When broken, this unit has been bleached white by vapor-phase alteration. This desert varnish allowed for the creation and preservation of ancient cultures' petroglyphs, some of which are estimated to date back over 8,000 years.

Welded and Devitrified Tuff

A.

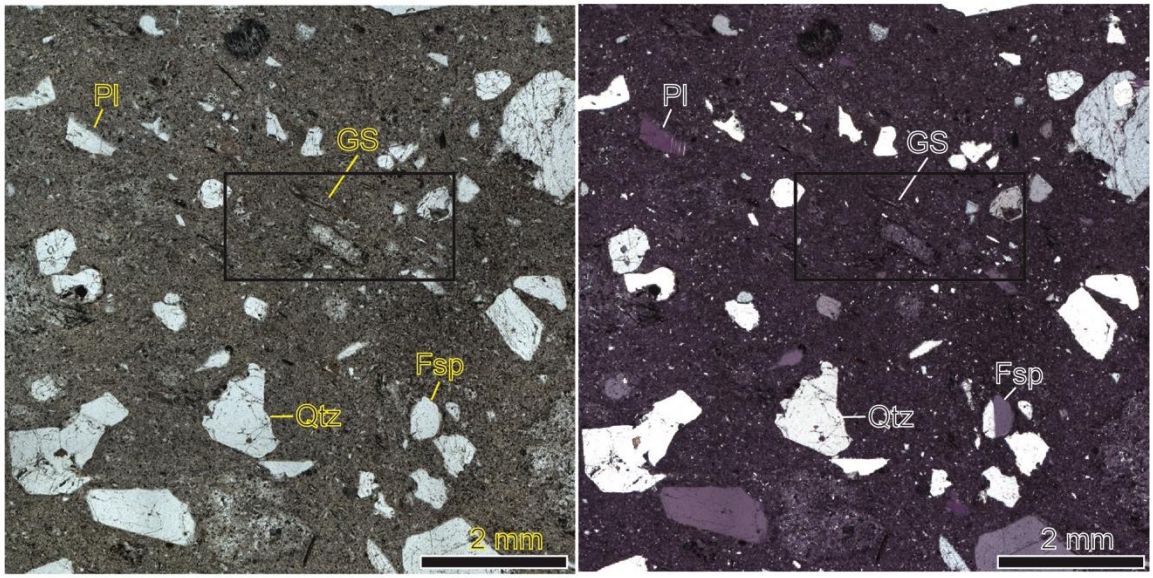

B.

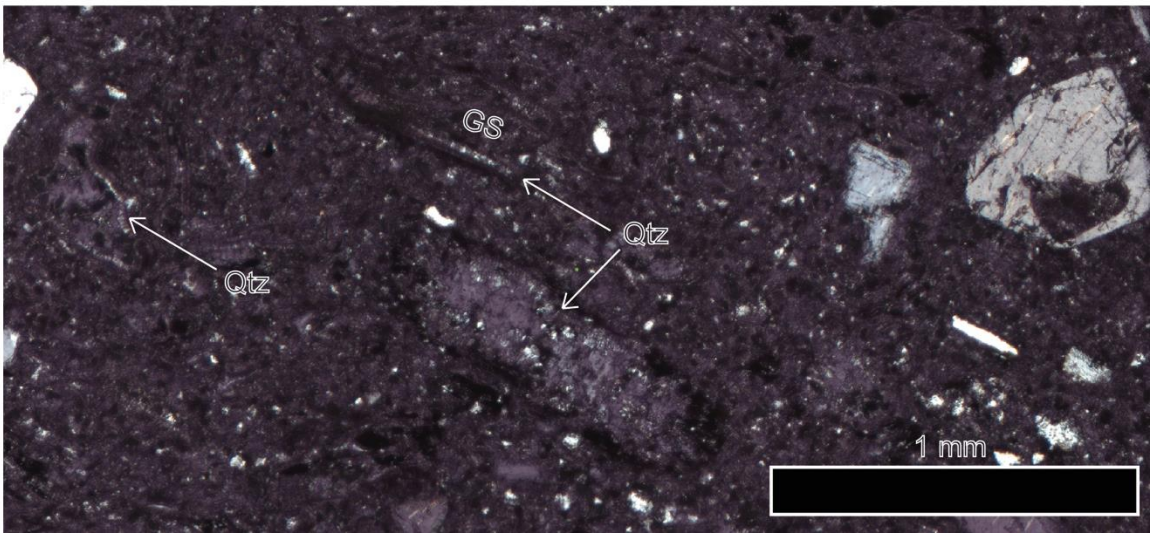

Figure 3.5. Composite photomicrographs of the welded and devitrified tuff (Ig1E) that is observed to underlie vapor-phase altered Ig2Ea in Owens River Gorge. (A) Thin section under plane light and crossed-polars. Note the horizontal alignment (top left to bottom right) and flattening of glass shards and mineral grains that indicate that the tuff is welded. Abbreviations: Fsp – feldspar, GS – glass shards, Pl – plagioclase, Qtz – quartz. (B) Magnified view of tuff matrix under crossed-polars. Note how the flattened glass shards have been crystallized to quartz and display axiolitic texture inwards from the shard walls. These features are characteristic of devitrification, which is believed to have formed the vapors that were released during fumarolic activity, leading to the vapor-phase alteration of overlying partial to non-welded tuff.

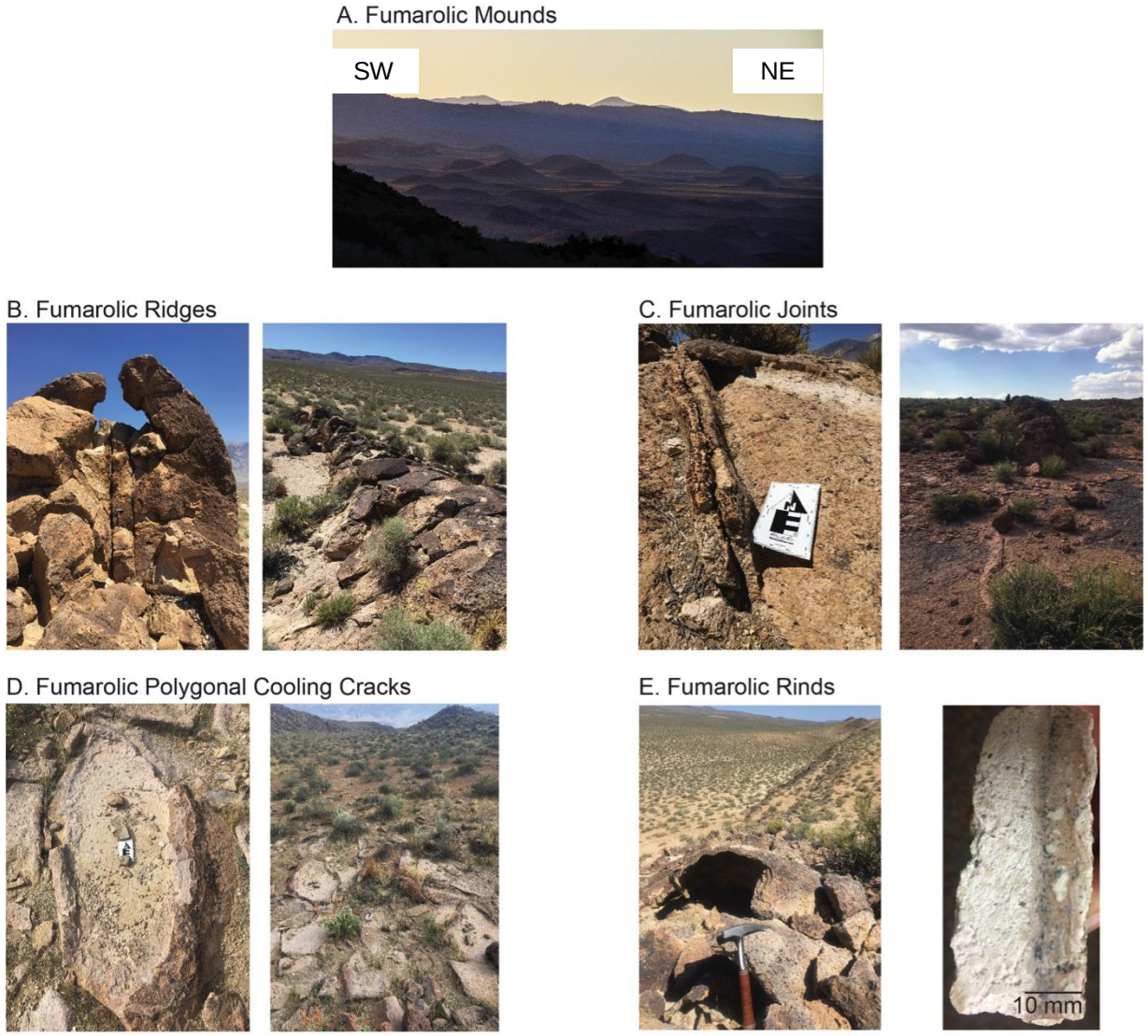

Figure 3.6. Fumarolic features of the Volcanic Tableland. (A) Fumarolic mounds of Hammil Valley rising up to 30 m in relief. (B) Fumarolic ridges viewed in cross-section and topographic relief (rock hammer for scale). Note the master joint that served as the pathway for escaping fumarolic vapors and condensate, and the rounded relief of the ridge. (C) Fumarolic joints identified by their common NE-NW strike, and indurated lip (10's mm thick) of silicified tuff. The photo on the right shows a fumarolic joint in the foreground extending to become a fumarolic ridge in the distance. (D) Blistered morphology of fumarolically altered cooling cracks in the vicinity of fumarolic mounds. Their curvilinear polygonal shapes and small scales indicate that fumarolic vapors and condensate leaked diffusely through the rock mass in the mound's vicinity. (E) Fumarolic rinds typical of fumarolic mineralization, displaying a silicified groundmass ~10 mm in thickness along surfaces exposed to fumarolic activity. Less indurated and nonwelded tuff beneath the rind can be preferentially eroded, leaving behind hollow shells of fumarolic material.

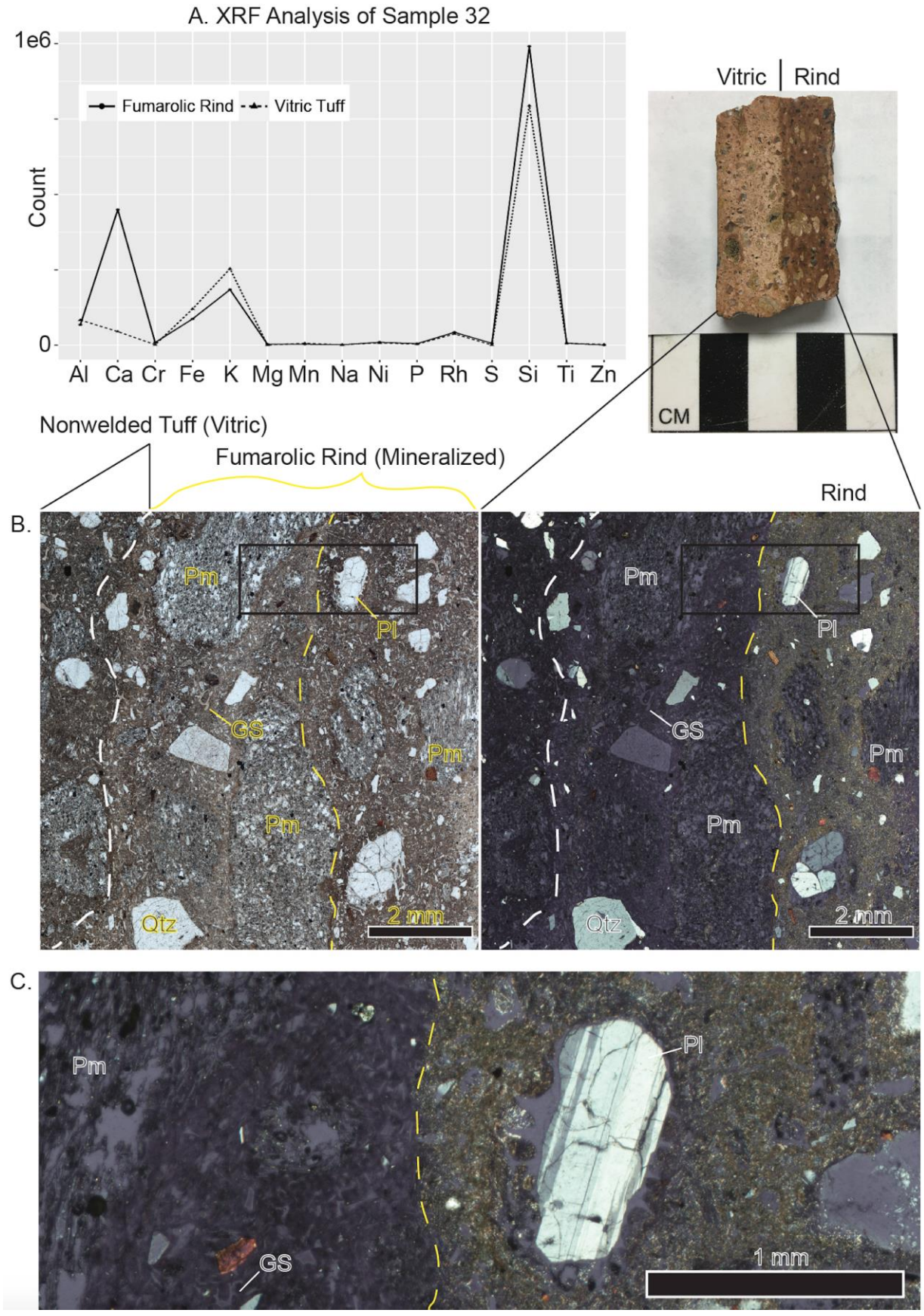
A. XRF Analysis of Sample 32
1e6
0
Count
Fumarolic Rind
Vitric Tuff
Al Ca Cr Fe K Mg Mn Na Ni P Rh S Si Ti Zn
Vitric
Rind
CM
Nonwelded Tuff (Vitric)
Fumarolic Rind (Mineralized)
Rind
B.
Pm
Pl
GS
Qtz
2 mm
C.
1 mm

Figure 3.7. (A) Elemental counts of the fumarolic rind and unaltered vitric tuff of sample 32 (Ig2Ea), recorded via XRF analysis. Note the higher abundance of Si counts of the fumarolic rind (solid line), compared to the non-mineralized vitric tuff (dashed line). As this sample was collected from a fumarolic joint (rind exposed) the greater of abundance of Ca is likely due to the influence of caliche. The presence of Rhodium is an artifact stemming from the Rhodium anode of the handheld XRF. (B) Composite photomicrographs of thin sections in plane and crossed-polarized light. Dashed lines represent the extent of fumarolic mineralization (yellow = extent of microcrystalline quartz matrix, white = extent of "bleached" zone). The photomicrographs are oriented similar to the billet shown above, whereby the fumarolic rind is located on the right and mineralization tapers from right to left. Note the apparent infiltration of microcrystalline quartz into the void space of pumice fragments in the silicified rind. Abbreviations: GS – glass shard, Pl – plagioclase, Pm – pumice, Qtz – quartz. (C) Magnified view of the fumarolic rind in crossed-polarized light. Here, the plagioclase grain (Pl) is rimmed by gray recrystallized glass and birefringent microcrystalline quartz. A similar feature is located above the scale bar in (B). Note how the microcrystalline quartz appears to have preferentially altered the fine-grained ash matrix, leaving the cuspate glass shards (gray) apparently unaffected. These glass shards have the same appearance as those in the "bleached" zone on the left-hand side of the photomicrograph (GS), and they indicate that the tuff is vitric (has not been devitrified).

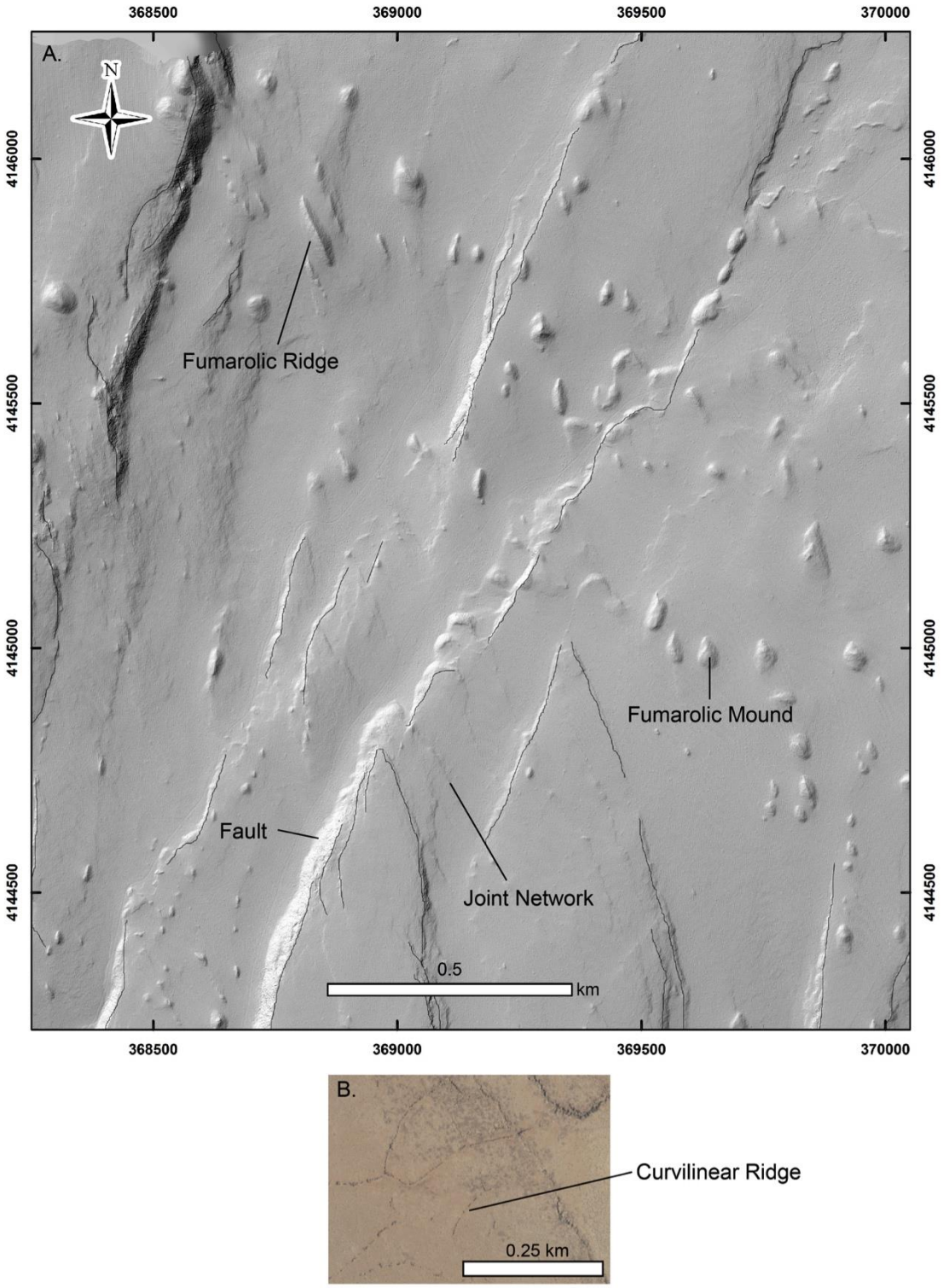

Figure 3.8. (A) Map showing the distribution of fumarolic features (mounds and ridges) relative to tableland structures (faults and joints). Note the conjugate NE and NW trends evident in joints, faults, and the alignment of fumarolic features. (B) Curvilinear fumarolic ridges in the central tableland. These features suggest that some fumarolic activity occurred along cooling joint networks.

Figure 3.9. (A-C) The three common textures of caliche mineralization in the Bishop Tuff. Note the laminar vein deposits of caliche along joint planes in (C) that are suggestive of fluid flow and infilling. (D) Magnifying scales of caliche occurrences along fracture planes in the rock mass. The second photograph displays the competency of a caliche cement capable of supporting broken cobbles of Bishop Tuff. The third photograph shows the relative size of lithic sand grains (0.5-5 mm) bound in the calcareous caliche cement.

Figure 3.10. A panorama showing a portion of the largest single fault surface (~ 235 m) discovered during fieldwork. This surface appears to have formed from shear in non-lightly welded tuff (Ig2Ea). Note the down-dip kinematics preserved in the white caliche deposits on the fault surface.

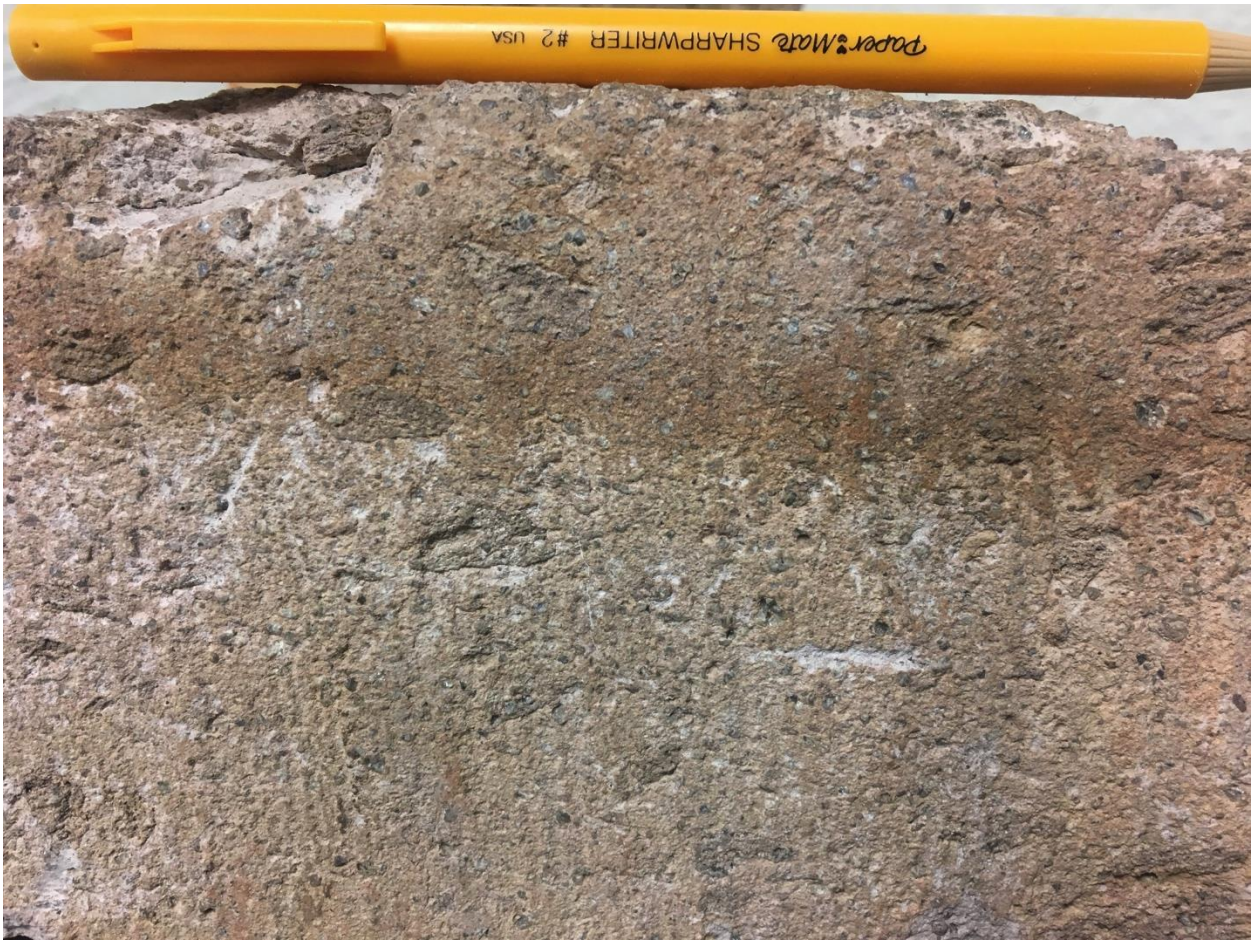

Figure 3.11. A pre-rupture soil profile preserved on a fault surface exhibiting groove lineations (mechanical pencil for scale).

Figure 3.12. Fault surfaces and variable kinematics discovered on the Volcanic Tableland. (A) Dip-slip slickenlines. (B) Oblique-slip grooves, orientation indicated by scale-bar arrow. (C) Near-horizontal strike-slip slickenlines, orientation indicated by scale-bar arrow. (D) Structural overprinting of horizontal slickenlines (indicated by arrow) atop vertical slickenlines in laminar caliche. (E) Horizontal chatter-marks (transport direction aligned with the arrow) that step down to the right indicating left-lateral faulting.

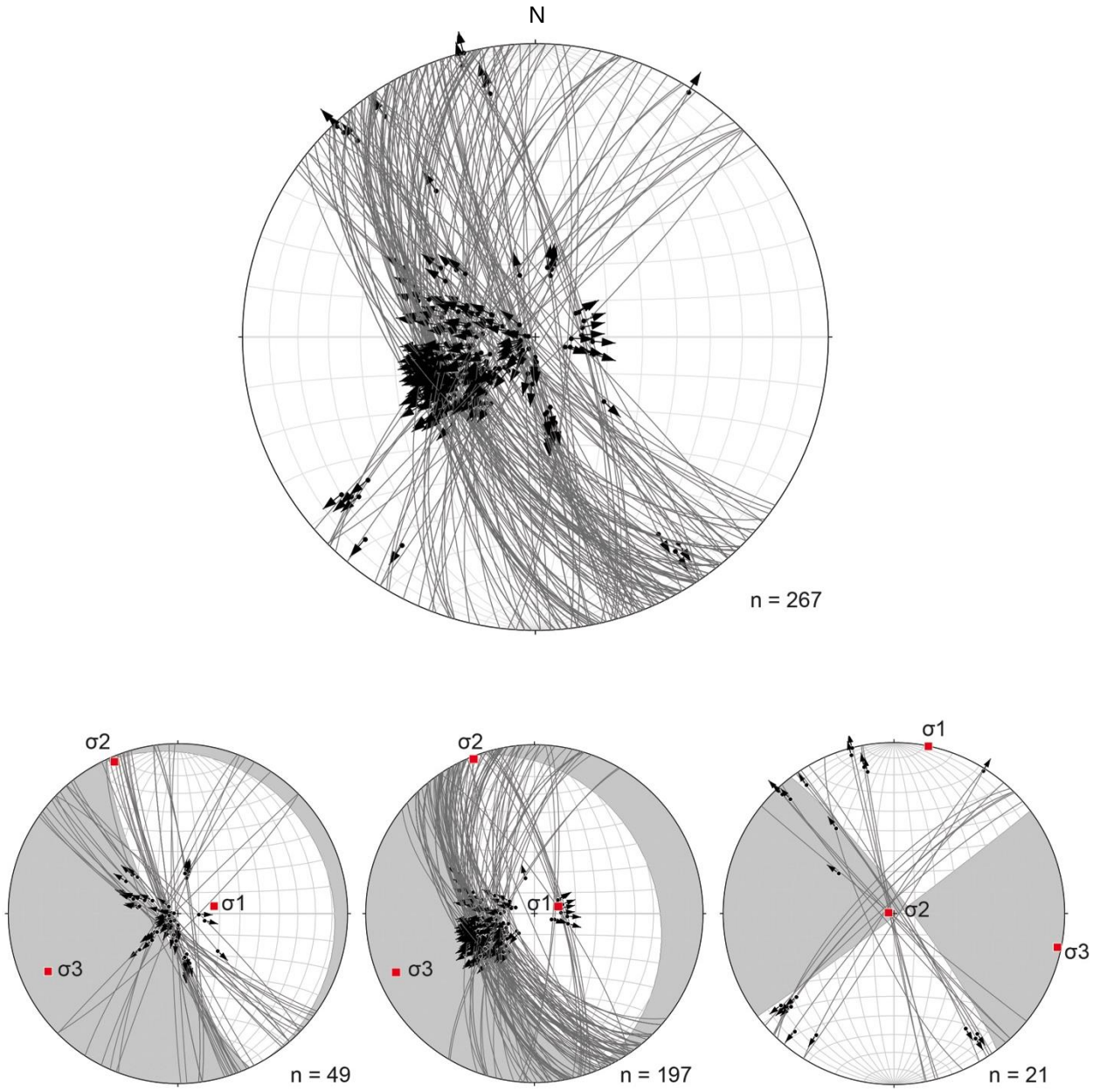

Figure 3.13. Stereonet plotting the 267 fault surface and slickenline pairs. Points and arrows along planes represent the orientation and slip direction of the recorded kinematic indicator. Using a simplified Zoback criteria (Zoback, 1992; Boore et al., 2013), faults classified by the plunge of their kinematic axes (P and T) were used to produce composite fault plane solutions: oblique (left), normal (center), and strike-slip (right). Strike-slip lineations fall near the margin of the plot and trend almost parallel to strike; whereas, steeply-plunging normal and oblique lineations occur centrally and trend oblique-perpendicular from fault strike. The respective principal stress orientations from stress inversion are shown. Note that the strike-slip maximum principal stress is horizontal and bisects the conjugate fault planes, while the maximum principal stress for the normal and oblique datasets is vertical. The minimum principal stress for all populations' trends ~ E-W.

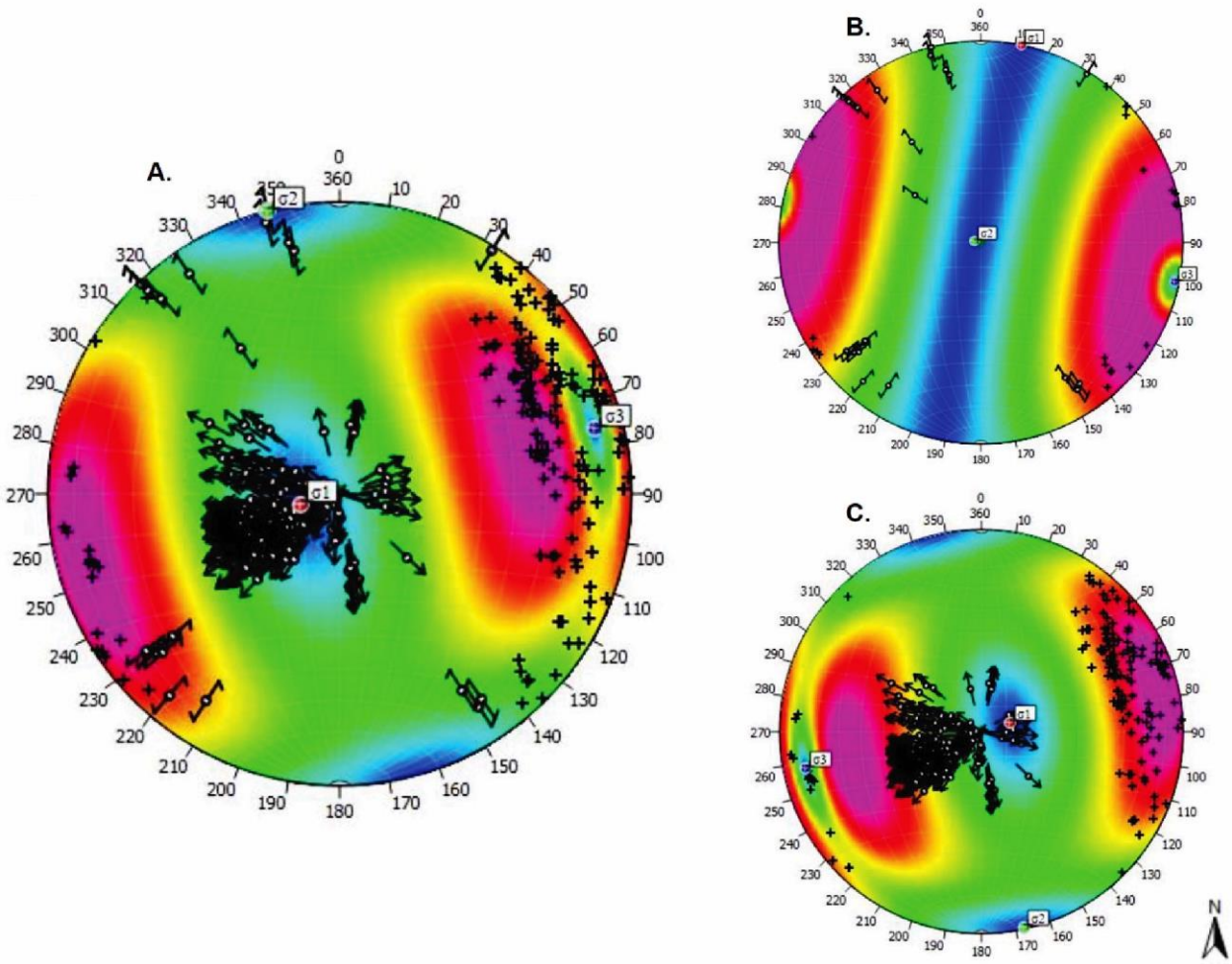

Figure 3.14. Three plotted stress inversions of field kinematic data per Angelier (1990). Fault poles (black cross symbols) have been plotted in lieu of planes, and slickenlines (arrows: strike-slip = bidirectional, and normal-oblique = unidirectional) have been plotted to display trend, plunge, and fault slip direction. Color gradations represent relative slip tendency (high = reds and yellows, low = blues and greens) for fault poles to indicate the likelihood of slip given the inverted principal stress orientations (color gradation correlates with slip tendency values of 0.0-1.0). (A) Stress inversion of all kinematic data collected in the field (n = 267; σ_1 = trend 255°, plunge 79°). (B) Stress inversion of strike-slip faults recorded in the field (n = 21; σ_1 = trend 12°, plunge 0°). (C) Stress Inversion of steeply plunging normal and oblique faults recorded in the field (n = 246; σ_1 = trend 72°, plunge 78°).

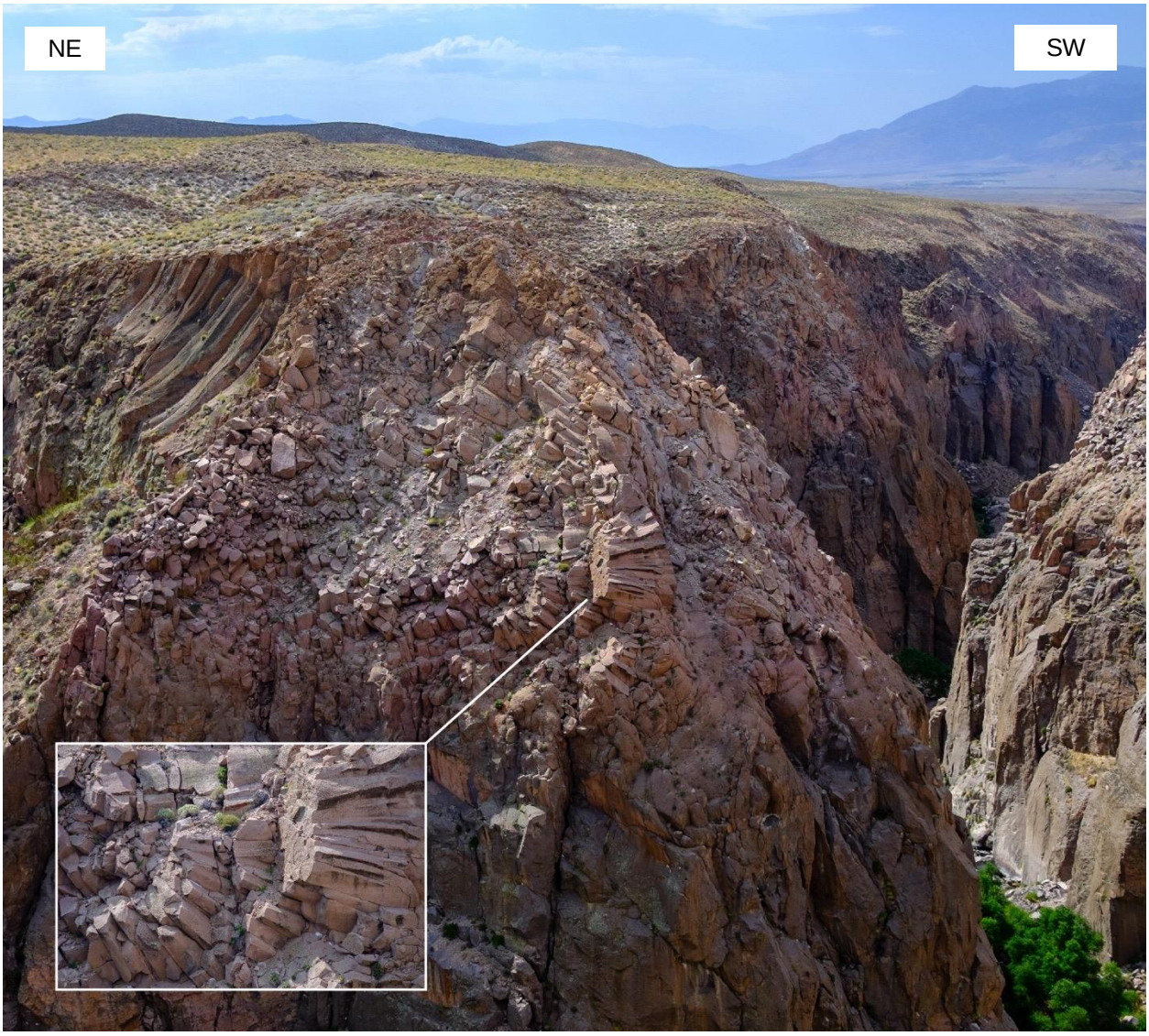

Figure 3.15. Horizontal to vertical columnar joints exposed in Owens River Gorge. Sheridan (1970) suggested that their orientations indicate the patterns of heat flow associated with vapor-phase and fumarolic activity, whereby columns are oriented perpendicular to isothermal gradients. Thus, horizontal columns indicate lateral heat flow and changes in isothermal gradients.

Figure 3.16. Vertically continuous fumarolic pathway (joint) extending ~ 40 m upwards from the base of Owens River Gorge. Columnar joints are expressed in the vapor-phase altered Ig2Ea tuff that overlies densely welded and devitrified Ig1E. Note how columnar joints radiate outwards from the fumarolic pathway indicating that the joint represented a locus of higher heat flow. Also note how these features are observed beneath fumarolic mounds.

Figure 3.17. Secondary mineralization along columnar joints (caliche-left, and quartz-right). It is likely that fine-grained secondary quartz growths accompanied vapor-phase alteration and fumarolic activity.

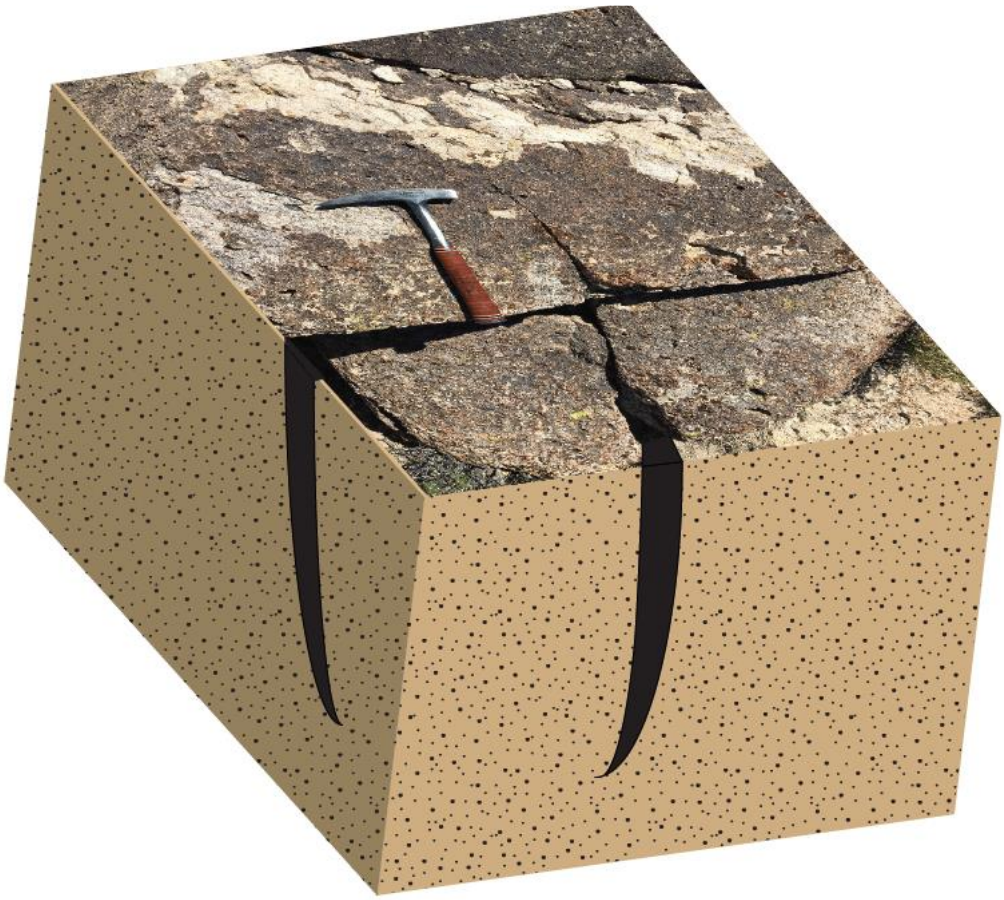

Figure 3.18. Conceptual block model of a cooling joint (~ 1 m scale). It should be noted that the continuity of these features appears to be a function of the degree of welding (more welding = more vertical continuity and vice versa).

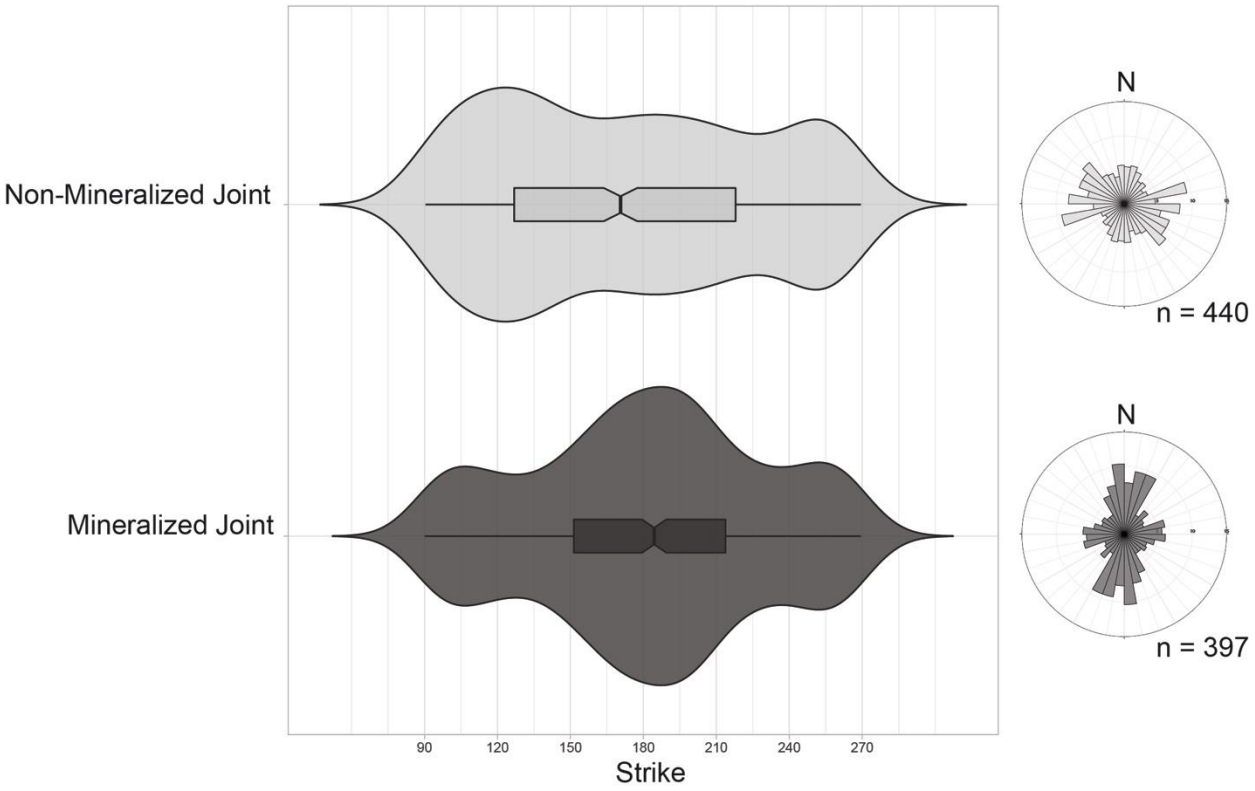

Figure 3.19. The strike azimuths of mineralized and non-mineralized joints recorded in the field. Left: Violin plots showing probability density functions of the strike for each dataset. Peaks on a violin plot indicate the relative probability of observing a value (joint strike) given the distribution of the recorded data. The box plot inside each violin plot shows statistical data (whiskers = minimum and maximum; vertical bar = median; and boxes = interquartile range/middle 50%). Thus mineralized joints appear to have greater probabilities of having NE-NW, and some E-W orientations. Conversely, non-mineralized joints appear to be more random and have approximately equal probabilities of having any strike azimuth. Right: Rose plots showing the frequency distribution of joint strikes for each data set in 10^{o} bins. Note the preferred NE-NW azimuths of mineralized joints.

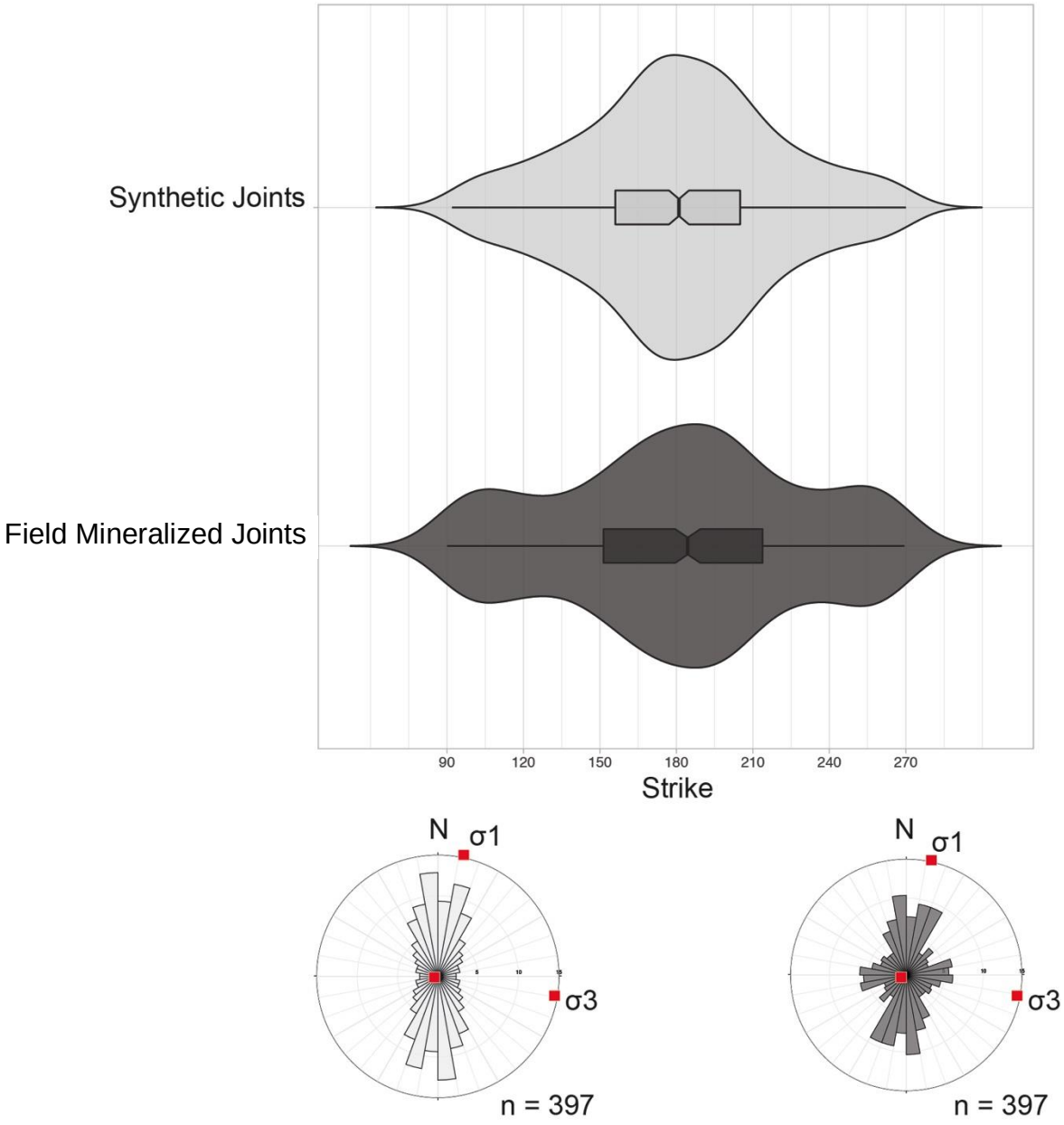

Figure 3.20. A comparison of the orientations of modeled fumarolic pathways (synthetic joints) and observed mineralized joints from the field. Note the similarities in the violin, box, and rose plots of each dataset, indicating greater probabilities of observing NE-NW strike values for both datasets. Principal stress orientations produced from the stress inversion of strike-slip data are plotted on each respective rose plot. In both data sets, the horizontal maximum principal stress bisects the dihedral angle between NE and NW striking modes. Not only does this indicate strain compatibility between strike-slip fault surfaces and the orientation of conjugate joints on the tableland, but it also suggests a similarity between the principal stresses derived from strike-slip fault surfaces in the field and the modeled stresses of the 1986 Chalfant Valley earthquake sequence used to create the synthetic joints.

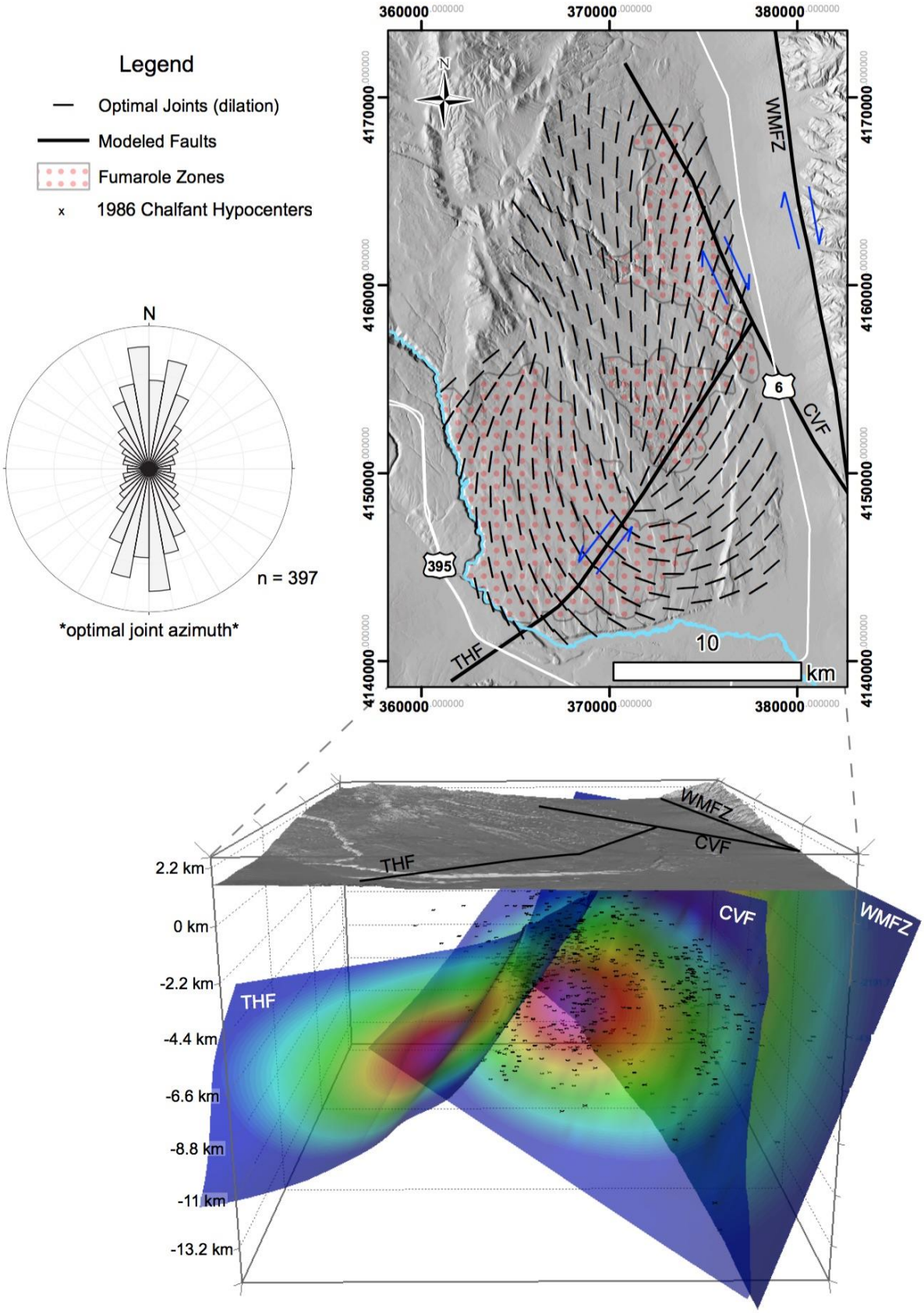
Legend
Optimal Joints (dilation)
Modeled Faults
Fumarole Zones
1986 Chalfant Hypocenters
N
n = 397
optimal joint azimuth
360000
370000
380000
4170000
4160000
4150000
4140000
WMFZ
CVF
THF
6
395
10
km
2.2 km
0 km
-2.2 km
-4.4 km
-6.6 km
-8.8 km
-11 km
-13.2 km

Figure 3.21. (A) Map showing the surface projections of the three fault surfaces created from USGS earthquake data of the 1986 Chalfant Earthquake sequence using MOVE 3D software and regional maps (UTM Zone 11 N). The fault surfaces are abbreviated as follows: Tungsten Hills Fault (THF), Chalfant Valley Fault (CVF), and the White Mountain Fault Zone (WMFZ). The sense of slip along each fault plane is indicated with blue arrows according to the motion described by Smith and Priestly (2000). Slip magnitudes on each fault were modeled according to research and observations published after the 1986 earthquake sequence (Cockerham and Corbett, 1987; Smith and Priestly, 2000). The relative slip along the modeled faults was used to calculate the optimal azimuth of vertical joints at the surface that would become dilated as a result of basement fault motion (see rose plot). (B) Modeled fault ellipses are colored by displacement, with red representing the area of maximum displacement in each fault centroid. Earthquake hypocenters are plotted according to the symbology shown above.

CHAPTER FOUR

DISCUSSION

Faults, Kinematics, and Deformation of the Volcanic Tableland

This study sheds new light on the deformation of the Volcanic Tableland through the discovery and documentation of kinematic evidence present in the Bishop Tuff. Slickenlines and fault grooves record dip-slip (n = 197), oblique-slip (n = 49), and strike-slip (n = 21) motions on the tableland. Therefore, contrary to suggestions in previous research (Dawers et al., 1993; Pinter, 1995; Phillips and Majkowski, 2011; Ferrill et al., 2016), tableland faults are not the sole product of outer-arc extension from downfaulting along the White Mountain Fault Zone. Fault surfaces and kinematic indicators appear to be best preserved in non-welded, vapor-phase, and partly welded units in the north (Ig2Ea and Ig2Ec), supporting previous findings along minor faults in nonwelded units on the southern margin of the tableland (Evans and Bradbury, 2004; Dinwiddie et al., 2006; Ferrill et al., 2016). In these units, minor fault gouge has assisted in the preservation of fault surfaces from erosion, and secondary mineralization in the form of caliche indicates that meteoric fluid flow took place along faults. In moderate to densely welded outcrops atop the southern half of the tableland (Ig2Eb), kinematic indicators are preserved as grooves and chatter marks except where caliche has permitted the development of slickenlines. Similarly, the development of caliche along these fault surfaces indicates the occurrence of post-emplacement, preferential meteoric fluid flow along structures.

Only about 8% of the fault surfaces recorded in this study may be categorized as being strike-slip, and the remaining majority of tableland faults exhibit vertical to subvertical down-dip

motions along normal and oblique faults. Their steeply plunging kinematics suggest ENE and WSW extension that is perpendicular to the NW trend of Owens Valley, and consistent with existing research on the direction of valley extension (Pinter, 1995; Unruh, 2003; Nagorsen-Rinke et al., 2013).

The observed strike-slip faults are kinematically compatible with the conjugate sinistral and dextral strike-slip system that was reactivated during the 1986 Chalfant Valley earthquake sequence (Cockerham and Corbett, 1987; Pacheco and Naebelek, 1988; Smith and Priestly, 2000), and likely predates tuff emplacement. In fact, the strikes of the modeled blind faults and the averages of the observed faults only differ by ~ 3^{o}. These findings indicate that structures at depth are kinematically linked with structures at the surface, and that seismic rupture at depth is capable of being accommodated along surficial structures in the Bishop Tuff. Dawers et al. (1993) and Lienkaemper et al. (1987) both suggested that distributed deformation in valley fill material beneath the tuff played a role in distinguishing faulting on the tableland from basement seismic activity. Dawers et al. (1993) postulated that this distributed deformation accounted for the kinematic differences between strike-slip activity in the basement and normal faulting at the surface, while Lienkaemper et al. (1987) reasons that simple shear at depth is expressed as normal fault-guided slip along existing tableland structures. It is likely that basement faulting is transferred to the surface via some combination of both of these inferences; however, they should be modified in light of the strike-slip and oblique-slip kinematics discovered in this study.

The orientations of strike-slip and oblique-slip faults from field data (vertical dips trending mostly NE and NW) suggest that they operate independently of normal faults and thus represent unique tableland structures. An exception to this would be where structural overprinting was observed along NW-striking faults optimally oriented for both dip-slip and

strike-slip. Therefore, it is apparent that any distributed deformation that might occur beneath the Bishop Tuff does not completely isolate the tableland from basement kinematics. The implications of this are numerous. Tableland faults may be more vertically continuous than previously believed, and/or basement faulting may terminate closer to the surface. Furthermore, valley fill material may have a greater competency to support structures and transfer slip to the surface than previously supposed.

Regarding the continuity of tableland faults, it was previously mentioned that Dawers et al. (1993) provides compelling evidence through the analysis of displacement profile shapes that faults greater than ~ 600 m in length break completely through the Bishop Tuff. Operating under the same assumptions, mapped faults and overlapping segments of lengths exceeding ~ 600 m can be interpreted similarly. Of the 749 faults that were mapped for this study, many exceed this length (n = 152). Additionally, where data resolution allowed for mapping in finer detail, faults were mapped up to a 1:5,000 scale resulting in many short fault segments. These shorter mapped segments frequently overlap and connect to exceed 600 m in length. Dawers and Anders (1995) suggest that the displacement-length scaling relationship for linked faults is the same as single-segment faults on the tableland, thus the actual number of faults that would break through the Bishop Tuff is greater than 152.

Basin-depth maps produced by Saltus and Jachens (1995) yield interpreted valley-fill thicknesses of 2-3 km beneath the Chalfant and Round Valley branches of the Bishop Basin, which respectively underlie the eastern and southern regions of the tableland (Stevens et al., 2013). As this valley fill is composed of extrusive igneous material in addition to fluvial and lacustrine sediments, it is likely that the thickness of material in the basins beneath the tableland is sufficient to induce some degree of mechanical compaction, and perhaps other diagenetic

processes, that would increase the coherence of the material beneath the Bishop Tuff. Conceptually, compacted valley fill material would be more capable of hosting discrete structures and transferring seismic rupture towards the surface.

Normal faults of similar orientations to tableland faults are also present in valley fill material that overlies the tuff in the vicinity of Bishop (Hollett, 1991), and they display little offset. Given the deformation expressed in the Bishop Tuff on the tableland, it is likely that faults present in this younger, unconsolidated valley fill material formed from the influence of preexisting structures in the underlying, more coherent tuff. Similarly, as long isolated and linked tableland faults have been suggested to penetrate through the tuff sheet, it is possible that they may connect with preexisting faults at depth. For example, Fish Slough fault has ~ 145 m of throw (Ferrill et al., 2016) and is believed to represent a fault bounded bedrock block due to a gravity high identified on its eastern footwall (Bateman, 1965; Pakiser et al., 1964; Saltus and Jachens, 1995; Stevens et al., 2013). Furthermore, Bateman (1965) relates the NW and NE curvature of faults to an underlying joint network because of their similarity to regional joints in the mesozoic granitoids of the Sierra Nevada and Tungsten Hills, suggesting that joints in the warped crystalline basement beneath the tableland may have controlled the pattern of faulting.

As it is believed that the present Owens Valley has been opening since the middle to late Pliocene (3.5-2.3 Ma) (Pakiser et al., 1964; Bachman, 1978), the current array of faults along the flanks and center of the Owens Valley graben may offer an indication that preexisting subsurface structures share a similar geometry. However, it is important to note that gravity surveys suggest that the paleo-Owens Valley had more variable topography than at the present (Pakiser et al., 1964; Saltus and Jachens, 1995) thus these subsurface structures might also reflect this variability in terms of their orientations and cross-valley distribution.

When considering this information, the relative displacement of faults (1-145 m) to basin thickness (maximum between 2-3 km), peaked and plateaued displacement profiles reported by Dawers et al. (1993), and the fact that basement strike-slip faults do not breach the surface of the Bishop Tuff all serve to support the nucleation of tableland faults near the free surface of the Owens Valley. Their nucleation was likely the result of heterogeneous faulting along the White Mountain Fault Zone (dextral and normal motions) and a blind conjugate strike-slip system beneath Owens Valley. Small isolated faults (< 600 m length) on the tableland likely nucleated at the free surface of the tuff and are contained completely in the ash-flow sheet as Dawers et al. (1993) suggests. Meanwhile, larger faults (e.g. Fish Slough) have been interpreted to extend to greater depths and possibly join preexisting structures. These faults are often formed from linkage and have curvilinear fault traces. Above the Round Valley and Chalfant branches of the Bishop Basin, large faults that break through the tableland likely terminate in valley fill material at depth, as is evidenced by their displacement relative to the km's of material in the basin. Thus, some degree of distributed deformation through mechanically compacted valley fill material must have contributed to transferring basement rupture to the surface of the tableland, where strike-slip kinematics are preserved amongst numerous normal and oblique faults. However, as gravity surveys indicate that Fish Slough fault bounds a suspended block of pre-cenozoic basement (Pakiser et al., 1964; Saltus and Jachens, 1995), it is feasible that some large displacement faults located above thinner and distal areas of the Bishop Basin might also intersect the basement and/or propagate from preexisting structures.

The variety in kinematics exhibited on the tableland indicates that the regional spreading and opening of northern Owens Valley was the result of complex extension through normal, oblique, and conjugate strike-slip faulting. From an aerial perspective, left-stepping en echelon

arrangements of similarly dipping faults and their mapped distribution (including minor horsetail splays) indicate the presence of a broad, predominantly dextral, transtensional shear zone trending to the northwest (Figure 4.1). Past research supports this finding (Bateman, 1965; Pacheco and Nabelek, 1988; Smith and Priestly, 2000; Nagorsen-Rinke et al., 2013; Delano, 2015). This is particularly noticeable in the Hammil Valley area, which trends parallel to the epicenters of the 1986 Chalfant Valley earthquake sequence. As Dawers (1993) points out, the steep fault dips on the tableland are common of dilational normal faults, but the lack of fissure formation suggests that they exhibit more shear displacement. The combination of flexure and downwarping of the Bishop Tuff along the White Mountain Fault Zone with conjugate strike-slip shear beneath the tableland is likely the cause for these steeply dipping faults that do not exhibit gaping fissures.

The conjugate geometry of blind strike-slip faulting indicates that some degree of wrenching has occurred beneath the tableland, which could account for curved fault strikes, and the discrepancy between kinematics at the surface and in the basement. In a transtensional setting like northern Owens Valley, divergent strike-slip wrenching at depth could form negative flower structures whereby surface fault strands would have predominantly normal displacement, similar to structures found in the Bohai Bay Basin, China (Huang and Liu, 2017). In a study on divergent wrench-fault zones, Harding et al. (1985) characterizes similar structures as “external faults” given their location on the margins of an underlying wrench-fault zone, their steep dips, normal displacement, splay structures, and their arrangement oblique and en echelon to the zone’s trend. This mode of deformation is also coincident with the opposing east and west dipping fault arrays on the tableland, their left-stepping (right-lateral) en echelon patterns, and their sinuous fault traces that curve to become roughly parallel with the strike of the interpolated

Chalfant Valley Fault and its associated epicenters of the 1986 Chalfant Valley earthquake sequence. Perhaps the development of a similar system explains why Dawers and Anders (1995) cited the lack of lateral offset along a stream channel as evidence that strike-slip motion is insignificant on the tableland, despite their observations of splays present at fault terminations and cutting relay ramps. Such observations of strike-slip geometry and normal fault displacement are common in divergent wrench-fault zones and, in a region of dextral transtension, would be expressed as left-stepping external faults like those described by Harding et al. (1985).

Furthermore, external faults of divergent wrench-fault zones have been observed to display a range of normal, oblique, and strike-slip slickenlines (Nelson and Krausse, 1981; Harding et al., 1985) that are similar to the kinematics observed on the tableland. This is due to the combination of extension and horizontal shear stresses active in wrench zones. In the field, the kinematic indicators on the tableland are reflective of the variety of faulting in the region. Oblique and strike-slip fault surfaces have vertical dips and appear to share a direct kinematic relationship with strike-slip faulting beneath the Bishop Tuff. Whereas, normal faults have more moderate dips and appear to relate to the flexural downwarping of the tuff along the White Mountain Fault Zone and perhaps transtensional wrenching along the buried strike-slip zone.

Smith (1987) published an eyewitness account of the 1986 Chalfant Valley main shock (M 6.4) and describes joints in the Bishop Tuff jostling independent of one another. This evidence suggests that seismic rupture is capable of being accommodated along joint surfaces in the tuff and might explain why strike-slip kinematics are often observed along vertical fault surfaces that have similar orientations and scale to conjugate joints. Given the lack of observable lateral offsets and the scale of displacement along strike-slip faults compared to normal faults, it is possible that blind strike-slip motions are accommodated along reactivated conjugate joints.

Flodin and Aydin (2004) describe a similar process involving the development of a conjugate strike-slip system through the shearing of preexisting, through-going fractures in sandstone, and the subsequent development and shear of splay fractures. Conjugate fractures in the Bishop Tuff are well documented, but their formation has been the subject of speculation and is explored in more detail later in this thesis (section: Formation of Conjugate Fractures and Fumarolic Pathways).

Lastly, it is important to note that modeled faults (Chalfant Valley Fault and Tungsten Hills Fault) were constructed using hypocenters from only one earthquake sequence, and that more faults with similar geometry may exist in the basement beneath the tableland and northern Owens Valley. For example, in their study on seismicity in the region spanning between Long Valley and the eastern slope of the White Mountains, dePolo et al. (1993) identified 18 faults capable of producing M 6.8-7.4 earthquakes, including a NE-striking sinistral plane that ruptured beneath the tableland during the 1984 Round Valley earthquake sequence.

Regional Stress of Northern Owens Valley

The paleostress regime of northern Owens Valley has been a subject of much interest given its location at the junction of the Basin and Range province, the Walker Lane belt, the Sierra Nevada, and the Long Valley caldera. Pacheco (1988) cites the prevalent strike-slip seismic activity that has occurred in the region since 1872 as evidence that there has been a recent and distinct rearrangement from a vertical to horizontal maximum principal stress axis, while the horizontal minimum stress axis has remained at approximately the same orientation. However, seeing as how most of the strike-slip surfaces discovered in the field occur on the footwall near the upper free-face of exposed fault scarps (~ 40 m high), it does not seem likely

that there has only been one distinct and recent transition from normal to strike-slip faulting since the tuff's emplacement. Likewise, most of the fresh fault surfaces that were discovered displayed dip-slip kinematics and preserved soil profiles that indicate recent rupture events. Thus, it is apparent that all three modes of faulting have been active since the tuff was emplaced, and their variability may represent temporal changes in the kinematics associated with tableland deformation. For instance, the discovery of structural overprinting in the field offers further evidence that some tableland faults operate in a multimodal manner, allowing them to accommodate the region's heterogeneous deformation through time.

These findings support the claim from Zoback and Zoback (1989) that suggests the contrasting modes of faults (normal, oblique, and strike-slip) in the region are the product of recurring temporal fluctuations in the magnitude of the maximum horizontal stress on the order of tens of thousands of years. Such fluctuations offer an explanation for the variety of kinematics expressed on the tableland, the structural overprinting observed in the field, and the complex fault geometry of the northern Owens Valley.

Through analyzing kinematic data from the field via stress inversion, the corresponding orientation of axes of principal stresses for the entire fault population were calculated. Although the result is concurrent with the overall orientation of faults in the field, the unequal sample sizes of the observed fault surfaces would likely lead to the misinterpretation of principal stress orientations. As regional stress inversions assume the temporal and spatial uniformity of stress (Gephart, 1990), the kinematic data was further subdivided into two populations based on their relative fault motions in order to prevent the obstruction of strike-slip data from the data of more numerous oblique and normal faults. Inverted kinematic data from normal and oblique faults yields a subvertical (78^o) maximum principal stress (σ_1) that trends 72^o and corresponds with

predominantly dip-slip, and some steeply plunging oblique-slip motions. The least principal stress (σ_3) plunges shallowly (< 12°) trending 258°, coincides with the minimum horizontal stress, and is concurrent with ENE-WSW extension. Inverted kinematic data for strike-slip faults, however, suggests an entirely different paleostress and tectonic regime. The inversion of strike-slip data reveals a horizontal maximum principal stress (σ_1) trending 12°, and a horizontal minimum principal stress (σ_3) trending 102°. The maximum horizontal stress bisects the 67° angle between the modeled Chalfant Valley Fault and Tungsten Hills Fault. Meanwhile, the minimum horizontal stress is coincident with ESE-WNW extension.

Despite the differences in orientation of the principal stress axes, both populations (normal and oblique population; strike-slip population) coincide with overall E-W extension in the region and the development of NE-NW striking opening-mode structures oriented perpendicular to the minimum horizontal stress of each population. Similarly, the maximum horizontal stress of both populations is north-striking (σ_2 –normal and oblique population; σ_1 – strike-slip population), which supports records from the central Sierra Nevada block (hydrofracture measurements, and conjugate strike-slip faults) and the eastern Sierra Front (normal and strike-slip faults) detailed by Zoback and Zoback (1989).

Recognizing that the variable kinematics observed in the field and the stress tensors produced via stress inversion are both coincident with past studies on regional deformation (Pacheco, 1988; Zoback and Zoback, 1989), our evidence indicates that the Bishop Tuff has recorded the temporal rotations of the maximum principal stress (σ_1 – from vertical to horizontal) through motion distributed across a blind transtensional strike-slip zone and the White Mountain Fault Zone since its emplacement. Maximum principal stresses with vertical orientations would be accommodated along normal and oblique faults atop the tableland and valley-down normal

faulting on the White Mountain Fault Zone. Maximum principal stresses with horizontal orientations, however, would be accommodated along strike-slip fault surfaces on the tableland, the blind conjugate strike-slip system beneath the tableland, and dextral slip on the White Mountain Fault Zone (e.g. dextral slip during the 1986 Chalfant Valley earthquake sequence). Furthermore, the influence of a horizontal maximum principal stress on normal and oblique faults on the tableland cannot be ruled out if they are indeed affected by wrenching in the subsurface. The preservation of soil profiles along fresh dip-slip fault surfaces despite the recent history of strike-slip seismic activity lends credence to this hypothesis. Therefore, the kinematics expressed during the 1986 Chalfant Valley earthquake sequence represent one type of the current and past tectonism evident in northern Owens Valley, and such variability in stresses should be considered when describing regional and local structures and the hydrothermal activity that is associated with them.

Formation of Conjugate Fractures and Fumarolic Pathways

Conjugate fractures in the Bishop Tuff are evident across the Volcanic Tableland. These features are suggested to have formed from shear (Bateman, 1965; Sheridan, 1970), although the mechanisms for their formation have not been explored in great detail. Sheridan (1970) attributes the formation of these fractures to compaction brought on by the downward stretching and cooling of the tuff atop a buried basin and suggests that the conjugate dihedral angle between fractures can be bisected by the radius of the underlying basin. If this were the case, we would expect to see that the maximum principal stress to be oriented parallel to the bisector between the dihedral angle of conjugate fracture planes, and that the conjugate planes would be oriented radially about the basin with some fracture sets approaching east-west trends (Muehlberger,

1961, Borradaile, 2015). Although basin depth maps indicate that the tuff was deposited in two preexisting basins beneath the tableland (Saltus and Jachens, 1995), when mapped with high-resolution remotely sensed data conjugate fractures exhibit a dominant NE-NW trend regardless of their position in relation to the basin radial. Likewise if basin compaction and cooling of the tuff were the primary factors in forming conjugate fractures, we might expect to see concentrically oriented extensional features (e.g. opening-mode fractures) about the buried basin. Conversely, Bateman (1965) suggests that the fractures represent conjugate shear planes formed from a regional horizontal principal stress, similar to the conjugate structures observed in the nearby Sierra Nevada and Tungsten Hills.

In light of the principal stress orientations produced from the stress inversion of strike-slip field data (σ_1 - horizontal trending 12°, σ_2 – vertical, σ_3 – horizontal trending 102°), the research presented in this thesis supports the mechanism proposed by Bateman (1965). The maximum horizontal stress ($\sigma_1 = \sigma_H$), bisects the acute dihedral angle (~ 60°) between mineralized conjugate fractures and conjugate strike-slip faults recorded in the field (Figures 3.12 and 3.19). This suggests that a N−S horizontally oriented maximum principal stress component is kinematically compatible with conjugate fracture orientations, conjugate strike-slip faults, and even the blind conjugate strike-slip zones at depth. Geothermal research in the Upper Rhine Graben had similar findings where induced seismicity yielded conjugate shear planes that were bisected by the maximum horizontal stress of the regional NW strike-slip stress field (Mukuhira et al., 2011). Provided the similarities in the orientations of these conjugate structures and the horizontally bisecting maximum principal stress derived from inverted strike-slip field data, it is evident that regional stresses were a driving force in the formation of the conjugate fractures. Furthermore, the orientation of the minimum horizontal stress (σ_3) for all faults

observed in the field supports E-W extension and the development of NE to NW striking opening-mode joints between azimuths of 348° and 12°. This extension may account for some of the mineralized structures that appear to bisect the dihedral angle of conjugate fractures.

If the conjugate fractures were some of the first discontinuities to develop after welding in the Bishop Tuff, as has been suggested (Bateman, 1965; Sheridan, 1970; Holt and Taylor, 1998), then they may represent precursors to fault development on the tableland. Their similarities to the orientations of strike-slip surfaces, their vertical continuity, and the fact that many faults appear to have preferentially propagated along the strike of conjugate fractures (dihedral intersections) support our finding. Furthermore, this has implications for the paleostress regime around the time that the Bishop Tuff was emplaced. If conjugate fractures developed early in the tuff from a ~ N-S oriented horizontal maximum principal stress, then it is apparent that the strike-slip activity manifested during the 1986 Chalfant Valley earthquake sequence is representative of the region's tectonic regime at the time of the tuff's emplacement.

Findings on the orientations and mineralization of conjugate joint planes and their functionality as fumarolic pathways on the tableland is described in this thesis and in past research efforts (Bateman, 1965; Sheridan, 1970; Holt and Taylor, 1998). Field observations indicate that fumarolic activity also occurred along polygonal cooling cracks in areas immediately adjoining fumarolic features, and early cooling joints to form curvilinear ridges on the distal and shallow margins of buried basins. These structures likely account for some of the variability evident on the roseplot of mineralized joints (Figure 3.18).

The existing work on the fumarolic activity of the tableland and other large ignimbrite sheets suggests that fumarolic gases (and/or vapors) and latent heat are derived mostly (if not entirely) from the welding and devitrification of the cooling ash-flow sheet (Sheridan, 1970;

Keith, 1991; Holt and Taylor, 1998; Holt and Taylor, 2001; Vaniman, 2006). Therefore, the mapped distributions of the three fumarolic zones of the tableland correspond to the degree of welding and devitrification in the Bishop Tuff (Sheridan, 1970; Wilson and Hildreth, 1997).

However, given the location of the tableland on the flanks of the Long Valley Caldera, volcanism in the Owens Valley proper as recent as 17 ka (Vazquez and Woolford, 2015), and hydrothermal activity on the valley floor along deep valley-bounding faults (Fish Slough Fault thermal springs, Keough's Hot Springs, and Benton Hot Springs), there is reasonable potential for an additional source of hydrothermal fluids to have supported fumarolic activity. There are currently three active thermal springs emerging from NE-striking fault tips on the Fish Slough Fault in an area with extensive vapor-phase alteration and fumarolic features. Jaykoh and Fatooh (2010) note that these springs are likely rooted to a deeper hydrothermal system, and that the area's water table rose as a result of the 1986 Chalfant Valley earthquake sequence. The duration of this rising water table peaked approximately one year after seismic activity and tapered to preexisting levels approximately six years later (Jaykoh and Fatooh, 2010), indicating that it is a structurally enhanced system (conversely, short term rises following seismic activity are typically related to compaction and reduced permeability). As Fish Slough Fault has been interpreted to root into the pre-cenozoic basement (Bateman, 1965; Pakiser et al., 1964; Saltus and Jachens, 1995; Stevens et al., 2013), it appears to tap into a deep hydrothermal system located beneath the Bishop Basin.

Furthermore, the influence of meteoric water (e.g. lakes, rivers, and precipitation) present at the time of (and following) emplacement cannot be ruled out. Holt and Taylor (1998) suggest that the hydrothermal circulation of meteoric water through the cooling tuff would serve as an

additional source for fumarolic vapors, while simultaneously accounting for the lack of deeper hydrothermal signatures (e.g. magmatic ^{18}O values) observed in the fumarolically altered tuff.

Despite these potential secondary sources, minerals and/or alteration indicative of a deeper hydrothermal system have not been identified in the preliminary petrographic or XRF analysis of fumarolic samples. In fact, these analyses yields that microcrystalline quartz (perhaps cristobalite) and minor amounts of K-feldspar are essentially the only minerals associated with fumarolic alteration. Thus, it is likely that the elemental constituents of these minerals were transported in fumarolic vapors and condensate that were formed from the devitrification of the underlying welded tuff (Ig1E) and probable influx of supplementary meteoric water.

Nevertheless, the shallowing water table and increased outflow of thermal springs following the 1986 Chalfant Valley earthquake sequence (Brewer, 1989; Jaykoh and Fatooh, 2010) is evidence for the vertical migration of subsurface fluids along structures (faults and fractures) that were seismically enhanced by strike-slip tectonics. As this earthquake sequence has been determined to be representative of the region's tectonics at the time of tuff emplacement, the seismic enhancement of these structures is analogous to the past dilation of fumarolic pathways. Therefore, the subject of the apparent interaction between deep hydrothermal and shallow meteoric fluids in Fish Slough remains of interest given its relation to the region's structural deformation.

The model results presented in this thesis that were derived from the recreated stress field of the 1986 Chalfant Valley earthquake sequence indicate that joints of similar orientations to mineralized joints recorded in the field are enhanced through dilation by strike-slip faulting at depth, allowing them to behave as optimal pathways for fumarolic activity. A suitable analog for these features is located in Turkey, where travertine ridges have formed from the progressive

dilation of fissures in a structural region characterized by cyclical normal to transtensional kinematics (Brogi et al., 2014). Thus, fumarolic features represent a manifestation of the strike-slip tectonic regime that was contemporaneous with the emplacement of the Bishop Tuff and a driving force in the development of early conjugate fractures and their subsequent enhancement as fumarolic pathways.

The relative timing of these features can be inferred from the field observations, modeling efforts, and petrographic analysis described in this thesis. (1) Progressive welding in the lower emplacement units of the Bishop Tuff (Ig1E) led to the devitrification of volcanic glass and subsequent production of silicate mineral phases (predominantly quartz/cristobalite) and volatiles. Varied degrees of welding in the upper emplacement unit (Ig2Eb) exhibited a confining geometry on produced volatiles, forming a zone of vapor-phase alteration. (2) As the structural competency of the tuff increased due to welding, vertical NE-NW striking conjugate fractures formed as a result of a regional horizontal maximum principal stress that was oriented ~ N-S (bisecting the dihedral angle of the conjugate set). This horizontal maximum principal stress was responsible for regional strike-slip activity. (3) Strike-slip tectonics similar to those exhibited during the 1986 Chalfant Valley earthquake sequence dilated conjugate fractures and fault planes, enhancing them to transmit volatiles and vapor-phase activity to the surface of the Volcanic Tableland, resulting in extensive fumarolic activity. The relative heat flow associated with subsurface vapor-phase activity formed columnar joints at perpendicular angles to isothermal gradients, and their orientations indicate higher heat flow along vertical conjugate fractures. Conjugate fracture surfaces and non-welded tuff at the surface of the tableland became mineralized from this fumarolic activity, forming an indurated silicified rind (~ 10mm thick) along surfaces that came into contact with rising fumarolic vapors and associated condensation.

(4) Subsequent erosion of the non-welded and non-mineralized tuff at the surface of the tableland produced a landscape of relict fumarolic mounds and ridges.

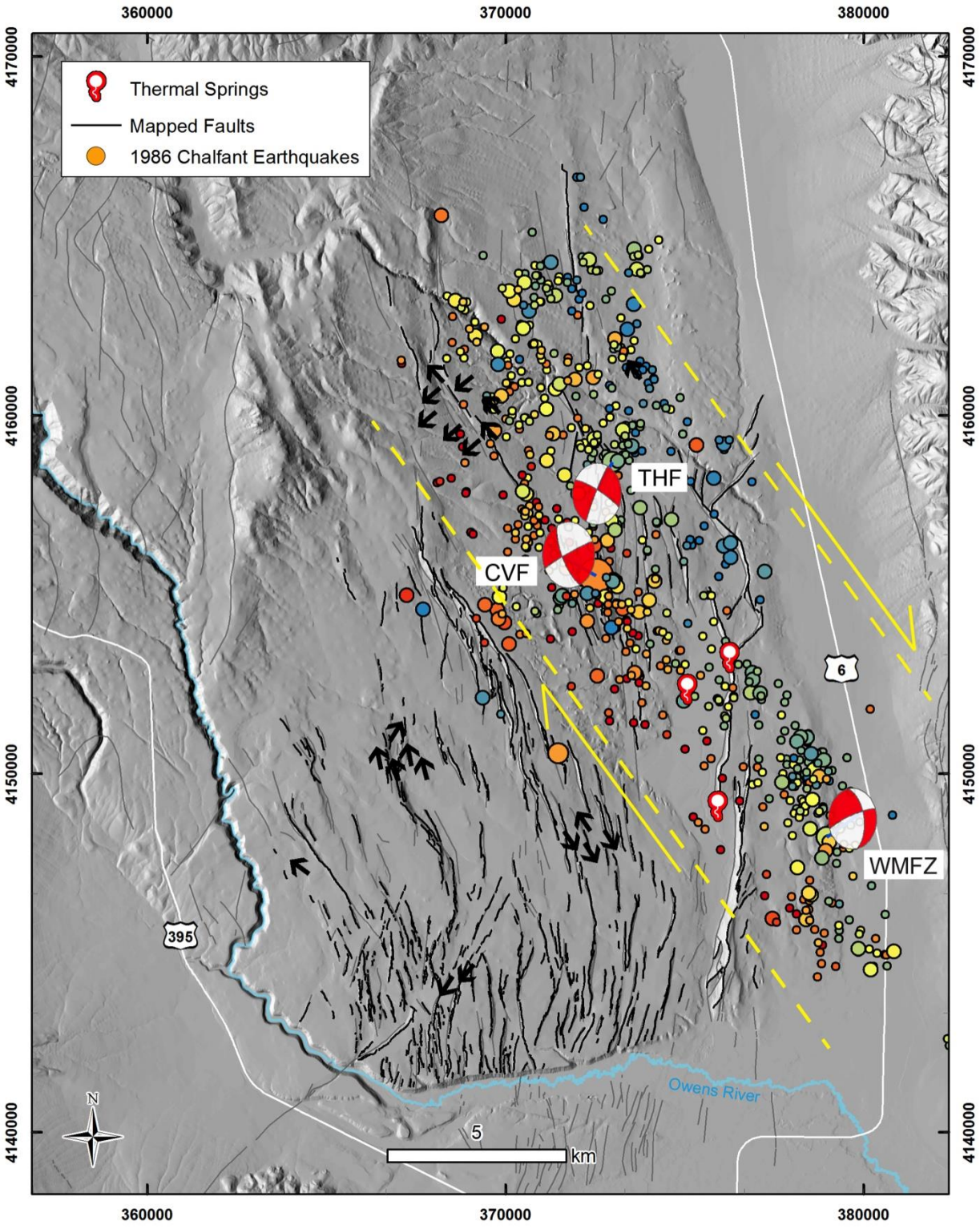
360000
370000
380000
4170000
4160000
4150000
4140000
Thermal Springs
Mapped Faults
1986 Chalfant Earthquakes
THF
CVF
WMFZ
6
395
Owens River
N
5
km

Figure 4.1. Map of the approximate boundary of the strike-slip zone (dashed yellow lines) beneath the Volcanic Tableland (UTM Zone 11N). Colored points represent 624 hypocenters from the 1986 Chalfant Valley earthquake sequence (> M 2.5), and they are colored according to depth (blue/green = shallow (~ 2 km), red = deep (~ 11 km)) and sized by magnitude (larger symbols correlate with greater magnitude events). The focal mechanisms of the three largest events (Chalfant Valley Fault (CVF) – M 6.3; Tungsten Hills Fault (THF) – M 5.7; White Mountain Fault Zone (WMFZ) – M 5.5) are included (P quadrants = white, T quadrants = red). Small black arrows indicate the slip directions recorded on strike-slip fault surfaces in the field (NW and SE = Dextral, NE and SW = Sinistral). The locations of these arrows have been slightly dispersed to allow for visual interpretation, for their precise geographic locations refer to Table 1. Overall motion of the zone is identified as being right-lateral, which is compatible with the left-stepping en echelon map pattern of identified tableland faults (bold lines = mapped for this study, pale lines = USGS quaternary faults database). Also note the three thermal springs identified on the tableland fall within this zone, and that several faults in their vicinity exhibit releasing geometries.

CHAPTER 5

CONCLUSIONS

Through high-resolution mapping, three-dimensional modeling, and the documentation of new kinematic evidence of faulting in the Bishop Tuff, this research sheds new light on the deformation of the Volcanic Tableland north of Bishop, CA, and its relationship to the tectonics of Northern Owens Valley and the Eastern California Shear Zone. Dip-slip, oblique-slip, and strike-slip kinematic indicators (grooves, slickenlines, and chatter marks) are all indicative of transtensional regional tectonics that have been active, at a minimum, since the tuff's emplacement ~ 760 ka. The left-stepping en echelon arrangement of faults, variable kinematics identified in the tuff, and conjugate strike-slip faulting identified during the 1986 Chalfant Valley earthquake sequence all serve as indicators that the tableland overlies a divergent wrench zone that accommodates regional motions of the White Mountain Fault Zone and the northwestern translation of the Sierra Nevada microplate. These varied kinematics, observations of structural overprinting, and the orientations of principal stresses derived from stress inversion are compatible with regional E-W extension (perpendicular to the trend of Owens Valley) and temporal fluctuations of the maximum principal stress between vertical and horizontal orientations that account for the varied strike-slip and dip-slip (oblique and normal) motions preserved in the rock record. Through analyzing the relationship and orientation of sites of fumarolic activity to conjugate NE-NW striking structures in the tuff, it is possible to recognize their potential significance as indicators of a paleostress regime. Conjugate fumarolic pathways are strain compatible with the horizontal principal stress orientations of observed strike-slip faults, and similar conjugate fracture planes have been identified in the surrounding region

(Sierra Nevada and Tungsten Hills). Therefore it is likely that these pathways represent conjugate shear planes formed from a regional horizontal maximum principal stress. Similar results were obtained upon modeling the strike-slip kinematics active during the 1986 Chalfant Valley earthquake sequence in order to produce a synthetic set of enhanced fumarolic pathways (dilated joints). Therefore, the evidence suggests that the current strike-slip tectonic regime manifested during the 1986 Chalfant Valley earthquake sequence was also contemporaneous with the emplacement of the Bishop Tuff. These tectonics were responsible for the early formation of conjugate fractures and their subsequent enhancement to function as fumarolic pathways, thus governing fumarolic activity at the surface of the Volcanic Tableland. These findings provide new insight on the complex modes of deformation present at the intersection of the Basin and Range province, the Walker Lane belt (Eastern California Shear Zone), the Sierra Nevada microplate, and the Long Valley caldera, and they should be taken into consideration during future research efforts in the region.

REFERENCES

Allmendinger, R.W., Gephart, J.W., and Marrett, R.A., 1989, Notes on Fault Slip Analysis: Geological Society of America Short Course "Quantitative Interpretation of Joints and Faults", November 4 & 5 1989, p. 23-26.

Allmendinger, R.W., 2017, FaultKin Software (Version 7.7.4), Available from: http://www.geo.cornell.edu/geology/faculty/RWA/programs/faultkin.html

Anderson, E. M.,1951, The Dynamics of Faulting: Oliver and Boyd, Edinburgh, 206 pp.

Bachman, S.B., 1978, Pliocene-Pleistocene break-up of the Sierra Nevada-White-Inyo Mountains block and formation of Owens Valley: Geology, v.6, p. 461-463, doi:10.1130/0091-7613(1978)6<461:PBOTSN>2.0.CO;2.

Bailey, R.A., Dalrymple, G.B., and Lanphere, M.A., 1976, Volcanism, Structure, and Geochronology of Long Valley Caldera, Mono County, California: Journal of Geophysical Research, v. 81, no. 5, p. 725-744.

Bateman, P.C., 1965, Geology and tungsten mineralization of the Bishop district, California: U.S. Geological Survey Professional Paper 470, p. 208

Boore, D.M., Stewart, J.P., Seyhan, E., and Atkinson, G.M., 2013, NGA-West 2 Equations for predicting response spectral accelerations for shallow crustal earthquakes: *PEER Rpt. 2013/05*, Pacific Earthquake Engineering Research Center, Berkeley, California, p. 1106.

Borradaile, G., 2015, Chapter 9 – Faults: Understanding Geology Through Maps: Elsevier, p. 111-139.

Brewer, L., 1989, The Intensity of the July 21, 1986, Chalfant Valley, California, Earthquake: U.S. Geological Survey Open-File Report 89-135, p. 1-25.

Brogi, A., Capezzuoli, E., Alçiçek, M.C., and Gandin, A., 2014, Evolution of a fault-controlled fissure-ridge type travertine deposit in the western Anatolia extensional province – the Çukurbağ fissure-ridge (Pamukkale, Turkey): Journal of the Geological Society – London, v. 171, p. 425-441.

Cockerham, R. S. and Corbett, E. J., 1987, The July 1986 Chalfant Valley, California, Earthquake Sequence, Preliminary Results: Seismological Society of America Bulletin, v. 77, no. 1, p. 280-289.

Comninou, M and Dundurs, J., 1975, The angular dislocation in a half space; Journal of Elasticity 5 (3-4), p. 203-216.

Dawers, N.H., Anders, M.H., and Scholz, C.H., 1993, Growth of normal faults: Displacement-length scaling: Geology, v. 21, p. 1107–1110.

Dawers, N.H., and Anders, M.H., 1995, Displacement-length scaling and fault linkage: Journal of Structural Geology, v. 17, p. 607-614.

Dawers, N.H., Sheehan, T.P., and Kirby, E., 2002, Structural nature of a large discontinuity in the Sierra Nevada extensional fault system:The Coyote "Warp" of northern Owens Valley, California: Geological Society of America Abstracts with Programs, v. 34, no. 6, p. 248.

Delano, K.M., 2015, Geologic Mapping in the Black Mountain Area, Northern Eastern California Shear Zone: Testing a Kinematic and Geometric Fault Slip Transfer Model: (Unpublished Master's Thesis), Central Washington University, Ellensburg, Wa.

dePolo, C.M., Peppin, W.A., Johnson, P.A., 1993, Contemporary tectonics, seismicity, and potential earthquake sources in the White Mountains seismic gap, west-central Nevada and east-central California, USA: Tectonophysics, v. 225, p. 271-299.

de Silva, S.L., and Bailey, J.E., 2017, Some unique surface patterns on ignimbrites on Earth: A "bird's eye" view as a guide for planetary mappers: Journal of Volcanology and Geothermal Research, v. 342, p. 47-60.

Dinwiddie, C.L., Bradbury, K.K., McGinnis, R.N., Fedors, R.W., and Ferrill, D.A., 2006, Fault zone deformation overprints permeability of non-welded ignimbrite: Chalk Cove fault, Bishop Tuff, Bishop, California: Vadose Zone Journal, v.5, p. 610-627, doi:10.2136/vzj2005.0062.

Dixon, T.H., Miller, M., Farina, F., Wang, H., and Johnson, D., 2000, Present-day motion of the Sierra Nevada block and some tectonic implications for the Basin and Range province, North American Cordillera: Tectonics, v. 19, p. 1–24.

Evans, J.P., and Bradbury, K.K., 2004, Faulting and fracturing of non-welded Bishop Tuff, eastern California: Deformation mechanisms in very porous materials in the vadose zone: Vadose Zone Journal, v. 3, p. 602–623.

Ferrill, D.A., Morris, A.P., McGinnis, R.N., 2012, Extensional fault-propagation folding in mechanically layered rocks: The case against the frictional drag mechanism: Tectonophysics, v.576-577, p. 78-85.

Ferrill, D.A., Morris, A.P., McGinnis, R.N., Smart, K.J., Watson-Morris, M.J., Wigginton, S.S., 2016, Observations on normal-fault scarp morphology and fault system evolution of the Bishop Tuff in the Volcanic Tableland, Owens Valley, California, U.S.A.: Lithosphere, v. 8, p. 238-254., doi:10.1130/L476.1.

Flodin, E.A., and Aydin, A., 2004, Evolution of a strike-slip fault network, Valley of Fire State Park, southern Nevada: Geological Society of America Bulletin, v. 116, p. 42-59, doi: 10.1130/B25282.1.

Gephart, J.W., 1990, Stress and the direction of slip on fault planes: Tectonics, v.9, p.845-858.

Gilbert, C.M.,1938, Welded tuff in eastern California: Geological Society of America Bulletin, v. 49, p. 1829-1862, doi: 10.1130/GSAB-49-1829.

Harding, T.P., Vierbuchen, R.C., and Christie-Blick, N., 1985, Structural styles, plate-tectonic settings, and hydrocarbon traps of divergent (transtensional) wrench faults: Society of Economoic Paleontologists and Mineralogists Special Publication, v.37, p. 51-77.

Hildreth, W., and Fierstein, J., 2017, Geologic Filed-Trip Guide to Long Valley Caldera, California: U.S. Geological Survey Scientific Investigations Report 2017–5022–L, 119 p., https://doi.org/10.3133/sir20175120L.

Hollett, K.J., Danstein, W.R., McCaffrey, W.F., and Walti, C.L., 1991, Chapter B, Geology and Water Resources of Owens Valley, California: U.S. Geological Survey Water Supply Paper 2370, 77 p.

Holt, E.W., and Taylor, H.P., 1998, $^{18}O/^{16}O$ mapping and hydrogeology of a short-lived (~ 10 years) fumarolic ($> 500^{o}C$) meteoric–hydrothermal event in the upper part of the 0.76 Ma Bishop Tuff outflow sheet, California: Journal of Volcanology and Geothermal Research, v.83, p.115-139.

Huang, L., and Liu, C.-y., 2017, Three types of flower structures in a divergent-wrench fault zone: Journal of Geophysical Research: Solid Earth, v. 122, p. 10,478–10,497.

Jaykoh, A.S. and Fatooh, J., 2010, Fish Slough, a Geologic and Hydrologic Summary, Inyo and Mono Counties, California, U.S. Department of the Interior Administrative Report Prepared for BLM Bishop Field Office, p. 1-33.

Keith, T.E.C., 1991, Fossil and active fumaroles in the 1912 eruptive deposits, Valley of Ten Thousand Smokes, Alaska: Journal of Volcanology and Geothermal Research, V. 45, p. 227-254.

Lienkaemper, J.J., Pezzopane, S.K., Clark, M.M., and Rymer, M.J., 1987, Fault fractures formed in association with the 1986 Chalfant Valley, California, earthquake sequence Preliminary Report: Bulletin of the Seismological Society of America, v.77, p. 297-305.

Lipman, P.W., Prostka, H.J., and Christiansen, R.L., 1972, Cenozoic Volcanism and Plate-Tectonic Evolution of the Western United States, Part 1, Early and Middle Cenozoic: Philosophical Transactions of the Royal Society of London, Series A, Mathematical and Physical Sciences, v. 271, no. 1213, A Discussion on Volcanism and the Structure of the Earth, p. 217-248.

Lovely, P.J., 2011, Fault-related deformation over geologic time: Integrating field observations, high resolution geospatial data, and numerical modeling to investigate 3D geometry and non-linear material behavior: (Unpublished Dissertation) Stanford University, Stanford, CA.

Marrett, R., and Allmendinger, R.W., 1990, Kinematic Analysis of Fault-Slip Data: Journal of Structural Geology, v. 12, no. 8, p. 973-986.

Marchand, D.E.,1971, Rates and modes of denudation, White Mountains, eastern California: American Journal of Science, v. 270, p. 109-135.

McGinnis, R.N., Morris, A.P., Ferrill, D.A., and Dinwiddie, C.L., 2009, Deformation analysis of tuffaceous sediments in the Volcanic Tableland near Bishop, California: Lithosphere, v. 1, p. 291–304, doi:10.1130/L43.1.

Muehlberger, W.R., 1961, Conjugate joint sets of small dihedral angle: Journal of Geology, v.69, p. 211-219.

Mukuhira, Y., Hiroshi, A., Niitsuma, H., and Häring, M., 2011, Identification of fracture orientation for large induced seismicity recorded at Basel, Switzerland in 2006: Transactions - Geothermal Resources Council, v. 35, p. 487-491.

Nagorsen-Rinke, S., Lee, J., and Calvert, A., 2013, Pliocene sinistral slip across the Adobe Hills, eastern California–western Nevada: Kinematics of fault slip transfer across the Mina deflection: Geosphere, v. 9, no. 1, p. 37–53.

Nelson, W.J., and Krausse, H.F., 1981, The Cottage Grove fault system in southern Illinois: Illinois Institute of Natural Resources, State Geological Survey Division, Circular 522, 65 p.

Pakiser, L.C., Kane, M.F., and Jackson, W.H., 1964, Structural Geology and Volcanism and Owens Valley Region, California – A Geophysical Study: U.S. Geological Survey Professional Paper 438, 68 p.

Phillips, F.M., and Majkowski, L., 2011, The role of low-angle normal faulting in active tectonics of the northern Owens Valley California: Lithosphere, v. 3, p. 22-36, doi:10.1130/L73.1.

Pinter, N., 1995, Faulting on the Volcanic Tableland, Owens Valley, California: The Journal of Geology, v. 103, p. 73–83, doi:10.1086/629723.

Pinter, N., and Keller, E.A., 1995, Geomorphic analysis of neotectonic deformation, northern Owens Valley, California: Geologische Rundschau, in press.

Saltus, R.W., and Jachens, R.C., 1995, Gravity and Basin-Depth Maps of the Basin and Range Province, Western United States: U.S. Geological Survey Geophysical Investigation Map GP-1012.

Sheridan, M.F., 1970, Fumarolic Mounds and Ridges of the Bishop Tuff, California: Geological Society of America Bulletin, v. 81, p. 851-868, doi:10.1130/00167606(1970)81[851:FMAROT]2.0.CO;2.

Smith, K.D., 1987, Personal Experience of the 21 July 1986 M_L 6.4 Chalfant Valley Earthquake: Bulletin of the Seismological Society of America, v. 77, no. 1, p. 311-313.

Smith, K.D., and Priestly, K.F., 2000, Faulting in the 1986 Chalfant, California, Sequence – Local Tectonics and Earthquake Source Parameters: Bulletin of the Seismological Society of America, v. 90, p. 813-831.

Stevens, C.H., Stone, P., and Blakely, R.J., 2013, Structural Evolution of the East Sierra Valley System (Owens Valley and Vicinity), California: A Geologic and Geophysical Synthesis: Geosciences 2013, v.3, p.176-215, doi:10.3390/geosciences3020176.

Unruh, J., Humphrey, J., and Barron, A., 2003, Transtensional model for the Sierra Nevada frontal fault system, eastern California: Geology, v.31, p. 327-330, doi:10.1130/0091-7613(2003)031<0327:TMFTSN>2.0.CO;2.

Unruh, J.R., 1991, The uplift of the Sierra Nevada and implications for late Cenozoic epeirogeny in the western Cordillera: Geological Society of America Bulletin, v. 103, p.1395-1404.

Vaniman, D., 2006, Tuff Mineralogy: Geological Society of America Special Paper 408, 5 p.

Vazquez, J.A., and Woolford, J.M., 2015, Late Pleistocene ages for the most recent volcanism and glacial-pluvial deposits at Big Pine volcanic field, California, USA, from cosmogenic ^{36}Cl dating: Geochemistry, Geophysics, and Geosystems, v. 16, p. 2812-2828.

Wilson, C.J.N., and Hildreth, W., 1997, The Bishop Tuff: New insights from eruptive stratigraphy: The Journal of Geology, v. 105, p. 407–439, doi:10.1086/515937.

Zoback, M.L., and Zoback, M.D., 1989, Tectonic stress field of the continental United States: Geological Society of America, Memoir 172, p. 523-540.

Zoback, M.L., 1992, Stress-field constraints on intraplate seismicity in eastern North America: Journal of Geophysical Research, v. 97, p. 11761-11782.

APPENDICES

Table 1. Fault Kinematic Data

Fault Type	Fault strike	Fault dip	Striae trend	Striae plunge	Latitude	Longitude
Strike-Slip	32.00	88.00	32.02	1.73	37.49811	-118.5052
Strike-Slip	137.00	88.00	316.68	1.34	37.57723	-118.4830
Strike-Slip	223.00	73.00	229.24	18.00	37.57897	-118.4863
Strike-Slip	166.00	89.00	345.76	0.00	37.48845	-118.5052
Strike-Slip	165.00	88.00	344.88	4.42	37.48846	-118.5052
Strike-Slip	137.00	89.00	316.80	4.75	37.57723	-118.4830
Strike-Slip	139.00	85.00	317.79	10.42	37.57723	-118.4830
Strike-Slip	325.00	87.00	325.68	9.70	37.46835	-118.4432
Strike-Slip	220.00	86.00	220.21	10.79	37.43421	-118.4881
Strike-Slip	224.51	76.00	229.59	21.36	37.57893	-118.4863
Strike-Slip	224.51	80.00	228.05	19.89	37.57894	-118.4864
Strike-Slip	229.00	85.00	231.05	15.83	37.57897	-118.4863
Strike-Slip	169.00	88.00	348.40	13.46	37.48855	-118.5051
Strike-Slip	327.00	88.00	146.84	13.97	37.46823	-118.4431
Strike-Slip	326.00	87.00	145.26	15.68	37.46823	-118.4431
Strike-Slip	212.00	86.13	212.77	16.80	37.43421	-118.4881
Strike-Slip	225.00	80.00	229.67	25.79	37.57893	-118.4864
Strike-Slip	169.50	89.00	349.37	16.65	37.48855	-118.5051
Strike-Slip	330.00	85.00	148.03	21.98	37.46823	-118.4431
Strike-Slip	156.07	77.30	325.74	39.43	37.59325	-118.4460
Strike-Slip	129.00	89.00	306.05	57.03	37.45911	-118.5224
Normal	150.04	53.06	243.32	53.77	37.59983	-118.5059
Normal	141.01	54.46	232.54	52.74	37.59991	-118.5060
Normal	150.04	53.06	241.00	54.85	37.59979	-118.5059
Normal	141.01	54.46	233.37	53.77	37.59992	-118.5060
Normal	150.04	53.06	230.40	55.19	37.59988	-118.5060
Normal	140.94	56.63	239.18	52.31	37.59980	-118.5059
Normal	141.01	54.46	243.43	55.28	37.59985	-118.5060
Normal	141.01	54.46	243.49	55.67	37.59985	-118.5060
Normal	153.84	62.44	298.15	48.05	37.59572	-118.4463
Normal	175.99	59.85	292.93	53.23	37.59570	-118.4462
Normal	169.50	58.00	287.20	55.43	37.59282	-118.4461
Normal	169.50	59.71	245.23	56.51	37.59362	-118.5022
Normal	168.00	59.00	277.76	57.07	37.59280	-118.4461
Normal	169.50	59.71	250.00	56.75	37.59363	-118.5022
Normal	163.53	59.46	246.10	57.24	37.59253	-118.5015
Normal	169.50	59.71	259.66	57.37	37.59364	-118.5021

Normal	156.35	57.91	230.49	59.00	37.57500	-118.4786
Normal	150.99	60.80	251.86	56.41	37.59271	-118.5016
Normal	169.50	59.71	251.05	57.72	37.59351	-118.5021
Normal	169.50	59.71	250.03	57.82	37.59362	-118.5022
Normal	171.06	60.19	229.65	56.65	37.57499	-118.4786
Normal	135.50	59.96	256.66	56.92	37.59392	-118.5023
Normal	171.06	60.19	223.73	56.47	37.57501	-118.4786
Normal	171.06	60.19	230.56	56.98	37.57499	-118.4786
Normal	153.70	60.23	257.58	57.76	37.59321	-118.5020
Normal	167.34	56.78	251.35	61.47	37.59350	-118.5021
Normal	171.06	60.19	237.75	57.63	37.57500	-118.4786
Normal	171.06	60.19	237.72	57.76	37.57500	-118.4786
Normal	171.06	60.19	238.53	58.09	37.57500	-118.4786
Normal	167.34	56.78	247.92	61.96	37.59355	-118.5021
Normal	163.54	60.14	249.83	58.71	37.59305	-118.5018
Normal	169.00	60.00	277.56	58.60	37.59277	-118.4461
Normal	167.34	56.78	252.11	62.21	37.59355	-118.5021
Normal	167.34	56.78	249.65	62.44	37.59352	-118.5021
Normal	135.50	59.96	248.42	58.92	37.59393	-118.5024
Normal	167.34	56.78	256.32	62.77	37.59357	-118.5021
Normal	167.34	56.78	248.07	62.78	37.59354	-118.5021
Normal	169.50	59.71	262.09	60.16	37.59359	-118.5021
Normal	135.50	59.96	241.27	59.72	37.59395	-118.5023
Normal	167.34	56.78	250.86	63.13	37.59352	-118.5021
Normal	146.61	61.83	254.53	57.81	37.57735	-118.4832
Normal	171.06	60.19	232.73	59.07	37.57499	-118.4786
Normal	153.70	60.23	250.71	59.93	37.59326	-118.5020
Normal	140.94	56.63	254.51	63.03	37.59357	-118.5025
Normal	168.30	58.68	244.92	61.42	37.59222	-118.5012
Normal	167.34	56.78	258.54	63.56	37.59353	-118.5021
Normal	166.00	61.00	279.80	58.92	37.59280	-118.4461
Normal	167.34	56.78	254.84	63.78	37.59354	-118.5021
Normal	163.54	60.14	249.38	60.81	37.59308	-118.5018
Normal	169.50	59.71	254.95	61.27	37.59356	-118.5021
Normal	197.00	61.30	264.10	59.23	37.59277	-118.4461
Normal	145.76	61.42	248.47	59.50	37.59331	-118.5020
Normal	168.59	62.00	289.52	58.29	37.59277	-118.4461
Normal	169.50	59.71	251.94	61.53	37.59359	-118.5021
Normal	167.34	56.78	251.17	64.87	37.59350	-118.5021
Normal	169.50	59.71	252.42	62.10	37.59368	-118.5022
Normal	135.50	59.96	248.62	61.85	37.59392	-118.5024
Normal	147.00	61.00	239.87	61.41	37.57402	-118.4784
Normal	158.45	60.59	247.77	62.00	37.59322	-118.5019
Normal	158.45	60.59	237.78	61.90	37.59318	-118.5019
Normal	136.56	61.95	242.04	60.40	37.59335	-118.5020
Normal	152.59	63.59	265.93	58.46	37.59376	-118.5022

Normal	146.61	61.83	244.97	60.77	37.57737	-118.4832
Normal	151.54	61.97	246.88	61.06	37.59304	-118.5018
Normal	155.65	62.57	251.01	60.47	37.59311	-118.5018
Normal	152.59	63.59	241.60	59.56	37.59376	-118.5022
Normal	150.12	63.78	256.91	59.06	37.59378	-118.5022
Normal	156.58	61.17	253.24	61.93	37.59295	-118.5017
Normal	146.61	61.83	239.89	61.36	37.57735	-118.4832
Normal	152.74	61.99	243.55	61.21	37.59282	-118.5016
Normal	169.50	59.71	251.77	63.48	37.59356	-118.5021
Normal	152.74	61.99	247.85	61.25	37.59284	-118.5016
Normal	150.12	63.78	261.27	59.14	37.59374	-118.5022
Normal	135.50	59.96	260.52	62.13	37.59384	-118.5023
Normal	136.56	61.95	251.00	60.85	37.59335	-118.5020
Normal	136.56	61.95	244.98	61.14	37.59331	-118.5020
Normal	158.49	63.47	256.47	59.94	37.59374	-118.5022
Normal	147.00	62.00	239.05	61.53	37.57402	-118.4784
Normal	149.89	63.32	252.53	60.23	37.59294	-118.5017
Normal	146.61	61.83	240.11	61.92	37.57738	-118.4832
Normal	136.56	61.95	251.47	61.18	37.59336	-118.5020
Normal	146.40	60.89	238.13	63.05	37.59197	-118.5011
Normal	135.50	59.96	246.52	63.62	37.59367	-118.5023
Normal	146.61	61.83	234.73	62.24	37.57738	-118.4832
Normal	150.12	63.78	254.28	60.11	37.59368	-118.5022
Normal	150.12	63.78	264.64	59.66	37.59373	-118.5022
Normal	158.49	63.47	258.46	60.62	37.59374	-118.5022
Normal	135.50	59.96	255.53	63.42	37.59388	-118.5023
Normal	150.12	64.74	250.45	59.54	37.59338	-118.5020
Normal	136.56	61.95	250.65	61.83	37.59346	-118.5020
Normal	169.50	59.71	251.91	64.69	37.59354	-118.5021
Normal	135.50	59.96	254.74	63.63	37.59386	-118.5023
Normal	150.12	63.78	250.52	60.63	37.59366	-118.5022
Normal	158.49	63.47	254.29	61.07	37.59368	-118.5022
Normal	150.12	63.78	249.40	60.72	37.59364	-118.5022
Normal	152.59	63.59	255.14	60.85	37.59380	-118.5023
Normal	150.12	63.78	249.43	60.84	37.59366	-118.5022
Normal	152.59	63.59	252.26	61.05	37.59372	-118.5022
Normal	152.59	63.59	257.98	60.89	37.59372	-118.5022
Normal	152.59	63.59	257.25	60.94	37.59372	-118.5022
Normal	150.12	63.78	249.97	60.88	37.59366	-118.5022
Normal	150.12	63.78	260.80	60.59	37.59370	-118.5022
Normal	135.50	59.96	256.44	63.93	37.59387	-118.5023
Normal	150.12	63.78	248.71	61.30	37.59369	-118.5022
Normal	135.50	59.96	261.22	63.86	37.59382	-118.5023
Normal	128.31	64.46	234.77	60.56	37.57735	-118.4832
Normal	136.81	63.00	230.87	62.32	37.57723	-118.4830
Normal	152.59	63.59	248.00	61.82	37.59372	-118.5022

Normal	173.54	63.00	252.97	62.50	37.58750	-118.5004
Normal	150.12	63.78	255.84	61.79	37.59371	-118.5022
Normal	150.12	63.78	247.50	62.31	37.59366	-118.5022
Normal	150.12	63.78	259.98	62.16	37.59367	-118.5022
Normal	180.71	63.26	263.26	63.17	37.58754	-118.5004
Normal	150.12	64.74	253.42	61.60	37.59349	-118.5020
Normal	150.12	64.74	247.03	61.80	37.59349	-118.5020
Normal	150.12	64.74	248.91	62.25	37.59336	-118.5020
Normal	150.12	63.78	256.74	63.29	37.59372	-118.5022
Normal	147.17	67.29	247.64	60.18	37.59261	-118.5015
Normal	150.12	64.74	244.14	63.01	37.59343	-118.5020
Normal	180.71	63.26	256.11	64.49	37.58751	-118.5004
Normal	196.64	65.24	277.20	62.68	37.59594	-118.4462
Normal	196.64	65.24	284.97	63.56	37.59280	-118.4462
Normal	131.09	68.42	252.43	60.03	37.59338	-118.5020
Normal	147.17	67.29	242.22	62.41	37.59275	-118.5016
Normal	147.00	65.00	245.23	64.76	37.57402	-118.4784
Normal	147.17	67.29	238.50	62.68	37.59266	-118.5015
Normal	131.09	68.42	248.11	60.66	37.59338	-118.5020
Normal	144.50	65.91	229.72	64.35	37.57754	-118.4834
Normal	131.09	68.42	252.99	61.29	37.59336	-118.5020
Normal	167.00	66.00	244.93	65.11	37.59337	-118.4462
Normal	131.09	68.42	248.78	62.00	37.59337	-118.5020
Normal	144.50	65.91	228.82	65.56	37.57754	-118.4834
Normal	131.09	68.42	246.43	62.31	37.59337	-118.5020
Normal	183.90	68.67	282.09	63.12	37.58749	-118.5002
Normal	161.95	67.39	227.34	63.94	37.57721	-118.4830
Normal	131.09	68.42	251.71	62.82	37.59347	-118.5020
Normal	135.50	59.96	263.64	70.96	37.59391	-118.5023
Normal	143.61	66.30	243.61	66.28	37.57748	-118.4835
Normal	141.92	67.08	228.91	65.96	37.57755	-118.4834
Normal	160.20	66.13	224.97	66.39	37.57723	-118.4830
Normal	175.99	66.85	273.45	66.49	37.59588	-118.4462
Normal	196.03	66.25	275.25	67.35	37.58753	-118.5002
Normal	196.03	66.25	257.47	66.52	37.58758	-118.5002
Normal	147.17	67.29	237.99	66.59	37.59278	-118.5016
Normal	199.81	68.79	264.13	65.85	37.58758	-118.5003
Normal	140.40	68.51	241.31	67.07	37.57690	-118.4826
Normal	140.40	68.51	250.56	66.95	37.57690	-118.4826
Normal	145.98	68.54	217.31	67.07	37.57723	-118.4830
Normal	173.54	71.25	265.98	64.94	37.58746	-118.5004
Normal	158.00	69.12	219.34	66.22	37.51551	-118.4310
Normal	145.98	68.54	214.19	67.69	37.57724	-118.4830
Normal	190.94	70.00	240.30	64.66	37.58751	-118.5003
Normal	143.74	69.68	241.07	68.15	37.57692	-118.4826
Normal	143.74	69.68	257.02	68.85	37.57693	-118.4826

Normal	141.00	70.00	223.04	69.48	37.57741	-118.4834
Normal	151.30	71.69	249.81	67.99	37.57721	-118.4830
Normal	146.55	70.38	229.06	69.50	37.57723	-118.4830
Normal	155.10	70.45	222.30	69.05	37.57722	-118.4830
Normal	140.40	68.51	235.90	72.12	37.57692	-118.4826
Normal	145.98	68.54	237.87	73.09	37.57719	-118.4830
Normal	176.99	70.85	275.21	70.72	37.59598	-118.4462
Normal	151.55	69.21	244.62	72.56	37.57722	-118.4830
Normal	173.78	72.94	294.74	68.83	37.59375	-118.4463
Normal	138.11	72.45	251.11	70.04	37.57714	-118.4830
Normal	153.00	74.00	248.89	69.38	37.57721	-118.4830
Normal	156.60	87.11	232.17	56.47	37.59985	-118.5060
Normal	182.05	71.26	231.46	70.81	37.57720	-118.4829
Normal	136.00	73.00	232.41	72.17	37.57748	-118.4835
Normal	179.00	73.00	263.12	72.40	37.51541	-118.4310
Normal	196.00	73.12	260.94	71.50	37.51526	-118.4311
Normal	141.00	73.00	238.85	72.67	37.57746	-118.4834
Normal	151.30	71.69	236.60	74.11	37.57720	-118.4830
Normal	154.00	72.89	238.84	73.00	37.57723	-118.4830
Normal	170.60	73.00	254.15	72.94	37.57721	-118.4830
Normal	197.15	74.00	289.05	74.41	37.59566	-118.4463
Normal	149.00	74.00	241.01	74.50	37.57719	-118.4830
Normal	175.00	74.12	273.76	75.18	37.51556	-118.4310
Normal	151.30	74.89	244.05	74.74	37.57723	-118.4830
Normal	187.00	74.82	254.20	74.25	37.51547	-118.4311
Normal	343.00	75.00	94.35	74.20	37.57367	-118.4791
Normal	210.52	76.12	270.70	73.58	37.51556	-118.4310
Normal	344.00	76.00	71.15	75.91	37.57367	-118.4791
Normal	210.00	77.00	345.47	72.23	37.59754	-118.4467
Normal	182.05	77.26	228.03	72.15	37.57719	-118.4829
Normal	347.00	76.70	59.88	76.20	37.57400	-118.4783
Normal	145.98	77.00	249.97	76.41	37.57719	-118.4830
Normal	345.00	77.00	78.34	76.84	37.57367	-118.4791
Normal	344.33	77.70	58.96	77.06	37.57402	-118.4783
Normal	341.00	78.00	87.35	77.29	37.57367	-118.4791
Normal	175.00	78.00	296.85	76.49	37.59374	-118.4463
Normal	326.00	79.00	106.43	73.27	37.57751	-118.4835
Normal	145.21	78.00	226.22	78.05	37.59572	-118.4463
Normal	193.00	78.12	283.45	78.43	37.51550	-118.4310
Normal	153.00	78.89	219.28	77.99	37.57723	-118.4830
Normal	5.40	80.00	105.63	80.09	37.59271	-118.4462
Normal	158.34	79.49	288.57	80.36	37.59571	-118.4463
Normal	3.81	81.00	108.16	81.45	37.59271	-118.4462
Oblique	155.00	77.00	310.31	60.90	37.45912	-118.5224
Oblique	134.00	79.00	290.35	65.25	37.45909	-118.5225
Oblique	132.00	80.00	290.96	64.34	37.45909	-118.5225

Oblique	133.20	84.69	301.89	60.26	37.59572	-118.4463
Oblique	158.00	83.00	172.74	64.35	37.60731	-118.5093
Oblique	159.07	84.00	172.77	63.19	37.60729	-118.5093
Oblique	126.00	81.00	279.12	70.41	37.45909	-118.5225
Oblique	213.22	83.20	227.33	64.64	37.51530	-118.4311
Oblique	127.00	81.00	280.89	71.07	37.45909	-118.5225
Oblique	125.00	83.00	288.36	67.27	37.45909	-118.5225
Oblique	142.00	85.00	312.09	63.55	37.45911	-118.5224
Oblique	200.52	81.12	232.60	74.06	37.51543	-118.4311
Oblique	129.00	83.00	291.24	68.94	37.45917	-118.5225
Oblique	164.00	86.00	173.43	63.14	37.60730	-118.5093
Oblique	351.81	83.00	13.16	70.62	37.59754	-118.4467
Oblique	353.00	84.00	11.67	69.96	37.59754	-118.4467
Oblique	136.00	83.00	291.92	72.62	37.45917	-118.5225
Oblique	351.81	83.00	13.32	72.43	37.59754	-118.4467
Oblique	353.00	84.00	9.46	70.35	37.59754	-118.4467
Oblique	160.00	86.00	169.91	66.00	37.60728	-118.5093
Oblique	161.00	85.00	173.10	68.50	37.60730	-118.5093
Oblique	319.05	87.00	133.23	63.91	37.57751	-118.4835
Oblique	203.52	83.12	232.33	75.85	37.51545	-118.4311
Oblique	314.00	83.00	104.53	76.96	37.57751	-118.4835
Oblique	160.00	87.00	167.09	65.63	37.60732	-118.5093
Oblique	156.00	85.00	168.30	70.24	37.60730	-118.5092
Oblique	45.31	82.94	92.04	80.16	37.59272	-118.4462
Oblique	206.82	85.12	224.91	72.23	37.51530	-118.4311
Oblique	161.00	86.00	171.52	68.96	37.60730	-118.5092
Oblique	141.00	84.00	297.14	76.16	37.45917	-118.5225
Oblique	159.34	83.00	281.43	82.33	37.59571	-118.4463
Oblique	162.47	84.24	209.69	82.12	37.59868	-118.4470
Oblique	163.00	84.00	238.02	83.97	37.59868	-118.4470
Oblique	161.47	83.88	222.46	83.97	37.59868	-118.4470
Oblique	171.82	86.53	254.54	85.82	37.59742	-118.4467
Oblique	138.82	87.43	178.32	83.16	37.45992	-118.4723
Oblique	138.82	87.43	182.21	83.55	37.45993	-118.4723
Oblique	138.82	87.43	247.11	85.02	37.46528	-118.4674
Oblique	138.82	87.43	242.91	85.12	37.46528	-118.4674
Oblique	179.00	87.00	192.29	79.73	37.59741	-118.4467
Oblique	138.82	87.43	182.03	84.54	37.45992	-118.4723
Oblique	171.82	86.53	277.62	86.96	37.59741	-118.4467
Oblique	138.82	87.43	259.31	85.70	37.46528	-118.4674
Oblique	171.82	86.53	211.81	86.28	37.59742	-118.4467
Oblique	153.34	87.00	307.35	84.30	37.59571	-118.4463
Oblique	225.13	88.53	229.50	76.69	37.59572	-118.4463
Oblique	177.00	89.00	184.25	77.04	37.59741	-118.4467
Oblique	201.34	88.37	225.89	84.95	37.58482	-118.4997
Oblique	138.82	87.43	277.78	87.95	37.46528	-118.4674

Table 2. Mineralized Joint Data (UTM Zone 11 N)

Strike	Dip	X (Easting)	Y (Northing)
169.34	77.76	360771.53	4154560.99
84.98	88.44	360771.73	4154561.16
174.66	88.39	360772.25	4154560.77
178.22	82.36	360772.68	4154560.59
265.72	88.15	360772.95	4154560.87
85.04	83.28	360772.96	4154563.88
85.19	88.37	360772.96	4154563.88
81.92	87.22	360773.02	4154560.33
79.41	84.45	360775.05	4154560.68
356.81	89.00	360775.39	4154556.38
172.61	82.86	360777.02	4154560.79
86.09	83.73	360786.97	4154561.41
93.01	83.66	360798.77	4154650.84
188.11	76.52	360803.72	4154705.63
65.39	77.82	360804.32	4154759.56
87.19	86.89	360806.06	4154683.35
196.63	78.53	360806.08	4154703.04
87.73	87.47	360806.8	4154651.53
81.95	81.27	360807.68	4154701.37
83.44	80.17	360810.66	4154701.46
281.67	87.72	360812.3	4154699.67
201.22	73.50	360813.17	4154700.15
76.37	73.19	360813.72	4154700.24
79.06	65.52	360815.09	4154701.08
80.87	81.47	360815.3	4154702.45
73.56	70.72	360815.68	4154700.09
191.86	78.96	360818.31	4154703.16
93.05	84.49	360842.03	4154695.83
9.59	82.35	365332.18	4146929
306.89	83.18	365332.18	4146929
122.87	87.01	365332.18	4146929
128	89.00	365332.18	4146929
202.44	85.87	365334.65	4146926.35
295.02	89.00	365334.65	4146926.35
228.09	89.00	365334.65	4146926.35
190.2	89.00	365334.65	4146926.35
314.94	78.44	365335.67	4146924.96
244.53	83.87	365628.21	4150314.21
164.34	85.87	365632.94	4150343.01
339.77	84.37	365648.28	4150376.13
324.55	63.84	365656.65	4152015.27
338.68	63.84	365661.77	4151998.75
274.85	72.25	365684.4	4150373

100.1	75.69	365685.09	4150346.01
352.92	81.52	365687.4	4150356.41
292.26	88.93	365701.83	4150369.05
106.83	77.86	365702.83	4150366.71
354.64	87.01	365703.78	4150368.84
353.3	74.02	365704.31	4150363.25
5.42	87.09	365708.91	4150370.89
354.11	85.99	365710.77	4150368.67
124.22	61.62	365712.44	4150354.85
6.76	77.91	365713.57	4150358.75
194.28	84.94	365719.97	4150369.18
206.28	82.77	365730.03	4150359.73
127.92	88.16	365731.03	4150363.61
30.35	86.99	365731.7	4150368.23
53.13	83.12	365732.21	4150355.12
40.59	85.13	365736.99	4150348.91
77.17	81.24	365740.33	4150345.13
43.36	87.03	365747.79	4150354.54
340.38	89.00	366079.34	4144582.96
209.85	86.59	366086.49	4144580.33
13.97	84.54	366108.59	4141706.24
208.47	72.69	366109.37	4141704.09
31.08	78.42	366110.03	4141707.32
199.07	88.61	366957.55	4140461.33
195.95	82.54	366966.04	4140456.15
27.4	87.99	366967.15	4140457.4
18.18	85.82	366969.63	4140458.48
205.05	88.92	366975.16	4140460.23
22.06	76.41	368261.13	4150622.01
33.79	78.00	368261.31	4150621.98
149.69	86.93	368261.86	4150539.23
334.68	88.06	368269.62	4150625.6
348.22	84.60	368269.75	4150617.46
156.99	77.40	368281.44	4150628.71
170.42	87.05	368316.71	4150359.06
71.92	82.07	368316.89	4150655.41
351.37	89.00	368317.2	4150655.99
254.59	87.19	368317.82	4150641
340.74	80.00	368318.08	4150635.9
344.59	85.80	368318.39	4150642.68
201.44	80.68	368320.22	4150372.93
352.93	84.27	368321.83	4150633.69
205.32	84.81	368321.83	4150366.14
353.19	88.62	368325.61	4150420.52
195.76	81.86	368326.95	4150436.8
153.15	86.96	368337.53	4150631.29

206.2	86.25	368338.8	4150436.46
245.18	81.21	368362.07	4150260.21
227.49	87.64	368364.58	4150268.11
18.29	70.36	368364.77	4150263.82
178.68	52.62	368365.45	4150606.49
201.35	83.34	368365.9	4150248.31
192.15	89.00	368366.92	4150611.37
10.1	79.38	368370.67	4150259.02
321.7	75.04	368371.46	4150256.51
334.13	74.26	368372.42	4150252.89
118.26	82.17	368373.06	4150245.77
275.84	83.68	368373.4	4150630.76
118.66	86.81	368375.36	4150469.19
29.79	73.30	368376.35	4150254.88
187.52	87.20	368376.38	4150615.23
292.71	61.70	368376.51	4150239.44
306.88	61.55	368378.97	4150240.98
277.32	84.12	368380.19	4150628.21
188.14	88.62	368382.16	4150626.28
197.75	88.70	368404.73	4150611.86
200.58	87.05	368435.08	4150601.73
229.88	77.78	369048.79	4159949.03
68.05	84.94	369049.31	4159948.2
256.23	87.57	369049.76	4159947.27
204.03	83.91	369063.07	4159920.32
226.73	82.78	369068.77	4159913.24
90.95	82.07	369069.14	4159918.69
70.23	81.49	369069.58	4159914.42
154.55	88.23	369089.91	4159902.4
49.41	89.00	369185.44	4145647.65
225.9	89.00	369186.61	4145648.45
276.74	88.32	369188.53	4145640.78
163.5	88.37	369188.7	4145641.29
234.68	87.76	369189.46	4145649.68
151.61	85.96	369189.48	4145648.71
255.43	82.56	369190.59	4145629.37
253.75	83.68	369190.59	4145629.37
346.92	85.80	369190.59	4145629.37
353.7	85.80	369191.98	4145627.38
344.04	87.27	369193.32	4145623.15
345.3	88.24	369194.28	4145613.44
187.27	85.79	369195.98	4145650.19
74.79	89.00	369198.57	4145640.11
229.32	79.61	369200.52	4145662.95
79.9	89.00	369205.55	4145640.47
333.53	88.73	369215.87	4145642.7

230.57	89.00	369387.37	4159729.98
209.22	83.01	369596.49	4145532.45
125.25	84.79	369596.62	4145533.75
116.53	82.74	369597.45	4145531.94
14.61	89.00	369598.29	4145534.02
107.04	56.84	369598.48	4145527.47
96.06	74.30	369598.48	4145527.47
95.24	73.30	369599.35	4145528.18
120.75	83.94	369602.1	4145531.48
124.59	87.44	369602.1	4145531.48
356.24	75.72	369606.46	4145517.17
188.59	80.25	369613.33	4145500.54
285.92	88.24	369613.33	4145500.54
184.93	87.10	369829.25	4147001.59
341.38	86.35	369859.15	4145374.38
234.03	74.42	369859.44	4145374.36
250.68	81.34	369862.2	4145377.75
182.42	84.88	369862.28	4145376.56
44.13	77.98	369953.74	4145482.61
195.89	81.77	369954.71	4145482.1
280.31	79.68	369954.91	4145483.96
200.32	82.84	369954.91	4145483.96
287.59	81.18	369954.97	4145483.89
199.27	80.94	369955.11	4145482.5
277.59	81.51	369956.12	4145484.89
281.67	82.93	369957.29	4145482.6
35.23	85.46	369957.71	4145482.58
23.87	89.00	369979.47	4155818.42
132.75	87.12	369981.26	4155822.62
27.57	87.13	369992.08	4155821.56
220.9	88.28	369994.47	4155816.32
124.11	87.03	369995.89	4155824.13
209.94	73.26	369996.89	4155811.6
207.01	78.76	370000.96	4155830.98
8.42	88.09	370001.72	4155820.36
171.91	84.36	370009.78	4155821.47
160.1	84.15	370012.48	4155815.92
167.84	82.85	370013.07	4155808.46
170.56	84.97	370013.38	4155797.94
168.9	80.44	370013.93	4155804.49
84.47	89.00	370015.13	4155803.04
162.5	86.03	370015.81	4155803.58
169.17	84.23	370016.39	4155803.65
151.39	81.39	370020.37	4155806.11
168.26	88.19	370035.58	4155798.67
165.24	89.00	370038.41	4155798.34

172.29	78.55	370047.36	4155804.57
357.59	85.06	370048.62	4145565.11
33.86	84.16	370048.84	4145564.38
150.39	86.34	370049.36	4145570.66
55.07	88.14	370049.36	4145570.66
240.13	89.00	370049.36	4145570.66
76.75	88.34	370050.06	4145568.38
58.15	84.45	370111.13	4145569.43
355.95	87.14	370113.63	4145570.89
20.61	88.24	370117.56	4155795.67
177.08	86.79	370120.67	4155795.02
356.56	84.42	370120.99	4145570.61
5.13	89.00	370121.67	4155792.73
74.36	81.45	370122.2	4145570.81
8.45	87.31	370122.88	4155795.86
185.59	89.00	370124.09	4155795.43
190.61	86.81	370126.89	4155790.78
189.44	85.95	370127.98	4155791.97
8.45	89.00	370130.75	4155796.02
75.38	89.00	370150.21	4145592.56
169.83	85.13	370151.1	4145592.88
333.45	88.49	370151.1	4145592.88
165.5	81.53	370151.56	4145594.56
101.22	81.39	370153.56	4145593.85
343.86	89.00	370153.63	4145593.06
251.5	86.83	370153.93	4145596.48
80.05	81.80	370154.32	4145597.38
168.02	83.38	370154.39	4145595.2
137.91	88.86	370161.59	4145593.64
232.72	89.00	370162.36	4145594.78
143.65	88.16	370163.74	4145591.61
169	81.65	370186.52	4155872.94
18.09	88.44	370190.34	4155865.52
277.79	87.38	370205.19	4155853.97
206.64	74.46	370210.48	4145601.68
294.16	89.00	370210.48	4145601.68
297.09	84.54	370210.95	4145602.53
254.15	77.71	370211.58	4145599.8
184.44	83.26	370211.71	4145595.75
267.86	85.03	370211.73	4145597.08
269.28	81.60	370212.18	4145596.88
269.42	87.49	370212.44	4145595.88
201.78	79.86	370213.05	4145600.56
318.78	86.57	370216.2	4147559.74
177.64	80.62	370216.28	4145602.61
192.77	84.70	370216.77	4155850.93

203.78	76.67	370217.09	4145605.32
352.53	88.86	370218.9	4147584.68
358.45	89.00	370219.98	4147555.52
199.05	81.63	370221.86	4147581.35
326.84	88.49	370224.46	4147540.42
359.28	88.80	370225.85	4147543.83
113.12	86.39	370227.43	4147542.47
19.84	87.66	370231.61	4147568.34
215.17	87.84	370232.6	4147529.2
62.18	77.91	370234.97	4147584.59
359.46	83.95	370236.25	4147516.98
273.65	83.40	370247.54	4145596.08
249.29	74.44	370248.07	4145590.55
80.04	88.53	370248.39	4145600.21
6.81	83.45	370249.81	4145604.39
6.49	86.74	370251.26	4145603.78
152.82	83.02	370252.32	4145606.98
76.24	89.00	370253.48	4145608.6
318.54	86.22	370574.28	4149480.01
311.85	88.66	370594.1	4149467.31
144.06	89.00	370609.22	4149446.62
325.52	88.58	370712.9	4149364.85
146.48	89.00	370714.28	4149375.16
319.68	89.00	370727.05	4149355.1
156.29	84.01	370765.78	4149265.2
324.04	88.69	370768.9	4149262.5
297.25	88.13	370882.4	4154932.89
296.89	88.98	370892.3	4154940.91
203.32	85.72	370904.58	4154773.68
208.15	85.00	370904.9	4154769.59
245.96	84.01	370905.61	4154767.6
341.06	87.93	370905.96	4154776.21
215.05	81.34	370907.98	4154784.86
129.57	81.29	370916.82	4154798.17
314.21	82.19	370919.45	4154845.38
327.36	81.39	370921.75	4154844.88
319.68	83.65	370922.59	4154845.21
146.96	81.79	370934.51	4154783.36
98.29	78.69	370940.54	4154791.98
248.33	77.57	370957.45	4154820.17
38.44	89.00	371332.6	4154596.66
197.08	82.94	371333.58	4154573.56
201.83	84.28	371333.86	4154571.5
98.61	79.86	371334.66	4154598.77
163.78	87.92	371335.94	4154599.63
192.94	88.48	371336.03	4154567.68

87.81	86.13	371336.34	4154556.96
95.31	83.70	371336.35	4154599.74
260.73	86.16	371336.35	4154599.74
179.03	83.71	371336.38	4154599.85
163.42	84.31	371336.83	4154601.49
9.62	89.00	371337.78	4154567.75
194.71	84.37	371338.72	4154565.24
190.63	79.15	371339.09	4154562.92
173.05	87.98	371340.14	4154565.86
12.51	88.02	371350.01	4154570
42.84	87.40	371358.55	4154554.16
25.2	74.25	371359.7	4154561.94
45.75	84.54	371360.52	4154555.01
271.6	82.76	371365.91	4154560.54
249.93	89.00	371365.91	4154560.54
5.34	83.99	371375.65	4154557.58
333.65	87.77	371775.3	4146544.87
283.59	89.00	371778.21	4146531.13
125.71	85.14	371778.71	4146534.18
224.67	82.33	371779.06	4146525.26
148.76	76.32	371781.94	4146549.66
206.03	78.45	371784.81	4146514.27
132.96	72.17	371788.67	4146484.16
162.87	81.48	371788.81	4146493.27
60.01	89.00	371788.81	4146493.27
153.71	82.15	371788.95	4146502.77
133.55	81.42	371788.99	4146483.35
147.61	75.18	371789.9	4146486.09
46.27	89.00	371789.93	4146487.5
155.43	89.00	371790.16	4146490.04
353.21	85.96	371790.66	4146488.28
171.03	88.84	371791.07	4146496.3
234.58	87.32	371791.32	4146489.2
271.32	61.62	371791.51	4146505.77
190.47	62.60	371792.98	4146513.82
173.63	54.24	371793.48	4146515.58
203.04	70.46	371793.75	4146512.56
0.53	71.76	371796.76	4146482.74
71.21	89.00	371797.25	4146484.3
216.76	81.32	372298.98	4161518.68
150.37	76.20	372300.87	4161516.53
333.09	79.67	372310	4161592.63
253.96	89.00	372315.17	4161595.65
0.52	75.53	372322.06	4161965.69
96.76	86.64	372322.96	4161962.99
336.71	62.48	372323.81	4161961.6

255.35	89.00	372325.53	4161964.09
155.66	71.38	372325.58	4161597.82
337.84	56.98	372325.59	4161972.08
59.88	88.37	372325.59	4161972.08
157.55	87.17	372325.69	4161598.66
102.07	79.18	372328.33	4161965.79
278.3	67.51	372340.11	4161615.26
52.18	77.41	372346.74	4161610.17
41.04	81.54	372349.65	4161615.11
338.84	89.00	372446.57	4145243.05
100.21	84.57	372448.26	4145184.41
101.82	86.32	372450.2	4145191.69
196.01	73.49	372450.94	4145261.67
286.93	84.72	372451.56	4145193
265.83	87.26	372459.32	4145198.61
346.3	81.61	372460.83	4145191.39
37.1	89.00	372465.83	4145428.43
120.4	68.11	372474.52	4145425.96
243.61	58.99	372474.97	4145265.55
219.86	62.68	372475.58	4145266.5
218.49	71.06	372477.81	4145270.94
226.34	67.32	372485.93	4145283.37
121.3	82.15	372488.62	4145417.11
251.11	75.23	372492.75	4145293.24
236.35	81.99	372500.76	4145302.6
301.97	75.21	372502.23	4145297.9
319.34	85.03	373233.48	4167920.41
56.2	81.08	373234.15	4167921
51.96	86.95	373234.15	4167921
84.46	84.82	373259.97	4167920.76
18.03	84.82	373291.06	4167953.1
178.41	89.00	373292.38	4167957.06
138.18	85.42	373297.7	4167955.79
294.2	81.51	373306.75	4167953.42
201.76	80.39	373315.08	4167947.05
9.21	89.00	373321.17	4167963.53
37.54	89.00	373322.26	4167967.5
355.57	78.61	373322.3	4167974.42
12.85	88.07	373323.65	4167965.81
273.02	81.87	373324.26	4168009.95
16.76	87.72	373324.71	4167966.99
227.27	87.53	373331.72	4167978.17
6.74	79.45	373333.46	4168017.1
1.4	88.55	373336.09	4167980.65
359.75	77.44	373336.26	4167982.1
195.17	80.39	373337.34	4167971.44

0.58	86.26	373337.98	4167974.8
291.85	83.83	373341.66	4168009.18
200.84	85.47	373342.65	4168009.2
24.85	87.35	373343.32	4168011.52
105.79	80.28	373345.36	4168038.25
279.81	78.14	373345.44	4168052.18
111.37	89.00	373346.9	4168042
107.05	76.31	373349.83	4168046.53
285.01	77.75	373349.86	4168051.09
346.27	77.01	373351.23	4168015.42
175.27	84.14	373351.33	4168052.58
270.1	85.98	373352.62	4168017.81
175.66	67.13	373352.77	4168054.32
182.75	80.55	373353.65	4168052.69
2.83	89.00	373356.25	4168030.68
173.27	86.86	373363.92	4168024.19
174.73	87.03	373364.91	4168000.89
268.52	80.44	373366.09	4167999.18
178.03	81.96	373366.74	4168027.27
357.19	55.03	373368.77	4168000.94
21.3	86.66	373385.31	4168007.1
199.51	79.31	373393.67	4168003.35
93.09	84.26	373393.79	4168002.02
13.57	86.84	373397.12	4168009.84
11.66	78.45	373400.03	4168011.92
20.4	89.00	373408.28	4168010.18
209.05	84.84	373415.09	4168014.12
16.27	88.26	373422.17	4168014.91
288.24	75.28	373422.28	4168018.12
275.56	81.82	373422.56	4168015.04
189.17	73.55	373425.18	4168025.24
18.27	75.42	373587.36	4144009.84

Table 3. Non-Mineralized Joint Data (UTM Zone 11 N)

Strike	Dip	X (Easting)	Y (Northing)
243.65	75.85	371767.272	4142139.85
322.66	86.52	371766.761	4142138.45
293.09	64.52	371768.803	4142137.57
311.02	72.58	371769.477	4142140.43
189.96	75.34	371769.696	4142145.01
172.74	74.99	371765.092	4142093.61
82.26	79.11	371787.561	4142086.52
215.93	86.12	371787.525	4142088.05
59.34	84.34	371787.525	4142088.05
217.47	83.79	371787.525	4142088.05
227.77	83.80	371793.259	4142091.86
197.40	82.88	371794.738	4142093.94
198.95	73.25	371783.063	4142092.22
147.45	76.17	371785.204	4142092.5
105.80	81.24	371785.916	4142092.97
312.21	82.88	371782.262	4142090.79
222.77	87.06	371788.278	4142087.8
109.69	88.21	371786.968	4142087.55
135.13	89.00	371784.46	4142087.53
66.60	70.03	371784.065	4142087.93
56.03	69.26	371782.465	4142089.02
256.06	79.06	371763.85	4142134.88
304.25	83.85	371764.458	4142133.89
272.96	85.91	371760.03	4142136.4
358.31	87.15	371759.613	4142135.84
172.04	47.21	371761.648	4142133.1
292.62	86.28	371762.047	4142134.43
325.39	89.00	371760.416	4142136.46
159.12	86.46	371735.321	4142121.77
250.96	78.16	371740.203	4142124.19
246.02	78.22	371759.007	4142116.21
182.40	84.96	371765.193	4142119.96
312.06	89.00	371754.49	4142135.2
80.77	88.95	371758.266	4142121.07
311.08	86.06	371748.778	4142128.91
320.31	73.79	371759.778	4142128.21
308.82	86.82	371759.778	4142128.21
290.32	86.57	371759.778	4142128.21
95.28	81.51	371759.778	4142128.21
220.96	72.43	371759.778	4142128.21
187.53	65.40	371759.778	4142128.21
252.15	86.21	372486.329	4145495.82
146.64	59.18	372485.501	4145494.54

197.82	55.96	372488.626	4145491.31
1.27	76.16	372488.605	4145492.41
221.57	80.16	372487.978	4145472.23
13.25	86.04	372484.163	4145470.13
87.52	86.07	372484.049	4145464.64
184.78	89.00	372488.122	4145466.64
274.23	80.81	372487.417	4145468.54
280.96	87.03	372485.083	4145464.34
93.23	86.37	372485.355	4145458.86
177.65	85.42	372482.716	4145444.89
270.44	86.52	372501.66	4145455.2
92.83	86.22	372489.217	4145451.45
88.69	80.82	372490.168	4145452.54
197.09	65.24	372489.556	4145451.81
93.94	70.85	372489.901	4145452.06
158.59	89.00	372483.836	4145436.64
238.74	82.32	372483.836	4145436.64
91.67	77.77	372483.328	4145433.45
136.57	83.86	372482.314	4145433.64
36.90	88.80	372483.836	4145431.79
200.36	71.96	372484.062	4145430.53
271.84	79.34	366792.353	4150794.11
135.14	85.58	366792.096	4150791.46
31.61	63.40	366779.8	4150755.87
311.60	89.00	366780.308	4150753.77
32.80	88.16	366777.482	4150752.29
208.29	89.00	366776.949	4150752.31
306.95	86.06	366776.49	4150749.11
162.25	85.31	366931.638	4150133.27
179.37	77.06	366935.122	4150128.63
179.96	80.64	366930.368	4150125.72
265.57	85.02	366930.368	4150125.72
2.52	87.14	366930.368	4150125.72
120.94	85.03	366927.786	4150125.57
114.57	82.41	366928.751	4150126.1
285.92	88.24	366937.045	4150121.42
188.59	80.25	366934.743	4150121.64
356.24	75.72	366934.419	4150121.33
96.06	74.30	366931.915	4150118.65
107.04	56.84	366937.481	4150103.72
95.24	73.30	366945.384	4150096.41
209.22	83.01	366940.925	4150093.8
125.25	84.79	366929.984	4149966.8
116.53	82.74	366933.195	4149960.84
14.61	89.00	366941.608	4149958.07
124.59	87.44	366941.608	4149958.07

120.75	83.94	366933.248	4149966.96
183.99	79.19	366931.507	4149966.57
199.81	73.82	366931.309	4149968.11
207.35	81.93	366967.003	4149847.19
213.68	81.83	366960.901	4149848.06
208.83	81.70	366943.714	4149864.46
284.62	87.94	367025.821	4149855.45
283.30	86.46	366960.403	4149847.96
279.54	85.69	366960.734	4149847.83
11.47	82.36	366959.065	4149845.41
10.46	81.47	366972.202	4149851.99
275.97	81.09	366975.081	4149858.2
189.62	87.05	366949.641	4149842.02
293.92	85.22	366947.284	4149840.15
290.82	85.04	366917.731	4149833.32
12.70	80.79	366964.004	4149845.06
215.68	79.52	366973.638	4149847.28
298.13	84.81	366964.789	4149825.59
299.38	83.70	366965.331	4149849.3
298.00	84.93	366965.331	4149849.3
300.62	85.60	366965.331	4149849.3
297.16	84.65	366965.331	4149849.3
128.00	84.17	366982.552	4149832.64
115.31	87.59	366964.43	4149821.16
311.87	88.65	367201.89	4149409.8
311.52	88.29	366968.308	4149813.37
312.53	84.39	366968.308	4149813.37
309.00	87.48	366962.426	4149813.61
314.10	87.78	366964.883	4149798.51
122.75	85.25	366992.053	4149800.63
115.06	84.20	366998.888	4149803.79
132.12	87.07	367031.675	4149816.02
134.34	86.25	366974.772	4149799.03
135.11	85.25	366981.079	4149799.43
309.52	89.00	366980.731	4149801.72
127.26	86.22	366983.035	4149802.6
308.69	85.89	366963.297	4149797.13
315.92	88.21	366970.428	4149799.5
221.99	81.71	366974.032	4149797.21
219.27	82.06	366984.721	4149789.32
210.69	83.87	366984.721	4149789.32
315.37	86.28	366979.636	4149789.35
334.31	85.83	366981.807	4149779.52
328.83	81.59	366982.395	4149774.63
274.05	60.75	366988.421	4149781.07
179.36	81.39	366987.647	4149780.4

263.47	61.12	366987.919	4149780.28
151.60	71.99	366987.919	4149780.28
150.68	78.22	366987.877	4149780.9
153.27	68.15	366986.075	4149779.45
300.38	86.38	366986.579	4149780.35
123.75	87.66	366972.214	4149774.86
73.92	89.00	366953.162	4149752.08
72.03	89.00	366966.978	4149775.63
72.05	88.52	366980.078	4149784.52
76.21	89.00	366973.514	4149787.57
318.54	86.22	367572.36	4141639.48
311.85	88.66	367574.983	4141635.03
144.06	89.00	367572.151	4141636.59
146.48	89.00	367572.227	4141634.4
325.52	88.58	367578.706	4141617.18
319.68	89.00	367577.256	4141615.55
156.29	84.01	367576.94	4141616.71
324.04	88.69	367575.102	4141617.31
314.30	73.53	368341.574	4144069.9
208.07	89.00	368347.834	4144081.09
199.04	87.53	368352.782	4144078.8
210.05	81.12	368350.317	4144077.2
210.90	81.51	368348.901	4144078.23
209.46	84.68	368348.901	4144078.23
230.78	82.02	362472.02	4143683.71
287.08	86.67	362473.716	4143683.05
229.86	88.12	362405.43	4143653.88
181.05	76.26	362409.037	4143649.94
137.43	80.85	362401.178	4143649.33
161.42	68.48	362389.881	4143632.79
66.79	72.83	362153.58	4143845.94
146.62	78.12	362153.58	4143845.94
117.31	82.05	362156.256	4143848.99
165.67	79.70	362165.068	4143856.52
96.47	81.84	362166.654	4143852.42
336.17	76.55	362166.989	4143853.85
213.03	76.36	362168.257	4143852.91
167.92	89.00	362193.544	4143833.46
190.39	67.83	362191.641	4143835.47
234.11	78.76	362232.781	4143822.81
255.66	76.19	362224.943	4143822.11
159.36	85.16	362229.949	4143822.02
299.80	81.30	372218.467	4147912.38
342.57	89.00	372217.124	4147908.44
140.65	78.66	372343.166	4147873.23
59.52	86.06	372378.29	4147861.78

66.46	88.86	372376.721	4147864.88
341.92	83.00	372379.079	4147844.12
332.56	82.34	372403.363	4147831.7
220.13	87.05	372384.513	4147828.12
311.58	86.80	372393.191	4147816.21
12.08	77.65	372384.201	4147812.6
320.64	86.90	372376.73	4147800.14
88.51	86.10	372383.648	4147799.71
293.06	85.08	372382	4147799.12
11.88	88.14	372379.454	4147800.83
178.13	84.94	372377.03	4147795.06
96.95	86.60	371570.452	4144421.37
354.85	87.91	372389.94	4147766.16
354.52	89.00	374564.614	4142095.14
197.37	84.56	372385.84	4147797.16
197.09	85.86	372378.623	4147788.26
115.17	84.67	372376.915	4147810.28
115.12	84.80	372371.329	4147796.59
122.64	87.08	367541.374	4161115.23
168.52	87.25	367115.168	4149510.64
343.90	89.00	367113.031	4149502.58
349.77	87.55	367113.802	4149501.63
350.54	88.09	367113.866	4149500.54
251.84	89.00	367113.168	4149496.77
76.68	85.60	367116.269	4149485.33
76.30	88.58	367118.074	4149484.65
177.04	88.73	367117.341	4149475.37
93.54	2.49	367117.021	4149476.68
160.52	88.86	367118.324	4149475.24
170.89	87.25	367117.516	4149470.54
241.08	75.80	366771.826	4163324.81
2.52	75.25	366773.227	4163324.07
11.19	75.28	366772.352	4163321.63
170.66	77.37	366773.795	4163317.51
80.45	79.88	366775.731	4163315.89
212.58	85.70	366777.939	4163314.24
79.24	81.25	366775.959	4163315.84
254.93	88.51	366777.093	4163322.83
254.22	89.00	366771.097	4163320.02
79.11	88.71	366766.676	4163316.6
47.71	85.02	366772.095	4163327.29
275.17	80.48	366774.225	4163327.64
276.25	79.63	366774.987	4163328.56
75.59	75.51	366774.987	4163328.56
75.06	80.59	366774.312	4163328.96
302.61	87.34	366774.001	4163328.01

306.57	83.72	372026.864	4155976.58
185.65	80.84	372028.734	4155976.81
192.55	87.15	372028.625	4155977.41
196.98	86.21	372023.068	4155993.61
195.02	89.00	372027.449	4155990.05
15.87	88.67	372017.851	4155981.97
202.82	85.89	372016.703	4155982.93
2.27	88.85	372009.765	4155976.31
36.74	77.50	372009.801	4155978.16
27.24	85.03	372009.914	4155979.73
28.38	84.79	372017.079	4155991.46
87.99	85.21	372659.035	4155612.25
274.26	79.54	372635.979	4155636.65
105.12	73.73	372552.096	4156052.03
103.89	83.36	372560.728	4156058.95
104.22	81.62	372557.823	4156059.34
152.81	86.20	372557.82	4156062.1
150.70	89.00	372559.748	4156072.83
151.85	83.97	372569.401	4156081.61
307.62	88.30	372576.035	4156095.49
206.26	77.43	372560.047	4156094.25
233.47	85.09	372557.873	4156096.43
239.83	84.83	372576.099	4156093.84
269.33	70.78	372557.775	4156101.62
282.89	74.25	372555.235	4156114.66
208.50	83.97	372553.593	4156110.97
207.03	84.35	372562.43	4156110.97
106.48	87.35	373960.412	4155094.01
57.86	85.84	373960.412	4155094.01
45.34	86.10	373960.463	4155093.48
49.76	88.55	373957.431	4155092.85
51.46	85.09	373966.433	4155097.29
48.42	79.90	373965.655	4155096.34
42.93	85.92	373954.146	4155100.4
301.62	82.02	373961.414	4155100
123.24	82.55	373962.959	4155099.29
145.24	72.68	373958.351	4155099.73
159.68	84.81	373912.186	4155152.44
143.37	75.33	373916.834	4155149.74
138.11	77.17	373909.112	4155162.71
133.43	77.58	373906.868	4155159.82
133.21	76.54	373913.068	4155162.2
62.79	88.75	373913.042	4155162.48
244.52	86.59	373919.591	4155185.47
234.30	85.88	373915.997	4155208.8
234.11	85.88	373915.859	4155212.9

240.35	82.95	366087.998	4144484.26
182.00	83.72	366087.854	4144483.11
176.91	83.90	365628.373	4150335.74
105.04	76.52	365628.249	4150334.06
173.42	81.66	365655.138	4152014.8
166.84	80.63	365649.357	4151997.79
182.85	82.71	365651.251	4151999.93
112.52	80.97	365654.241	4152001.95
98.99	86.88	368269.905	4150480.03
256.52	82.35	368256.914	4150474.54
180.42	82.30	368268.763	4150532.38
186.06	83.88	368269.32	4150531.54
71.43	87.02	368263.377	4150539.08
78.19	81.56	368264.37	4150584.95
166.02	88.65	368260.473	4150622.06
68.10	87.38	368266.956	4150625.68
251.81	88.45	368266.672	4150625.94
74.70	87.46	368287.255	4150623.16
69.89	88.90	368291.408	4150619.1
71.40	84.27	368325.848	4150628.69
291.39	87.75	368348.367	4150622.25
27.12	84.91	368351.002	4150618.25
95.08	77.69	368368.662	4150609.64
142.04	67.26	368367.239	4150609.66
203.90	40.02	368366.451	4150607.65
283.22	72.47	368370.402	4150458.22
91.51	68.25	368372.022	4150457.11
336.14	52.97	368330.971	4150421.28
91.68	64.13	368321.804	4150372.72
120.64	62.33	368323.091	4150370.65
178.08	47.76	368357.318	4150284.79
275.96	76.73	368364.248	4150266.05
48.76	88.88	368370.405	4150243.36
287.35	88.90	368369.769	4150244.41
325.30	53.75	369198.386	4145671.26
293.64	81.34	369194.442	4145652.88
28.39	63.95	369198.308	4145653.51
7.95	65.50	369197.173	4145648.76
69.45	51.04	369192.109	4145647.9
273.57	89.00	369191.269	4145649.66
94.67	88.61	369193.399	4145647.38
287.75	75.85	369191.607	4145640.49
69.12	74.70	369188.146	4145640.67
76.93	72.35	369798.646	4146915.4
99.79	82.50	369798.403	4146916.9
156.17	68.20	369800.507	4146918.2

243.90	76.30	369831.794	4147003.77
287.14	77.34	369830.942	4147002.85
301.51	82.62	370233.546	4147504.08
114.81	62.06	370234.21	4147504.35
25.28	78.02	370229.679	4147504.81
338.21	76.39	370235.368	4147510.63
335.99	80.82	370235.504	4147508.45
337.56	83.38	370229.544	4147508.48
196.11	73.41	370234.738	4147509.69
274.54	82.83	370234.705	4147532.78
265.45	84.06	370224.971	4147564.29
274.41	86.70	370223.221	4147564.77
6.89	86.13	370227.749	4147573.64
49.85	89.00	370226.661	4147574.26
145.18	86.61	370228.533	4147577.78
233.20	87.15	370222.774	4147575.07
25.52	88.44	370223.975	4147577.95
256.36	87.27	370225.55	4147578.09
356.12	88.05	370223.96	4147580.33
313.75	89.00	370218.634	4147581.57
120.05	88.58	370215.284	4147579.26
75.01	80.53	370212.497	4147583.13
253.93	85.96	370212.888	4147583.97
203.44	89.00	370213.84	4147589.87
122.19	89.00	370212.732	4147592.52
289.92	85.74	371781.046	4146552.77
290.48	87.34	371774.026	4146539.92
268.44	85.93	371778.476	4146533.19
293.07	79.28	371774.111	4146528.06
92.42	86.42	371783.462	4146514.16
77.91	88.98	371786.277	4146513.46
24.67	85.44	371789.679	4146512.85
136.67	67.62	371790.634	4146513.26
321.36	87.05	371791.644	4146502.77
58.70	87.63	371792.018	4146501.98
1.79	88.14	371788.583	4146498.98
289.55	88.58	371793.235	4146498.2
314.32	85.71	371793.822	4146490.53
70.15	86.11	371792.132	4146491.59
26.13	82.54	371789.817	4146488.09
106.96	85.14	371794.658	4146488.51
31.12	79.76	371796.37	4146479.32
299.08	87.24	371799.014	4146476.66
229.59	88.46	372506.608	4145299.69
168.15	35.63	372506.594	4145296.83
250.08	84.53	372488.325	4145281.19

1.11	82.06	372485.828	4145271.66
245.71	72.94	372473.121	4145269.05
76.85	77.89	372449.656	4145264.29
214.43	75.00	372450.029	4145265.38
184.10	68.56	372450.405	4145251.19
75.99	86.57	372450.116	4145177.55
94.48	70.28	372452.727	4145181.89
205.91	72.51	372448.462	4145188.67
127.60	84.10	372459.788	4145197.43
64.95	89.00	372446.634	4145193.29
167.01	71.12	372447.909	4145195.63
187.80	83.93	372449.446	4145194.33
42.17	79.98	372448.874	4145199.14
175.71	84.28	373588.301	4144000.47
168.24	83.57	373590.719	4144004.82
271.06	73.13	373591.676	4144005.3
137.32	62.71	373590.75	4144006.41
34.44	80.77	373585.299	4144007.45
173.14	89.00	373586.109	4144014.87
14.90	68.25	373585.964	4144016.03
199.57	76.70	373591.944	4144011.77
78.95	80.91	373589.125	4144011.73
179.33	82.00	373588.44	4144013.51
153.75	68.66	373585.623	4144013.12
16.53	82.71	373584.318	4144015.14
46.13	85.51	373586.498	4144014.59
158.73	57.31	373169.605	4143770.07
310.02	82.85	373166.241	4143774.73
261.79	86.92	373168.763	4143774.2
265.52	84.21	373160.698	4143769.72
306.71	84.89	373163.798	4143773.08
350.39	86.00	373168.087	4143776.14
8.61	84.15	373181.746	4143789.47
256.35	86.25	373181.569	4143788.54
80.06	89.00	373180.605	4143786.13
348.28	87.24	373180.415	4143790.23
77.73	85.00	373186.458	4143803.25
96.56	34.95	373199.923	4143803.88
255.71	44.00	373830.15	4142973.29
297.84	63.71	373828.392	4142970.82
260.31	84.17	373823.365	4142968.06
119.20	47.31	373814.716	4142948.04
295.56	78.70	373984.783	4143502.61
44.72	54.63	373985.268	4143502.29
269.43	87.41	373983.098	4143491.76
162.61	76.51	373982.865	4143492.01

280.11	85.51	373981.233	4143477.81
162.81	86.56	373980.544	4143469.49
257.60	81.27	373971.203	4143464.51
351.14	88.25	374242.864	4143312.38
145.74	79.83	374244.044	4143313.37
139.28	72.91	374242.858	4143300.65
257.48	85.02	374238.632	4143299.84
264.29	87.66	374213.543	4143135
307.56	76.06	374197.306	4143112.53
173.33	85.37	374204.245	4143108.79
75.53	83.04	374197.109	4143027.17
316.03	66.08	371789.934	4146487.5
283.60	88.73	371788.666	4146484.16
276.45	82.61	371788.995	4146483.35
307.06	73.04	371797.248	4146484.3
133.29	66.16	371796.764	4146482.74
265.08	76.13	372502.227	4145297.9
284.49	66.89	372500.764	4145302.6
113.38	79.26	372492.752	4145293.24
292.10	66.42	372485.926	4145283.37
292.06	75.60	372477.807	4145270.94
326.13	79.52	372474.966	4145265.55
269.09	66.90	372475.581	4145266.5
78.44	76.50	372450.944	4145261.67
79.07	78.33	372446.572	4145243.05
145.35	85.84	372448.256	4145184.41
129.27	80.04	372460.83	4145191.39
139.33	78.39	372459.316	4145198.61
276.76	86.63	372451.562	4145193

Table 4. Synthetic Joint Data (UTM Zone 11 N)

Strike	Dip	X (Easting)	Y (Northing)
137.00	90.00	367426.79	4141296.45
330.00	90.00	365184.55	4141669.58
309.00	90.00	368921.61	4141669.58
323.00	90.00	366679.37	4142042.70
301.00	90.00	370416.44	4142042.70
156.00	90.00	364437.13	4142415.82
316.00	90.00	368174.20	4142415.82
290.00	90.00	371911.27	4142415.82
330.00	90.00	365931.96	4142788.94
307.00	90.00	369669.03	4142788.94
276.00	90.00	373406.09	4142788.94
342.00	90.00	363689.72	4143162.07
143.00	90.00	367426.79	4143162.07
297.00	90.00	371163.85	4143162.07
82.00	90.00	374900.92	4143162.07
156.00	90.00	365184.55	4143535.19
315.00	90.00	368921.61	4143535.19
102.00	90.00	372658.68	4143535.19
69.00	90.00	376395.75	4143535.19
348.00	90.00	362942.31	4143908.31
330.00	90.00	366679.37	4143908.31
304.00	90.00	370416.44	4143908.31
86.00	90.00	374153.51	4143908.31
238.00	90.00	377890.57	4143908.31
343.00	90.00	364437.13	4144281.43
322.00	90.00	368174.20	4144281.43
109.00	90.00	371911.27	4144281.43
251.00	90.00	375648.33	4144281.43
337.00	90.00	365931.96	4144654.56
313.00	90.00	369669.03	4144654.56
270.00	90.00	373406.09	4144654.56
59.00	90.00	377143.16	4144654.56
348.00	90.00	363689.72	4145027.68
330.00	90.00	367426.79	4145027.68
298.00	90.00	371163.85	4145027.68
253.00	90.00	374900.92	4145027.68
49.00	90.00	378637.99	4145027.68
343.00	90.00	365184.55	4145400.80
142.00	90.00	368921.61	4145400.80
276.00	90.00	372658.68	4145400.80
60.00	90.00	376395.75	4145400.80
337.00	90.00	366679.37	4145773.92
310.00	90.00	370416.44	4145773.92

75.00	90.00	374153.51	4145773.92
230.00	90.00	377890.57	4145773.92
348.00	90.00	364437.13	4146147.05
150.00	90.00	368174.20	4146147.05
106.00	90.00	371911.27	4146147.05
61.00	90.00	375648.33	4146147.05
343.00	90.00	365931.96	4146520.17
321.00	90.00	369669.03	4146520.17
77.00	90.00	373406.09	4146520.17
231.00	90.00	377143.16	4146520.17
353.00	90.00	363689.72	4146893.29
338.00	90.00	367426.79	4146893.29
302.00	90.00	371163.85	4146893.29
61.00	90.00	374900.92	4146893.29
42.00	90.00	378637.99	4146893.29
349.00	90.00	365184.55	4147266.42
331.00	90.00	368921.61	4147266.42
259.00	90.00	372658.68	4147266.42
231.00	90.00	376395.75	4147266.42
358.00	90.00	362942.31	4147639.54
344.00	90.00	366679.37	4147639.54
323.00	90.00	370416.44	4147639.54
60.00	90.00	374153.51	4147639.54
42.00	90.00	377890.57	4147639.54
354.00	90.00	364437.13	4148012.66
339.00	90.00	368174.20	4148012.66
88.00	90.00	371911.27	4148012.66
231.00	90.00	375648.33	4148012.66
349.00	90.00	365931.96	4148385.78
335.00	90.00	369669.03	4148385.78
238.00	90.00	373406.09	4148385.78
223.00	90.00	377143.16	4148385.78
359.00	90.00	363689.72	4148758.91
345.00	90.00	367426.79	4148758.91
335.00	90.00	371163.85	4148758.91
50.00	90.00	374900.92	4148758.91
35.00	90.00	378637.99	4148758.91
355.00	90.00	365184.55	4149132.03
342.00	90.00	368921.61	4149132.03
50.00	90.00	372658.68	4149132.03
43.00	90.00	376395.75	4149132.03
5.00	90.00	362942.31	4149505.15
171.00	90.00	366679.37	4149505.15
343.00	90.00	370416.44	4149505.15
47.00	90.00	374153.51	4149505.15
35.00	90.00	377890.57	4149505.15

1.00	90.00	364437.13	4149878.27
167.00	90.00	368174.20	4149878.27
24.00	90.00	371911.27	4149878.27
42.00	90.00	375648.33	4149878.27
192.00	90.00	362194.89	4150251.40
357.00	90.00	365931.96	4150251.40
346.00	90.00	369669.03	4150251.40
221.00	90.00	373406.09	4150251.40
215.00	90.00	377143.16	4150251.40
8.00	90.00	363689.72	4150624.52
352.00	90.00	367426.79	4150624.52
359.00	90.00	371163.85	4150624.52
219.00	90.00	374900.92	4150624.52
208.00	90.00	378637.99	4150624.52
4.00	90.00	365184.55	4150997.64
349.00	90.00	368921.61	4150997.64
29.00	90.00	372658.68	4150997.64
35.00	90.00	376395.75	4150997.64
15.00	90.00	362942.31	4151370.76
358.00	90.00	366679.37	4151370.76
352.00	90.00	370416.44	4151370.76
35.00	90.00	374153.51	4151370.76
29.00	90.00	377890.57	4151370.76
191.00	90.00	364437.13	4151743.89
353.00	90.00	368174.20	4151743.89
12.00	90.00	371911.27	4151743.89
33.00	90.00	375648.33	4151743.89
23.00	90.00	362194.89	4152117.01
185.00	90.00	365931.96	4152117.01
171.00	90.00	369669.03	4152117.01
27.00	90.00	373406.09	4152117.01
28.00	90.00	377143.16	4152117.01
19.00	90.00	363689.72	4152490.13
358.00	90.00	367426.79	4152490.13
360.00	90.00	371163.85	4152490.13
209.00	90.00	374900.92	4152490.13
32.00	90.00	361447.48	4152863.25
193.00	90.00	365184.55	4152863.25
352.00	90.00	368921.61	4152863.25
17.00	90.00	372658.68	4152863.25
207.00	90.00	376395.75	4152863.25
28.00	90.00	362942.31	4153236.38
4.00	90.00	366679.37	4153236.38
355.00	90.00	370416.44	4153236.38
24.00	90.00	374153.51	4153236.38
23.00	90.00	377890.57	4153236.38

23.00	90.00	364437.13	4153609.50
355.00	90.00	368174.20	4153609.50
7.00	90.00	371911.27	4153609.50
25.00	90.00	375648.33	4153609.50
37.00	90.00	362194.89	4153982.62
13.00	90.00	365931.96	4153982.62
172.00	90.00	369669.03	4153982.62
17.00	90.00	373406.09	4153982.62
23.00	90.00	377143.16	4153982.62
33.00	90.00	363689.72	4154355.75
359.00	90.00	367426.79	4154355.75
359.00	90.00	371163.85	4154355.75
21.00	90.00	374900.92	4154355.75
47.00	90.00	361447.48	4154728.87
24.00	90.00	365184.55	4154728.87
352.00	90.00	368921.61	4154728.87
190.00	90.00	372658.68	4154728.87
22.00	90.00	376395.75	4154728.87
44.00	90.00	362942.31	4155101.99
5.00	90.00	366679.37	4155101.99
174.00	90.00	370416.44	4155101.99
17.00	90.00	374153.51	4155101.99
37.00	90.00	364437.13	4155475.11
172.00	90.00	368174.20	4155475.11
3.00	90.00	371911.27	4155475.11
19.00	90.00	375648.33	4155475.11
16.00	90.00	365931.96	4155848.24
171.00	90.00	369669.03	4155848.24
192.00	90.00	373406.09	4155848.24
199.00	90.00	377143.16	4155848.24
231.00	90.00	363689.72	4156221.36
352.00	90.00	367426.79	4156221.36
358.00	90.00	371163.85	4156221.36
17.00	90.00	374900.92	4156221.36
36.00	90.00	365184.55	4156594.48
349.00	90.00	368921.61	4156594.48
6.00	90.00	372658.68	4156594.48
18.00	90.00	376395.75	4156594.48
352.00	90.00	366679.37	4156967.60
173.00	90.00	370416.44	4156967.60
13.00	90.00	374153.51	4156967.60
167.00	90.00	368174.20	4157340.73
1.00	90.00	371911.27	4157340.73
17.00	90.00	375648.33	4157340.73
345.00	90.00	365931.96	4157713.85
350.00	90.00	369669.03	4157713.85

9.00	90.00	373406.09	4157713.85
17.00	90.00	377143.16	4157713.85
343.00	90.00	367426.79	4158086.97
357.00	90.00	371163.85	4158086.97
14.00	90.00	374900.92	4158086.97
347.00	90.00	368921.61	4158460.09
5.00	90.00	372658.68	4158460.09
17.00	90.00	376395.75	4158460.09
336.00	90.00	366679.37	4158833.22
353.00	90.00	370416.44	4158833.22
12.00	90.00	374153.51	4158833.22
344.00	90.00	368174.20	4159206.34
1.00	90.00	371911.27	4159206.34
16.00	90.00	375648.33	4159206.34
324.00	90.00	365931.96	4159579.46
350.00	90.00	369669.03	4159579.46
188.00	90.00	373406.09	4159579.46
18.00	90.00	377143.16	4159579.46
339.00	90.00	367426.79	4159952.58
358.00	90.00	371163.85	4159952.58
14.00	90.00	374900.92	4159952.58
310.00	90.00	365184.55	4160325.71
347.00	90.00	368921.61	4160325.71
185.00	90.00	372658.68	4160325.71
18.00	90.00	376395.75	4160325.71
152.00	90.00	366679.37	4160698.83
355.00	90.00	370416.44	4160698.83
12.00	90.00	374153.51	4160698.83
163.00	90.00	368174.20	4161071.95
2.00	90.00	371911.27	4161071.95
17.00	90.00	375648.33	4161071.95
324.00	90.00	365931.96	4161445.08
172.00	90.00	369669.03	4161445.08
9.00	90.00	373406.09	4161445.08
339.00	90.00	367426.79	4161818.20
359.00	90.00	371163.85	4161818.20
16.00	90.00	374900.92	4161818.20
317.00	90.00	365184.55	4162191.32
348.00	90.00	368921.61	4162191.32
7.00	90.00	372658.68	4162191.32
22.00	90.00	376395.75	4162191.32
333.00	90.00	366679.37	4162564.44
356.00	90.00	370416.44	4162564.44
195.00	90.00	374153.51	4162564.44
164.00	90.00	368174.20	4162937.57
4.00	90.00	371911.27	4162937.57

22.00	90.00	375648.33	4162937.57
327.00	90.00	365931.96	4163310.69
353.00	90.00	369669.03	4163310.69
193.00	90.00	373406.09	4163310.69
340.00	90.00	367426.79	4163683.81
2.00	90.00	371163.85	4163683.81
22.00	90.00	374900.92	4163683.81
143.00	90.00	365184.55	4164056.93
350.00	90.00	368921.61	4164056.93
191.00	90.00	372658.68	4164056.93
28.00	90.00	376395.75	4164056.93
336.00	90.00	366679.37	4164430.06
359.00	90.00	370416.44	4164430.06
20.00	90.00	374153.51	4164430.06
346.00	90.00	368174.20	4164803.18
9.00	90.00	371911.27	4164803.18
28.00	90.00	375648.33	4164803.18
152.00	90.00	365931.96	4165176.30
356.00	90.00	369669.03	4165176.30
18.00	90.00	373406.09	4165176.30
343.00	90.00	367426.79	4165549.42
186.00	90.00	371163.85	4165549.42
27.00	90.00	374900.92	4165549.42
353.00	90.00	368921.61	4165922.55
16.00	90.00	372658.68	4165922.55
340.00	90.00	366679.37	4166295.67
3.00	90.00	370416.44	4166295.67
25.00	90.00	374153.51	4166295.67
351.00	90.00	368174.20	4166668.79
194.00	90.00	371911.27	4166668.79
181.00	90.00	369669.03	4167041.92
23.00	90.00	373406.09	4167041.92
168.00	90.00	367426.79	4167415.04
11.00	90.00	371163.85	4167415.04
210.00	90.00	374900.92	4167415.04
358.00	90.00	368921.61	4167788.16
20.00	90.00	372658.68	4167788.16
346.00	90.00	366679.37	4168161.28
8.00	90.00	370416.44	4168161.28
208.00	90.00	374153.51	4168161.28
356.00	90.00	368174.20	4168534.41
18.00	90.00	371911.27	4168534.41
186.00	90.00	369669.03	4168907.53
205.00	90.00	373406.09	4168907.53
354.00	90.00	367426.79	4169280.65
15.00	90.00	371163.85	4169280.65

3.00	90.00	368921.61	4169653.77
311.00	90.00	384850.16	4173385.00
120.00	90.00	383441.71	4173385.00
281.00	90.00	382033.27	4173385.00
249.00	90.00	380624.83	4173385.00
41.00	90.00	379216.39	4173385.00
34.00	90.00	377807.94	4173385.00
35.00	90.00	376399.50	4173385.00
33.00	90.00	374991.06	4173385.00
30.00	90.00	373582.62	4173385.00
205.00	90.00	372174.18	4173385.00
19.00	90.00	370765.73	4173385.00
13.00	90.00	369357.29	4173385.00
6.00	90.00	367948.85	4173385.00
359.00	90.00	366540.41	4173385.00
173.00	90.00	365131.96	4173385.00
346.00	90.00	363723.52	4173385.00
340.00	90.00	362315.08	4173385.00
155.00	90.00	360906.64	4173385.00
330.00	90.00	359498.20	4173385.00
325.00	90.00	358089.75	4173385.00
320.00	90.00	356963.00	4172788.75
314.00	90.00	356963.00	4170801.27
307.00	90.00	356963.00	4168813.78
119.00	90.00	356963.00	4166826.29
291.00	90.00	356963.00	4164838.80
282.00	90.00	356963.00	4162851.32
273.00	90.00	356963.00	4160863.83
83.00	90.00	356963.00	4158876.34
72.00	90.00	356963.00	4156888.85
61.00	90.00	356963.00	4154901.37
49.00	90.00	356963.00	4152913.88
37.00	90.00	356963.00	4150926.39
27.00	90.00	356963.00	4148938.90
199.00	90.00	356963.00	4146951.42
13.00	90.00	356963.00	4144963.93
9.00	90.00	356963.00	4142976.44
3.00	90.00	356963.00	4140988.95
355.00	90.00	356963.00	4139001.47
346.00	90.00	356963.00	4137013.98
338.00	90.00	356963.00	4135026.49
331.00	90.00	357667.22	4133834.00
327.00	90.00	359075.66	4133834.00
142.00	90.00	360484.11	4133834.00
317.00	90.00	361892.55	4133834.00
312.00	90.00	363300.99	4133834.00

307.00	90.00	364709.43	4133834.00
303.00	90.00	366117.87	4133834.00
118.00	90.00	367526.32	4133834.00
293.00	90.00	368934.76	4133834.00
287.00	90.00	370343.20	4133834.00
102.00	90.00	371751.64	4133834.00
276.00	90.00	373160.09	4133834.00
270.00	90.00	374568.53	4133834.00
84.00	90.00	375976.97	4133834.00
78.00	90.00	377385.41	4133834.00
72.00	90.00	378793.85	4133834.00
65.00	90.00	380202.30	4133834.00
59.00	90.00	381610.74	4133834.00
52.00	90.00	383019.18	4133834.00
225.00	90.00	384427.62	4133834.00
219.00	90.00	384991.00	4135225.24
35.00	90.00	384991.00	4137212.73
210.00	90.00	384991.00	4139200.22
25.00	90.00	384991.00	4141187.70
19.00	90.00	384991.00	4143175.19
13.00	90.00	384991.00	4145162.68
7.00	90.00	384991.00	4147150.17
2.00	90.00	384991.00	4149137.65
359.00	90.00	384991.00	4151125.14
360.00	90.00	384991.00	4153112.63
3.00	90.00	384991.00	4155100.12
189.00	90.00	384991.00	4157087.60
11.00	90.00	384991.00	4159075.09
8.00	90.00	384991.00	4161062.58
4.00	90.00	384991.00	4163050.07
357.00	90.00	384991.00	4165037.55
346.00	90.00	384991.00	4167025.04
334.00	90.00	384991.00	4169012.53
322.00	90.00	384991.00	4171000.02
314.00	90.00	384991.00	4172987.50
324.00	90.00	359952.65	4133834.00
311.00	90.00	363689.72	4133834.00
298.00	90.00	367426.79	4133834.00
284.00	90.00	371163.85	4133834.00
89.00	90.00	374900.92	4133834.00
252.00	90.00	378637.99	4133834.00
235.00	90.00	382375.05	4133834.00
332.00	90.00	357710.41	4134207.12
140.00	90.00	361447.48	4134207.12
127.00	90.00	365184.55	4134207.12
113.00	90.00	368921.61	4134207.12

98.00	90.00	372658.68	4134207.12
82.00	90.00	376395.75	4134207.12
65.00	90.00	380132.81	4134207.12
227.00	90.00	383869.88	4134207.12
329.00	90.00	359205.24	4134580.25
315.00	90.00	362942.31	4134580.25
302.00	90.00	366679.37	4134580.25
108.00	90.00	370416.44	4134580.25
272.00	90.00	374153.51	4134580.25
75.00	90.00	377890.57	4134580.25
58.00	90.00	381627.64	4134580.25
338.00	90.00	356963.00	4134953.37
325.00	90.00	360700.07	4134953.37
311.00	90.00	364437.13	4134953.37
297.00	90.00	368174.20	4134953.37
282.00	90.00	371911.27	4134953.37
86.00	90.00	375648.33	4134953.37
68.00	90.00	379385.40	4134953.37
49.00	90.00	383122.47	4134953.37
334.00	90.00	358457.83	4135326.49
140.00	90.00	362194.89	4135326.49
307.00	90.00	365931.96	4135326.49
292.00	90.00	369669.03	4135326.49
276.00	90.00	373406.09	4135326.49
78.00	90.00	377143.16	4135326.49
61.00	90.00	380880.23	4135326.49
41.00	90.00	384617.29	4135326.49
330.00	90.00	359952.65	4135699.61
316.00	90.00	363689.72	4135699.61
302.00	90.00	367426.79	4135699.61
286.00	90.00	371163.85	4135699.61
89.00	90.00	374900.92	4135699.61